

Hybrid Josephson junctions and their qubit applications

PROEFSCHRIFT

TER VERKRIJGING VAN
DE GRAAD VAN DOCTOR AAN DE UNIVERSITEIT LEIDEN,
OP GEZAG VAN RECTOR MAGNIFICUS PROF.DR.IR. H. BIJL,
VOLGENS BESLUIT VAN HET COLLEGE VOOR PROMOTIES
TE VERDEDIGEN OP DINSDAG 3 SEPTEMBER 2024
KLOKKE 11.30 UUR

DOOR

Tereza Vakhtel

GEBOREN TE KYIV, OEKRAÏNE IN 1997

Promotor: Prof. dr. C. W. J. Beenakker
Co-promotor: Dr. B. van Heck (Sapienza University of Rome, Italy)

Promotiecommissie: Dr. A. R. Akhmerov (TU Delft)
Prof. dr. S. J. van der Molen
Prof. dr. K. E. Schalm
Prof. dr. J. S. Meyer (University of Grenoble, France)
Dr. G. Welker (TU Delft)

Casimir PhD Series Delft-Leiden 2024-24

ISBN 978-90-8593-405-9

An electronic version of this thesis can be found
at <https://openaccess.leidenuniv.nl>

Front cover: An artist's impression (Dr. Anastasiia Skurativska) of an S-N-S Josephson junction, inspired by the Dutch artist M.C. Escher (1898-1972). The pairs of the birds symbolize Cooper pairs in the superconducting leads. The blue birds symbolize incident electrons on the superconductor-semiconductor interface, which are reflected as holes (empty spaces between the blue birds that resemble white birds).

To my family and friends.

Contents

1	Introduction	1
1.1	Preface	1
1.2	Josephson effects	2
1.2.1	Tunneling Josephson junction	2
1.2.2	Andreev reflection	3
1.2.3	S-N-S junction	4
1.2.4	S-R-S junction	5
1.3	Superconducting qubits	6
1.3.1	Transmon qubit	7
1.3.2	Fluxonium qubit	9
1.4	Minimally twisted bilayer graphene	11
1.5	Bloch oscillations	15
1.6	Altermagnets	16
1.7	This thesis	19
1.7.1	Chapter 2	19
1.7.2	Chapter 3	19
1.7.3	Chapter 4	20
1.7.4	Chapter 5	21
1.7.5	Chapter 6	21
2	Quantum phase slips in a resonant Josephson junction	23
2.1	Introduction	23
2.2	2π and 4π quantum phase slips	24
2.3	Model	27
2.4	WKB analysis	30
2.5	Results	34
2.6	Conclusions	37

2.6.1	Experimental observability of 4π phase slips in transmon circuits	38
2.6.2	Connection to novel qubit designs	39
2.6.3	Connection to Majorana zero modes	39
2.6.4	Generality of our results	40
2.7	Appendix: Derivation of the low-energy Hamiltonian	41
2.8	Appendix: WKB solution	44
2.9	Appendix: Evaluation of the WKB integrals	57
3	Tunneling of fluxons via a Josephson resonant level	65
3.1	Introduction	65
3.2	Model	67
3.3	Wentzel–Kramers–Brillouin (WKB) analysis	69
3.4	Duality with a topological superconducting island	74
3.5	Conclusion	78
3.6	Appendix: Definitions of the coefficients	80
3.7	Appendix: Expressions for the low-energy Hamiltonian parameters	81
4	Phase-shifted Andreev levels in an altermagnet Josephson junction	85
4.1	Introduction	85
4.2	Altermagnet Josephson junction	87
4.3	Andreev levels without normal reflection	88
4.4	Including normal reflection	89
4.5	Comparison with computer simulations	92
4.6	Josephson energy and supercurrent	93
4.7	Conclusion	95
4.8	Appendix: Scattering matrix calculation of the Andreev levels	95
4.9	Appendix: Tight-binding calculations	97
5	Bloch oscillations in the magnetoconductance of twisted bilayer graphene	103
5.1	Introduction	103
5.2	Network model	104
5.3	Quantum walk	106
5.4	Bloch oscillations	108
5.5	Magnetic breakdown	108
5.6	Conductance	110

5.7	Conclusion	112
6	Breathing mode in open-orbit magnetotransport: a magnetic lens with a quantum mechanical focal length	115
6.1	Introduction	115
6.2	Calculation of the breathing mode	116
6.3	Tight-binding model	119
6.4	Semiclassical approximation	121
6.5	Magnetoconductance oscillations	124
6.6	Conclusion	126
6.7	Appendix: Calculation of the interference oscillations in the root-mean-square displacement	127
6.8	Appendix: Magnetic lens for multiple coupled open orbits .	127
	Bibliography	131
	Summary	149
	Samenvatting	151
	Підсумки	153
	Curriculum Vitæ	155
	List of Publications	157

Chapter 1

Introduction

1.1 Preface

At the heart of this thesis is the Josephson effect – a condensed matter physics phenomenon of both fundamental and practical importance, one of the most exciting aspects of superconductivity. This effect occurs when a nanostructure, a weak link or an insulating barrier is placed between two superconductors. Such a device (Josephson junction) can sustain a dissipationless supercurrent that can flow without voltage bias. The effect is named after Brian Josephson, who provided its first mathematical description for the case of the tunneling barrier [1, 2]. The theoretical understanding and nanofabrication technique developments enabled numerous applications of such tunneling Josephson junctions; among the most famous ones are SQUID (superconducting quantum interference device) magnetometers, NIST standard of volt and superconducting qubits [3, 4]. The thesis focuses on the latter application, where further understanding of the Josephson effect in more complex devices may lead to improved properties of the qubits.

From the microscopic point of view, the ground states of the superconducting leads are condensates of Cooper pairs in a collective symmetry broken state, described by a complex order parameter. This complex order parameter has a phase, and, in a tunneling Josephson junction, the supercurrent will depend on the phase difference between the two superconductors ϕ in a non-linear way: $I \sim \sin \phi$. Due to the second Josephson relation $\dot{\phi} \sim V$, where V is the voltage drop across the junction, this non-linearity makes the junction a non-dissipative non-linear inductor. In

parallel with a capacitor and in the regime where ϕ is a quantum variable, such a system becomes a non-linear quantum oscillator, which happens to be one of the best pieces of hardware for a qubit. More sophisticated Josephson junctions may have more internal degrees of freedom and different current-phase characteristics [5]. These can be employed to design qubits even more robust to dephasing and decay.

The subject of Chapter 2 and Chapter 3 is a superconductor-quantum dot- superconductor (S-R-S) junction embedded in two different quantum circuits. In Chapter 2, we explore the circuit where the S-R-S junction is shunted (connected in parallel) with a capacitance. An essential characteristic of this system is the sensitivity of the spectrum to the fluctuations of the gate voltage used for the control of the qubit. We make detailed calculations of the dependence on the gate voltage while reproducing some previous theoretical predictions that, in some fine-tuned regime, the sensitivity should become extremely small.

In the second circuit, the capacitively shunted junction is additionally shunted with a linear inductor. In Chapter 3, we calculate energy splittings between states typically used for quantum computation. Such a system is one of the realisations of the so-called bi-fluxon qubit, where the coupling between $|0\rangle$ and $|1\rangle$ states is suppressed due to an additional conservation law forbidding the transition [6, 7].

Finally, Chapter 4 explores how the Josephson effect is modified in a junction containing a recently discovered class of magnetic materials: altermagnet. A distinct feature of such Josephson junctions is that the energy minimum may be achieved at the non-zero phase difference [8, 9], unlike in the tunneling junctions.

1.2 Josephson effects

We will start with the simplest type of a Josephson junction: superconductor-insulator-superconductor (S-I-S) junction. The second and third types are S-N-S (superconductor-semiconductor-superconductor) and S-R-S (superconductor-quantum dot-superconductor).

1.2.1 Tunneling Josephson junction

Tunneling (S-I-S) Josephson junction is the most widely used one for superconducting qubits. Usually, it's made of aluminium leads in the superconducting state with aluminium oxide in between; such a device can be

fabricated with the shadow evaporation technique. Each piece of the superconductors is described by a superconducting wave function $\psi = |\psi|e^{i\varphi}$: its amplitude corresponds to the superfluid density, and the phase is referred to as the superconducting phase. Because there is a small but non-zero overlap between the two wavefunctions, a Cooper pair can tunnel, and a non-zero supercurrent will flow. The low energy Hamiltonian of such a junction is :

$$H(\phi) = -E_J \cos \phi, \quad (1.1)$$

E_J is the positive Josephson energy, and ϕ is the superconducting phase difference between the two leads. Because the charge (in the units of the Cooper pair charge) operator is canonically conjugated to phase, the charge operator is:

$$\hat{n} = -i\partial_\phi. \quad (1.2)$$

Then, the current-phase relation is given by:

$$I(\phi) = 2eE_J \sin \phi. \quad (1.3)$$

This is the well-known first Josephson relation. A version of the celebrated Ambegaokar-Baratoff formula connects E_J to the normal state conductance G_N of the junction [10–12]:

$$E_J = \frac{G_N \Delta}{G_Q} \frac{\Delta}{8}, \quad G_Q = \frac{e^2}{h}, \quad (1.4)$$

where Δ is the superconducting gap. If there is a non-zero voltage drop V across the junction, the Josephson relation says $\dot{\phi} = 2eV$. This relation can be derived from gauge invariance reasonings and relates the superconducting phase to the flux. It allows to compute the inductance of the junction $L_J^{-1} = \frac{\partial^2 E(\phi)}{\partial \phi^2}$. The non-linear inductance is one of the properties that make Josephson junctions an important element of superconducting qubits, as will be discussed further.

1.2.2 Andreev reflection

In the tunneling junction, the Josephson energy and the supercurrent can be derived using second-order perturbation theory [13]. In an S-N-S junction, the coupling between the leads generally cannot be treated as

a perturbation. Therefore, a more microscopic approach to the origin of the supercurrent is needed. Let us consider a perfect NS (normal metal-superconductor) interface first. Suppose, from the normal side, there is an incident electron with energy $E < \Delta$ (measured from the Fermi energy), meaning it cannot enter the superconductor. Naively, no charge transfer can happen in this situation. Nevertheless, superconductivity allows charge transfer via Andreev reflection when the electron gets reflected as a hole [14]. Because the total charge has to be conserved, an additional Cooper pair was created in the superconductor, so the transferred charge is $2e$. Since the excitation energy inside the normal part has to stay the same: $E = v_F(k_e - k_F) = -v_F(k_h - k_F)$ and $k_e - k_h = 2E/v_F$. Usually, the coherence length $\xi \equiv v_F/\Delta \gg 1/k_F$, so the momenta are almost the same (Andreev approximation). However, the hole's velocity will be the opposite of the electron's, hence the name reflection. A reverse process, when a hole is reflected as an electron, can also happen. One can match the electron/hole wavefunction to the solution of the Bogoliubov-de Gennes equation in the superconducting part and obtain that the reflected hole/electron also acquires a relative phase [13]:

$$\chi = -\arccos\left(\frac{E}{\Delta}\right) \mp \varphi, \quad (1.5)$$

where $-/+$ is for the incident electron/hole case.

1.2.3 S-N-S junction

A closed trajectory becomes possible if one has an SNS junction instead of one NS interface. First, an electron is Andreev reflected as a hole, and then the hole propagates to the other SN interface and is reflected again as an electron. Such a bound motion implies the possibility of a state localized in the junction called the Andreev bound state. Note that a Cooper pair is transferred between the leads after these two processes so that such states may carry a supercurrent. Often, one assumes a short junction limit $L \ll \xi$, in which the accumulation of phase due to ballistic propagation of an electron/hole $(k_e - k_h)L$ can be neglected. In this case, the Andreev bound states' energies obtained from the scattering formalism are [15]:

$$E_{\text{ABS}}(\phi) = \Delta \sqrt{1 - T \sin^2(\phi/2)}, \quad (1.6)$$

where T is the transmission eigenvalue of the junction. These states are spin-degenerate and are the only ones that contribute to the supercurrent in the short-junction limit, as the continuum contribution is negligible. Usually, there are multiple Andreev bound states that originate from multiple channels at the Fermi energy. The tunneling Josephson potential 1.1 can be obtained from 1.6 by the Taylor expansion around $T_n = 0$, where n stands for each channel contributing to the in-gap spectrum. The correspondence reads $E_J = \Delta \sum_n T_n / 4$. Note that formally, because the tunneling junctions are usually only 1 atom thick, the scattering matrix approach for the Andreev bound states' spectrum does not apply, as one cannot insert leads inside the normal part of the junction. Nevertheless, the formula works.

1.2.4 S-R-S junction

The previous model, however, doesn't describe all the typical experimental situations. Some of the InAs-Al-shell Josephson junctions rather look like a small confined region (quantum dot) weakly coupled to the leads (with the tunneling rates Γ_1, Γ_2) [16, 17]. We assume that this region hosts a single spin-degenerate level. If the dwell time $\tau_{dw} = \Gamma^{-1} \equiv 1/(\Gamma_1 + \Gamma_2) \gg \Delta^{-1}$, then this junction is in the opposite to the short junction $\tau_{dw} = L/v_F \ll 1/\Delta$ limit, and it will have different properties. In what follows, we will focus exactly on the tunneling $\tau_{dw} \gg \Delta^{-1}$ limit. In a more general case, the Andreev bound states' energies cannot be written in a closed form [5]. We will also assume that the total number of the electrons in the leads and on the dot is even, such that at 0 temperature, it's sufficient to consider only two possible occupation numbers of the quantum dot (0 and 2). Given these assumptions, the low-energy Hamiltonian is [18–21]:

$$H_{QD} = 4E_C(-i\partial_\phi - n_g)^2 + V(\phi) \quad (1.7)$$

$$V(\phi) = -\epsilon_r \tau_z - \Gamma \cos(\phi/2) \tau_x - \delta\Gamma \sin(\phi/2) \tau_y, \quad (1.8)$$

where the Pauli matrices act in the occupation number of the dot space, $\delta\Gamma = \Gamma_1 - \Gamma_2$ and ϵ_r is the detuning of the resonant level from the Fermi energy in the leads. There's also a capacitive energy with $E_C = e^2/2C$ (where C is the capacitance of the junction) due to the dipole moment generated by Cooper pair tunneling and equilibrium charge n_g controlled by a gate (in the Cooper pair charge units), shown on the circuit. Note that the Hamiltonian is not 2π -periodic. This is because it is written in a

2π -anti-periodic basis, with twisted boundary conditions [22]:

$$\Psi(\phi + 2\pi) = \tau_z \Psi(\phi). \quad (1.9)$$

The Fourier decomposition of these basis states in terms of the states with well-defined charge is:

$$\begin{aligned} \Psi_0(\phi) &= \sum_{n \in \mathbb{Z}} e^{i\phi n} \Psi_0(n), \\ \Psi_2(\phi) &= \sum_{n \in \mathbb{Z} + \frac{1}{2}} e^{i\phi n} \Psi_2(n). \end{aligned} \quad (1.10)$$

Here, n is the charge transferred across the junction, as this is the variable related to the dipole moment. In the second sum, the summation goes over half-integer n because when the quantum dot is occupied twice, it amounts to $1/2$ of the Cooper pair transfer. Hence, the Hamiltonian is 2π -periodic if one accounts for the aperiodicity of the basis. The eigenvalues of $V(\phi)$ are $\pm E_A(\phi)$, where E_A happens to be the same as the Andreev bound state's energy (due to spin degeneracy):

$$E_A = \Gamma_A \sqrt{1 - T \sin^2 \phi/2}, \quad \Gamma_A = \sqrt{\Gamma^2 + \epsilon_r^2}. \quad (1.11)$$

$T = 1 - |r|^2$ is the effective transparency of the junction with $r = \frac{\epsilon_r + i\delta\Gamma}{\Gamma_A}$. The spectrum is similar to that of SNS, but the Andreev bound states are detached from the continuum, and the wavefunctions are different. The effects of this difference on the qubit are discussed in Chapters 3 and 2. Usually, a quantum dot has a non-negligible (Anderson U) Coulomb energy. This can make an odd-occupied Andreev bound state the ground state of the junction [23], especially if the transparency is almost perfect. However, this energy can be neglected if $\Gamma \gg U$ [18] and the quantum dot cannot be occupied only once at zero temperature if the total number of electrons in the circuit is even.

1.3 Superconducting qubits

Superconductors offer a promising platform for quantum computation because: a) A single piece of a superconductor has a non-degenerate ground state and b) the excitations of this ground state are separated by a superconducting gap. If the qubit's energies are deep within the gap, the

coupling to the continuum degrees of freedom is suppressed. Usually, the superconducting gaps are of the order of ~ 100 GHz, and the qubits are operated at the 1 – 10 GHz energies, so the system has to be cooled down to ~ 10 mK. The most naive qubit would be a quantum version of a harmonic oscillator: an inductor in parallel with a capacitor. However, this system has an obvious problem: one cannot address a specific transition because the levels are equidistant. In the previous section 1.2.1, we learned that a Josephson junction is a non-linear inductor, which makes it a useful part of a qubit. The following two subsections briefly discuss two common types of qubits based on tunneling Josephson junctions.

1.3.1 Transmon qubit

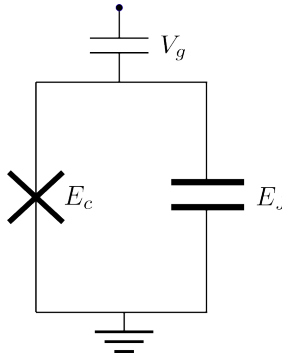


Figure 1.1. Transmon circuit

If a Josephson junction is shunted by a capacitor, similarly as in 1.2.4, the Hamiltonian of such a circuit is [24, 25]:

$$\hat{H} = 4E_C (\hat{n} - n_g)^2 - E_J \cos \hat{\phi}. \quad (1.12)$$

The number of Cooper pairs on the island is an integer, so the boundary conditions are periodic $\psi(\phi + 2\pi) = \psi(\phi)$ as $e^{in(\phi+2\pi)} = e^{in\phi}$ if $n \in \mathbb{Z}$. The eigenvalue problem is mathematically equivalent to that of an electron in the periodic crystal. ψ satisfies the same differential equation as a Bloch wave with quasi-momentum n_g . One can always make a gauge transformation $\psi \rightarrow \psi e^{-i\phi}$, which preserves the periodic boundary conditions but changes n_g by 1. Hence, the spectrum will be periodic in n_g . We consider two illustrative limits.

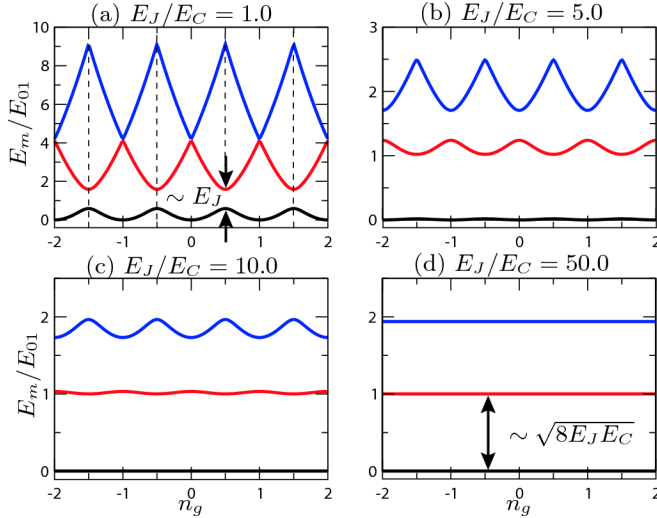


Figure 1.2. Eigenenergies of the transmon Hamiltonian 1.12 as a function of n_g for different ratios E_J/E_C . Energies are given in units of the transition energy E_{01} between the ground and first excited state, evaluated at $n_g = 1/2$. *Reprinted figure with permission from J. Koch, Terri M. Yu, J. Gambetta, A. A. Houck, D. I. Schuster, J. Majer, A. Blais, M. H. Devoret, S. M. Girvin, and R. J. Schoelkopf, Phys. Rev. A **76**, 042319, 2007. Copyright (2007) by the American Physical Society*

Cooper pair box $E_C \gg E_J$ regime

One will typically end up in this situation if the junction is not shunted by a big capacitor on purpose. The spectrum of the junction is then very similar to that of a nearly free electron, where the Cooper pair tunneling introduces the avoided crossings between the charge parabolas. Such a qubit has a high degree of anharmonicity [26], but its energy depends strongly on n_g . A gate that controls this equilibrium charge typically fluctuates, leading to the dephasing of the qubit. That is why this regime is suboptimal, and the next regime we will consider is much better.

Transmon $E_C \ll E_J$ regime

A large capacitor $\sim 100 \mu\text{m}$ size allows to achieve it. Low-lying levels are localized in the minima of the potential, and the tunneling between these minima, also called phase slips, is exponentially suppressed. The

tight-binding spectrum for the m -th band is:

$$E_m(n_g) = \omega_p(m + 1/2) - \frac{\epsilon_m}{2} \cos(2\pi n_g). \quad (1.13)$$

ϵ_m is given by a WKB formula, which is true also for the lowest levels, where the usual WKB does not work [26]:

$$\epsilon_m \simeq (-1)^m \frac{2^{4m+5}}{m!} \sqrt{\frac{2}{\pi}} \left(\frac{E_J}{2E_C} \right)^{\frac{m}{2} + \frac{3}{4}} e^{-\sqrt{8E_J/E_C}}. \quad (1.14)$$

$\omega_p = \sqrt{8E_J E_C}$ is called plasma frequency, which corresponds to the harmonic oscillations in the quadratic part of the Josephson potential. The sensitivity of the spectrum to n_g (also called charge dispersion) is exponentially small, but the energy levels are almost harmonic again. Nevertheless, an algebraically small anharmonicity $\sim \sqrt{E_C/E_J}$ that remains is sufficient. To illustrate the limits mentioned above, the spectra at various E_J/E_C ratios are plotted in the Figure ??.

1.3.2 Fluxonium qubit

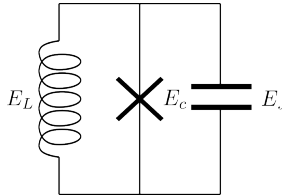


Figure 1.3. Fluxonium circuit

Another way to eliminate the charge dispersion while maintaining a much larger level of anharmonicity is to implement it in another type of superconducting qubit called fluxonium [27, 28]. The idea is to get rid of the superconducting island by shunting it with an inductor:

$$\hat{H} = 4E_C(\hat{n} - n_g)^2 + \frac{1}{2}E_L \left(\hat{\phi} + \phi_{ext} \right)^2 - E_J \cos \phi. \quad (1.15)$$

E_L is related to the inductance as $E_L = (\Phi_0/2\pi)^2/L$ and ϕ_{ext} is related to the flux threaded through the loop $\phi_{ext} = \Phi/\Phi_0$, where $\Phi_0 = h/2e$ is the flux quantum. The charge on the island is not quantized anymore, so any induced charge n_g in the kinetic term can be gauged away, and

the spectrum is insensitive to it. Phase slips can also happen in the inductor, introducing infinitely many copies of the inductive term shifted by 2π . However, if the phase slips happen at time scales much larger than the time scale of the experiment, it's sufficient to keep only one. Despite the simplicity of the Hamiltonian, its physics is very rich. We focus on the regime where $E_L \ll \omega_p$ & $E_C \ll E_J$. For the analysis, it is convenient to write the Hamiltonian in the basis of the Bloch waves $\Psi_{p,s}(\phi) \equiv \langle \phi | s, p \rangle = e^{-ip\phi} u_{p,s}(\phi)$. $u_{p,s}(\phi + 2\pi) = u_{p,s}(\phi)$ is periodic and diagonalizes the 'transmon' part:

$$\left(4E_C(\hat{n} - p)^2 - E_J \cos \phi\right) u_{p,s} = E_s(p) u_{p,s}. \quad (1.16)$$

$p \in (0, 1]$ denotes the 'quasi-momentum' and s denotes the band index. $\Psi_{p,s}(\phi)$ are the functions of the non-compact phase and form a complete orthonormal basis if $u_{p,s}$ are normalized to 1 on the circle $\phi \in (0, 2\pi]$. The phase $\hat{\phi}$ in the basis is expressed as follows:

$$\hat{\phi} = -i\partial_p + \hat{\Omega}. \quad (1.17)$$

The matrix elements of this operator [27, 29]

$$\langle p, s | \hat{\Omega} | p', s' \rangle = \delta(p - p') \Omega_{s,s'}(p) \quad (1.18)$$

$$\Omega_{s,s'}(p) = - \left(\frac{2E_C}{E_J} \right)^{1/4} \left(\sqrt{s} \delta_{s+1,s'} + \sqrt{s+1} \delta_{s',s-1} \right) \quad (1.19)$$

can be neglected in our limit, such that the Hamiltonian has a block-diagonal structure:

$$H_s = \frac{E_L}{2} (-i\partial_p + \phi_{ext})^2 + E_s(p). \quad (1.20)$$

The wavefunctions in this basis are also periodic $\psi_s(p+1) = \psi_s(p)$. Because $E_s(p) = E_s(1/4) - \frac{\epsilon_s}{2} \cos 2\pi p$ (1.13), this Hamiltonian is dual (under the exchange of the quasi-charge and the phase) to transmon. Hence, we discuss the two regimes again.

Usual fluxonium $E_L \gg \epsilon_s$ regime

The reason for the title is that it is the most common fluxonium regime, which is the easiest to achieve experimentally. Like in the $E_C \gg E_J$ regime

of transmon, E_s is a perturbation on the top of the kinetic $\frac{E_L}{2}(-i\partial_p + \phi_{ext})^2$ term, whose eigenstates are fluxons:

$$|2\pi m, s\rangle = \int_0^1 dp e^{i2\pi mp} |p, s\rangle, \quad m \in \mathbb{Z}. \quad (1.21)$$

This is again a complete basis of states [27, 29]. In the phase representation, the fluxons $\langle \phi | 2\pi m, s \rangle$ are states localized around $\phi = 2\pi m$ minima of the Josephson energy, originating from the s -th harmonic levels. $E_s(p)$ acts like a weak scattering potential, coupling neighbouring fluxons and introducing the avoided crossings. Similarly to the Cooper pair box, the levels are highly anharmonic, but the spectrum depends strongly on the flux bias ϕ_{ext} . One can operate the qubit at $\phi_{ext} = \pi$, where one of the avoided crossings for the lowest band happens, and the first derivative of the energy difference with flux vanishes. This is a so-called sweet spot where most of the modern fluxoniums are operated. In the phase ϕ space, the $|0\rangle, |1\rangle$ wavefunctions are the symmetric and antisymmetric superpositions of fluxons localized at $\phi = -2\pi$ and $\phi = 0$. Extremely large coherence times were achieved with this type of qubit, of the order of 1ms [30–33].

Blochnium $E_L \ll \epsilon_s$ regime

This regime is tough to achieve, as it requires very small inductances due to the exponential suppression of the phase slips. Thus, this regime has been reached experimentally only marginally [34]. The lowest states are localized in the quasi-charge minima of $E_0(p)$ and are dual to those in the transmon $E_J \gg E_C$ regime. Hence, in this regime, the qubit's energies are insensitive to both n_g and ϕ_{ext} fluctuations, which is why achieving it would be highly desirable.

1.4 Minimally twisted bilayer graphene

It was predicted more than 10 years ago that stacking two graphene layers at the top of each other at a small angle ($\theta \sim 1^\circ$) leads to the appearance of flat bands [35, 36]. Flat bands enable a variety of strongly correlated phenomena and remarkable tunability of the material [37–39], the study of which led to the emergence of a new field: twistrionics [40]. However, also at small angles $\sim 0.1^\circ$, where interactions can be neglected in certain cases,

interesting physics can happen [41–43]. The magnetotransport properties of such a material, called minimally twisted bilayer graphene, are discussed in Chapter 5 and Chapter 6.

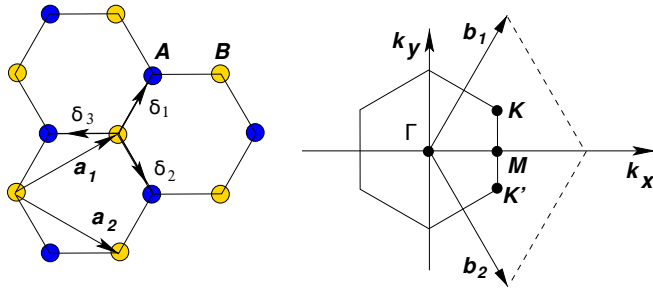


Figure 1.4. Graphene honeycomb lattice and its Brillouin zone. *Reprinted figure with permission from A. H. Castro Neto, F. Guinea, N. M. R. Peres, K. S. Novoselov, and A. K. Geim, Rev. Mod. Phys. 81, 109, 2009. Copyright (2009) by the American Physical Society.*

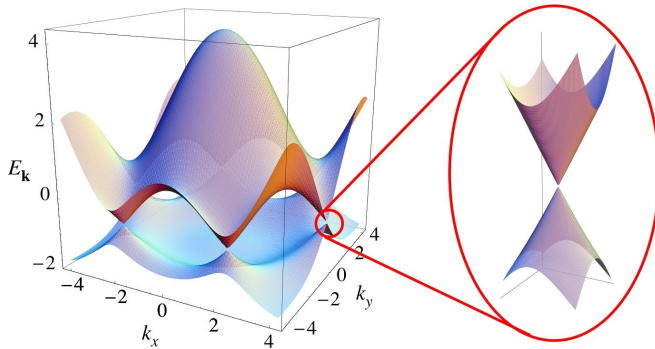


Figure 1.5. Graphene band-structure. *Reprinted figure with permission from A. H. Castro Neto, F. Guinea, N. M. R. Peres, K. S. Novoselov, and A. K. Geim, Rev. Mod. Phys. 81, 109, 2009. Copyright (2009) by the American Physical Society.*

First, we recall the basic properties of single-layer graphene. The material is made of carbon atoms arranged in a hexagonal 2D lattice (lattice constant 2.46 \AA) [44]. The unit cell has two atoms 1.4, which are usually named A and B. Figure 1.6 shows the band structure in the simplest tight-binding model. There are two special points (K and K') in the Brillouin zone where the two Dirac cones are (Fig. 1.5), with linear dispersion

relations $E = \pm v_F |k|$ in their neighbourhoods. The value of v_F is of the order of 10^6 m/s. The valley (K or K') index becomes an almost good quantum number at low enough energies and in the absence of short-scale disorder.

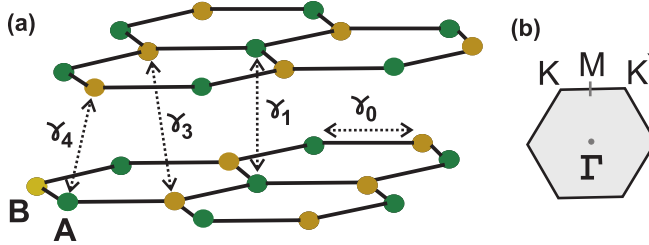


Figure 1.6. Lattice structure of Bernal AB stacking configuration of bilayer graphene and the corresponding Brillouin zone. *Reprinted figure with permission from A. H. Castro Neto, F. Guinea, N. M. R. Peres, K. S. Novoselov, and A. K. Geim, Rev. Mod. Phys. 81, 109, 2009. Copyright (2009) by the American Physical Society.*

Second, we introduce Bernal stacked bilayer graphene, which is the lowest energy stacking configuration. In an AB (BA) configuration, the B(A) atoms will be on the top of the centres of the hexagons in the bottom layers (Fig. 1.6). The effect on the band structure is that the Dirac cones from the two layers hybridize and become parabolas, as shown in the Figure 1.7. Two of these parabolas touch at each Dirac point. If a perpendicular electric field is applied (by gating the material), a gap proportional to the strength of the field opens. As a result, the material becomes a semiconductor with a tunable gap. Another important feature is that each valley has a non-trivial Chern number ± 1 , even though the total Chern number is 0 [44].

Finally, when the two layers are stacked at a very small $\sim 0.1^\circ$ angle, a superlattice with a large ~ 100 nm unit cell appears [45–47]. Such twist angles can even happen in nature [48]. Because Bernal stacking is the lowest energy configuration [44], the lattice will relax into sharply defined triangular AB/BA domains, as shown in the Figure 1.8. As already explained, the domains become gapped if a perpendicular electric field is applied. Gapped AB and BA domains will have the opposite (± 1) Chern numbers for a fixed valley index. As a result, a topological phase transition happens across each domain wall, and because the Chern number changes by 2, there will be two chiral modes around each domain for one valley and

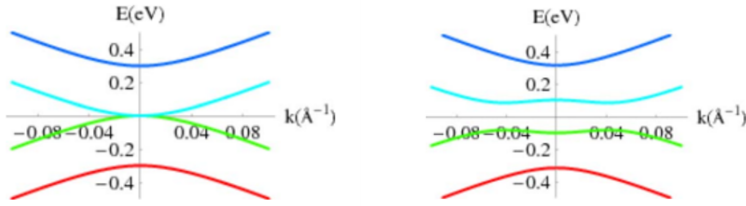


Figure 1.7. *Left panel:* Band-structure of Bernal stacked bilayer graphene *Right panel:* Band-structure of Bernal stacked graphene with perpendicular electric field applied. *Reprinted figure with permission from: A. H. Castro Neto, F. Guinea, N. M. R. Peres, K. S. Novoselov, and A. K. Geim, Rev. Mod. Phys. 81, 109, 2009. Copyright (2009) by the American Physical Society.*

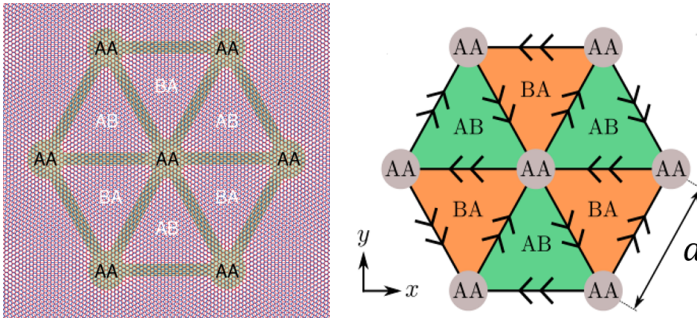


Figure 1.8. *Left panel:* Moire pattern of minimally twisted bilayer graphene *Reprinted figure with permission from J. D. Verbakel, Q. Yao, K. Soththewes, and H. J. W. Zandvliet, Phys. Rev. B 103, 165134, 2021. Copyright (2021) by the American Physical Society.* *Right panel:* Network model for transport in electrically gated minimally twisted bilayer graphene. *Reprinted figure with permission from C. De Beule, F. Dominguez, and P. Recher Phys. Rev. Lett. 125, 096402, 2020. Copyright (2020) by the American Physical Society.*

spin. The network of these states was experimentally observed with STM [48, 49], and the absence of inter-valley scattering due to disorder, which is crucial for the arguments, was confirmed as well [48]. The direction of propagation of the modes is reversed for the opposite valley, which ensures the T -reversal symmetry. Typically, it's assumed that the modes propagate ballistically along the boundaries of the domains and scatter according to some scattering matrix in the nodes with AA alignment of the atoms [41, 43]. This model was successful in describing magnetotransport experiments [50, 51].

1.5 Bloch oscillations

An important concept that will be encountered in Chapter 5 and Chapter 6 is Bloch oscillations. This is one of the counterintuitive phenomena in crystals: if a weak electric field is applied, the velocity of the electrons will oscillate with frequency eEa (where E is the strength of the electric field and e is the charge of the electron) due to the Bragg reflection [52, 53]. Despite early predictions, it has not been measured in a crystal, as for the typical electric fields and lattice constants, the mean free times of the electrons are typically too low. However, it's been observed in superlattices [54–58] and a mathematical analogue of Bloch oscillations in minimally twisted bilayer graphene, which should be possible to observe, will be discussed in the Chapter 5.

The simplest model where Bloch oscillations can be explained is a 1D tight-binding model of non-interacting electrons in a lattice. The dispersion relation will be $E = h \cos ka$, where a is the lattice constant, k is the quasi-momentum and h is the hopping strength. If a sufficiently weak electric field is applied to the crystal, such that the single-band model stays intact, this will generate a force on the electrons $\dot{k} = -eE$. The equation is trivial to integrate: $k(t) = k_0 - eEt$. This means that the velocity $v(k) = \partial_k E$ of each electron will oscillate in time due to the periodicity in k dispersion relation, and an AC current will be generated.

If we imagine a semi-classical wave-packet, localized around $z(0)$ at the lengthscale $\gg a$ with some quasi-momentum $= q$, its position will oscillate in time too:

$$z(t) - z(0) = \int_0^t \partial_k \epsilon(k) dt' = \frac{h}{eE} (\cos(k_0 a - eE t a) - \cos(k_0 a)). \quad (1.22)$$

However, if the wave packet is localized only at the scale of one lattice constant, and the quasimomentum is not well-defined, the probability density will have the oscillation pattern of the so-called breathing mode [59], shown in the Figure 1.9. The horizontal axis corresponds to time and the vertical axis corresponds to the position (z). The wave packet returns to the initial lattice site exactly after one period of oscillations: $T = \frac{2\pi}{eEa}$, unlike in the semi-classical case, where such return happens twice during the period.

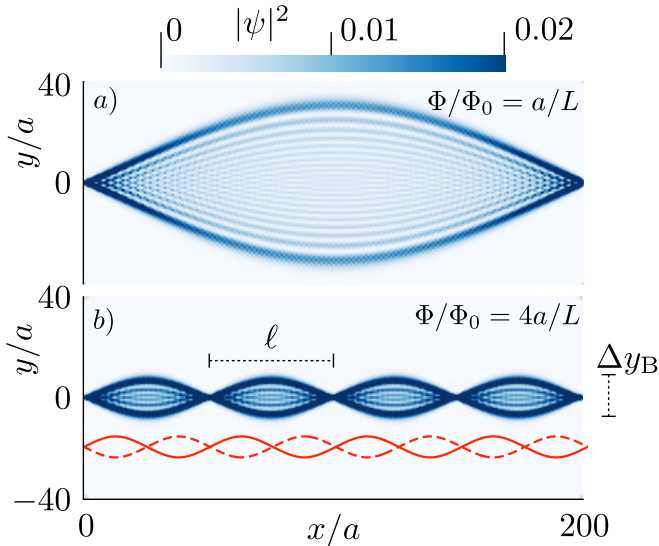


Figure 1.9. Breathing mode for a state initially localized at the origin. The colour scale stands for the probability density of the wave packet. The image below illustrates that the semi-classical wavepacket returns to the origin twice during one Bloch period of oscillation, while the breathing mode does so only once

1.6 Altermagnets

There are two well-known magnetic phases that have collinear spins and are enabled by exchange interactions: ferromagnetism and antiferromagnetism. However, in the recent 5 years, a new, third phase was theoretically predicted: altermagnetism [60–63]. It shares some similarities with both phases. Like in ferromagnets, the time-reversal symmetry is broken, which leads to the anomalous Hall effect [63–66], confirmed experimentally in semiconducting MnTe [67] and metallic RuO₂ [68]. Like antiferromagnets, altermagnets have no net magnetization [64, 65, 69, 70]. However, there are also cases where altermagnets behave like neither of the two, one of them will be considered in this thesis.

The simplest Neel antiferromagnet can be seen as follows. Let’s imagine a 1D crystal lattice of magnetic ions having collinear spins. Every second spin is flipped with respect to the neighbouring spin, and one can divide the chain into two opposite spin sub-lattices, which are related by a translation by one unit cell. Since the Hamiltonian should be sym-

metric under such a translation, for both spins the electronic dispersion relation will be the same and the Hamiltonian will be time-reversal symmetric, hence the 0 net polarization. Also more sophisticated versions of antiferromagnets exist, where two spin sub-lattices can be connected by inversion. However, the magnetic properties of such materials are the same as those of the Neel antiferromagnets at the qualitative level [69].

Another possibility can theoretically happen; when two sub-lattices are related by neither inversion nor translation. For example, it can be a rotation, like in RuO_2 [64, 71]. Because the atoms with opposite spins are rotated by $\pi/2$ relative to each other, the dispersion relations for the two spins are no longer the same, but related by the same rotation. A

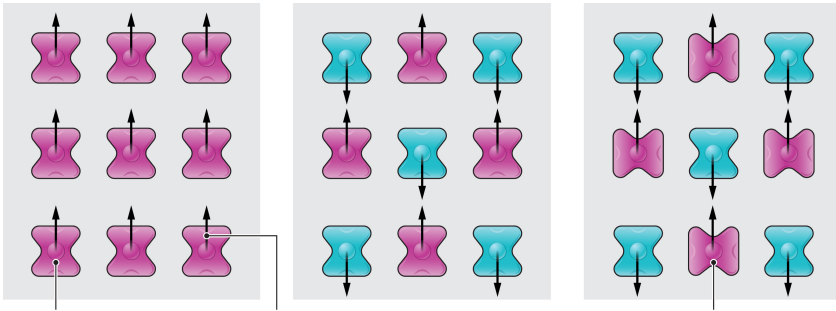


Figure 1.10. Example configurations of spins and atoms for three magnetic phases: ferromagnetism, antiferromagnetism and altermagnetism. In altermagnetic RuO_2 , atoms with opposite spins are rotated by $\pi/2$. *From Savitsky, Zack. "Researchers discover new kind of magnetism." Science (New York, NY) 383.6683 (2024): 574-575. Reprinted with permission from AAAS.*

minimal model for such a material is the following [72] (Fig. 1.11):

$$H = \frac{1}{2m} (k_x^2 + k_y^2) \sigma_0 - t(k_x^2 - k_y^2) \sigma_z, \quad (1.23)$$

where k_x, k_y are the momenta and σ_z is the Pauli matrix acting in the spin space. The first term corresponds to the usual isotropic contribution and the second term is the altermagnetic one. This term is also referred to as d-wave magnetism – a magnetic counterpart to the d-wave superconducting order parameter (in that sense, s-wave magnetism is a ferromagnet) [65]. It's immediately obvious that the time-reversal symmetry is broken, and the Fermi-surface is spin-split. These two important signatures have been recently verified experimentally [71, 73]. Nevertheless, the net

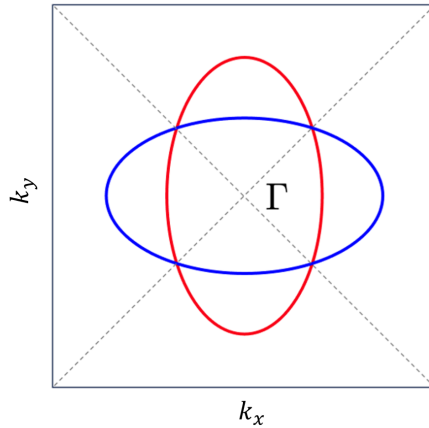


Figure 1.11. Fermi surface of an altermagnetic material. Blue colour stands for the spin up and red colour stands for the spin down. *By Libor Šmejkal - Provided by the author, CC BY-SA 4.0.*

magnetization is 0, since the two Fermi-surfaces are the same up to the rotation. Note, that unlike spin-orbit coupling, which doesn't break time-reversal symmetry, this interaction is quadratic in momentum and is of non-relativistic origin (it can be caused by exchange interactions, as mentioned in the beginning). Due to the latter fact, t is predicted to be quite large in some materials, up to ~ 1 eV [65, 72, 74].

Despite the recent discovery, this phenomenon is believed to be quite common; there are dozens of such materials already [65], some of them (such as MnTe) were initially believed to be antiferromagnets [75]. One of the experimental obstacles is the existence of domains, which makes many of the predicted effects cancel [76]. Despite the difficulty, this novel magnetic phase is worth studying from both fundamental and practical points of view, as the unique combination of spin-polarized Fermi surface and the absence of net magnetization makes it a promising material for spintronics [65].

A relatively recent direction of research is the study of the interplay between superconductivity and altermagnetism. A number of interesting phenomena have been already discovered: orientation-dependent Andreev reflection [77, 78], π Josephson junction [8, 9] and topological Majorana modes [79, 80]. In Chapter 4 we study the second effect in a more microscopic and non-perturbative way by calculating the Andreev Bound states'

spectrum for arbitrary transparency. We recover the π junction behaviour and observe a large anisotropy with respect to the orientation of the altermagnet in the normal part. This provides us with an example when altermagnet behaves neither as a ferromagnet, nor an antiferromagnet: an antiferromagnetic junction wouldn't show the π junction behaviour, but a ferromagnetic junction doesn't have such large anisotropy.

1.7 This thesis

Bellow I briefly highlight the main results presented in the thesis.

1.7.1 Chapter 2

In the second chapter, we compute analytically the amplitudes of 2π and 4π phase slips occurring in a resonant level capacitively shunted Josephson junction, which determines the charge dispersion of the transmon qubit. The amplitude for quantum tunneling under the Josephson potential barrier is modified by the Landau-Zener amplitude of adiabatic passage through an Andreev level crossing, resulting in the suppression of 2π phase slips. The Landau-Zener amplitude vanishes when the level is on resonance with the Fermi energy in the leads and the couplings are symmetric (which corresponds to high effective transparency of the junction). As a consequence, 4π phase slips become the dominant tunneling process. The analytical expressions demonstrate this crossover, showing that a very small residual charge dispersion persists even at perfect transparency. These results are of relevance to the experimental observation of the vanishing charge dispersion in the InAs-Al shell nanowire transmons [16, 17].

1.7.2 Chapter 3

The next chapter considers a fluxonium circuit consisting of a capacitively shunted resonant level junction in parallel with an inductor. In the high-transparency regime discussed in 1.7.1, fluxons are predominantly coupled by 4π quantum phase slips. This regime implies that, at the sweet-spot $\phi_{ext} = \pi$, the avoided crossings between (anti-)symmetric superpositions of degenerate fluxons separated by phase 2π should disappear. We calculate how the fluxonium spectrum is affected by the presence of the resonant level using low-energy WKB for arbitrary effective transparency. We also

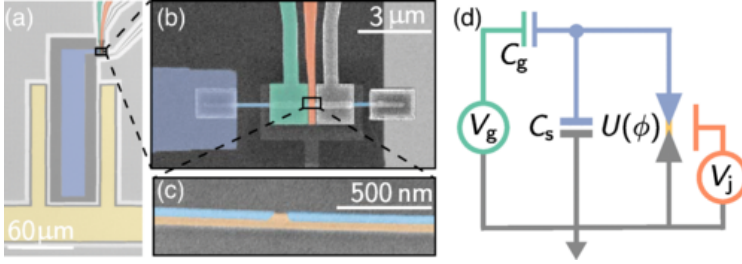


Figure 1.12. A nanowire transmon device where the vanishing charge dispersion was observed [16]. *Reprinted figure with permission from Arno Bargerbos, Willemijn Uilhoorn, Chung-Kai Yang, Peter Krogstrup, Leo P. Kouwenhoven, Gijs de Lange, Bernard van Heck, and Angela Kou Phys. Rev. Lett. 124, 246802 (2020). Copyright 2020 by the American Physical Society.*

show that if the inductive energy of the loop is much smaller than the plasma frequency of the junction, the low-energy Hamiltonian of the circuit is dual to that of a topological superconducting island. These findings can inform experiments on bifluxon qubits as well as the design of novel types of protected qubits.

1.7.3 Chapter 4

In the fourth chapter, we move away from the qubit applications and consider a hybrid planar Josephson junction with an altermagnet (d-wave magnet) inside the normal part. We compute the effect of the altermagnet on the Andreev bound state spectrum in a non-perturbative way, assuming the short junction limit. Unlike in a non-magnetic Josephson junction, the Andreev bound states with opposite spins acquire opposite phase shifts $E(\phi \pm \delta\phi)$, such that the spectrum becomes spin-polarized. When the magnetic order has pure d_{x-y} symmetry with respect to the y direction perpendicular to the junction, the Andreev bound state spectrum acquires a simple form:

$$E = \Delta_0 \sqrt{1 - T(k_y) \sin^2 \frac{1}{2}(\phi \pm \delta\phi(k_y))}, \quad (1.24)$$

where k_y is the transversal momentum (which is a good quantum number here), T is the transparency of the mode with such a transversal momentum and $\delta\phi$ is a phase shift that depends on the length of the junction, altermagnetic coupling, k_y and is opposite for opposite spins. We

also calculate the corresponding total Josephson energy and supercurrent, recovering the possibility of π -junction behaviour, which was predicted earlier [8, 9].

1.7.4 Chapter 5

In this chapter, we investigate the magnetotransport in minimally twisted bilayer graphene. We use a well-established network model [41–43, 48, 49, 81, 82] of chiral ballistic modes (arranged in a triangular network), which applies to samples where the inter-valley scattering can be neglected and an additional perpendicular field is applied. In a certain parametric regime of the phenomenological model (which is expected to hold in the real samples), the 2D transport can be mapped to a 1D random walk. One of the spatial dimensions (along which backscattering of the ballistic modes is not possible) maps to time in the random walk, and the perpendicular magnetic field is mapped onto the electric field. In this way, a mathematical analogue of 1D Bloch oscillations can be observed in the 2D magnetotransport of minimally twisted bilayer graphene, as the oscillations in the magnetoconductance with the magnetic field will have periodicity set by the Bloch frequency.

1.7.5 Chapter 6

The last chapter concerns magnetotransport in 2D materials with open Fermi surfaces, which is a generalization of the model considered in the previous chapter. The stationary Schroedinger equation in the presence of the magnetic field can be mapped to the evolution equation of a particle in a 1D crystal in the presence of an electric field (where time maps to the spatial direction x in which the orbit is open). Due to the Bragg reflection in the 1D crystal as the particle reaches the Brillouin zone boundary, the spatial profile of the corresponding 2D density profile will show periodicity with x . If the wave-function is localized at the lengthscale of the unit cell for a certain x_0 , it will be refocused after $\Delta x = (eaB/h)^{-1}$ (a is the lattice constant and B is the magnetic field). Unlike the usual magnetic focusing effect due to the Lorentz force with the focal length $\frac{k_F}{eB}$ (k_F – Fermi momentum), the focusing effect in this chapter is intrinsically quantum.

Chapter 2

Quantum phase slips in a resonant Josephson junction

2.1 Introduction

The phase difference across a Josephson junction can be driven by quantum fluctuations to change, or "slip", by integer multiples of 2π [83]. Such quantum phase slips often determine the low-frequency behavior of microwave superconducting circuits [84–89]. In a long chain or loop of Josephson junctions, or in thin superconducting wires or rings, quantum phase slips compromise the spatial stiffness of the phase and can suppress superconductivity [90–97]. In general, quantum phase slips affect the energy levels of a coherent superconducting circuit [98] and can therefore be measured with spectroscopic methods.

For instance, in a Cooper-pair-box circuit [24, 99, 100] in the transmon limit [26], quantum phase slips determine the charge dispersion of the energy levels [26], i.e. the magnitude of their oscillation as a function of the charge induced on the superconducting island [see figure 2.1(a-b)]. The charge dispersion of the fundamental frequency of the circuit is particularly important since it controls the dephasing time of superconducting qubits [26]. This fact motivated the development of the transmon [26], where the quantum phase slip amplitude is suppressed by a large ratio of the Josephson energy E_J and the charging energy E_C , resulting in an exponential suppression of the charge dispersion [101].

Setting aside qubit applications, devices with an appreciable charge dispersion remain of fundamental interest: thanks to their sensitivity

to charge parity, they can be used to study quasiparticle poisoning and dynamics [102–107], and, in a possible future, to measure fermion parity in topological Majorana qubits [108, 109]. These ongoing developments welcome further theoretical study of quantum phase slips, particularly given the emergence of hybrid semiconducting-superconducting qubit devices [110] and novel designs of noise-protected superconducting qubits [111].

In this chapter, we compute in detail the amplitude of quantum phase slips in a Josephson junction with a resonant energy level. We describe and pay particular attention to the competition between coherent 2π and 4π quantum phase slips that occurs in such a junction. The competition is controlled by two independent parameters: the energy of the resonant level and the asymmetry between the tunneling rates to the superconducting leads. The 4π phase slips become dominant close to resonance, and we argue that even though they were too small to be detected in recent experiments [16, 17], they can be observed in devices with a larger charging energy. Towards the end, possible implications for qubit designs are also discussed. The next section motivates our calculations, placing them in the context of previous theoretical and experimental research.

2.2 2π and 4π quantum phase slips

The amplitude of coherent quantum phase slips in a weak link is given by the tunneling amplitude between neighboring minima of the Josephson potential energy. This amplitude can be qualitatively affected by the type of weak link where the phase slip occurs. Figure 2.1(c-e) compares three simple but paradigmatic scenarios: a low-transparency tunnel junction (S-I-S); a highly transparent single-channel quantum point contact (S-QPC-S); and finally a junction with a resonant level (S-R-S). As we argue below, so far the S-R-S scenario has not been fully understood and described, despite its experimental relevance.

Figure 2.1(c) illustrates the familiar setting of a tunnel junction, such as a quantum point contact close to pinch-off or an Al oxide junction, for which the potential energy is $\approx E_J(1 - \cos\phi)$ ¹. Quantum phase slips

¹A low-transparency QPC differs from an oxide junction because in the former the entire phase dispersion of the ground state originates from a single transport channel, and thus a single Andreev bound state, while in the latter from hundreds or even thousands of transport channels. The two junctions have equivalent ground state prop-

connect the neighboring minima of the cosine potential, distant by 2π and, when $E_J \gg E_C$, they are suppressed exponentially with $\sqrt{E_J/E_C}$ [26]. This classic result can be obtained using the WKB method or an instanton approach to the cosine potential [112, 113]. The charge dispersion of the energy levels is $2e$ -periodic and, while exponentially small, remains finite at any value of E_J due to the presence of back-scattering at the tunnel junction.

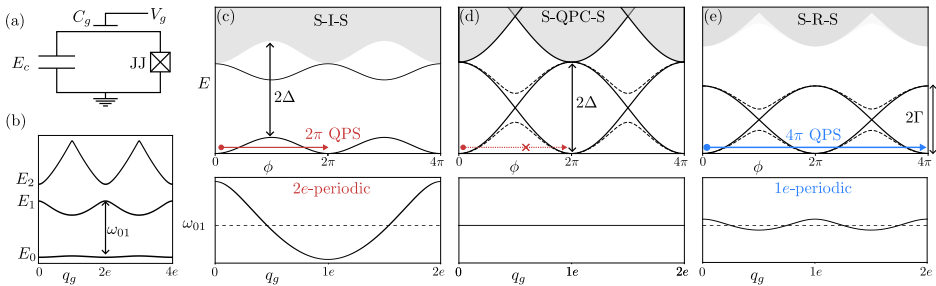


Figure 2.1. (a): A Cooper pair box consists of a superconducting island connected to ground by a capacitor and a Josephson junction. A gate voltage V_g controls the charge induced on the island, $q_g = C_g V_g$. In the transmon limit of the Cooper pair box, the charging energy E_C is much smaller than the Josephson tunneling strength. (b) The energy levels E_n of the Cooper pair box oscillate with n_g . The resulting charge dispersion can be determined by measuring the fundamental frequency $\omega_{01} = E_1 - E_0$ as a function of n_g , for instance via microwave spectroscopy. (c-e) Schematic energy spectrum of three different types of Josephson weak links (top row) and corresponding charge dispersion oscillations in the Cooper-pair box (bottom row). (c): $2e$ -periodic dispersion due to 2π quantum phase slips in a tunnel junction. (d): Absence of charge dispersion in a quantum point contact at perfect transparency. (e): $1e$ -periodic dispersion due to 4π quantum phase slips in a junction with a resonant energy level (e). Dashed lines in (d) and (e) show the Josephson potential away from perfect transparency, in which case 2π phase slips are weakly restored.

By contrast, figure 2.1(d) shows the case of a quantum point contact at perfect transparency. Its distinctive feature is the presence of a level crossing that disconnects the neighboring minima of the Josephson potential. In fact, since each potential branch touches the continuum states at $E = 2\Delta$, the Josephson potential is a-periodic [114]. As a consequence, quantum phase slips are forbidden altogether and the charge dispersion

erties, but different densities of states close to the gap edge; the sketch in figure 2.1c schematically depicts the first case.

vanishes [114–116]. Away from perfect transparency, the level crossing becomes a narrowly avoided crossing. Quantum phase slips may then occur again, but only if the phase slips adiabatically through the crossing. Hence, they are suppressed by the associated Landau-Zener transition amplitude and, near perfect transparency, it remains much smaller than in a S-I-S junction with comparable Josephson energy.

This enhanced suppression of the charge dispersion has been recently observed in spectroscopic measurements of transmon qubits realized with hybrid InAs/Al nanowire Josephson junctions [16, 17]. However, in these experiments the condition of almost perfect transparency was achieved by fine-tuning the nanowire junction to a resonance. As shown in figure 2.1(e), this scenario differs qualitatively from that of a quantum point contact.

The normal-state transmission probability of a quantum point contact does not depend on energy on scales compared to the gap Δ , while in the presence of a resonance it is a peaked function of energy, with a characteristic width Γ that can be much smaller than Δ . As a consequence, the Andreev levels in the resonant case are detached from the continuum of energy levels even at zero phase difference [117, 118], while they always touch the gap edge for a quantum point contact [15].

This difference has important consequences for quantum phase slips: if perfect transmission is achieved resonantly, the Josephson potential consists of two 4π -periodic branches [18]. Thus, one expects 4π phase slips to occur even when 2π phase slips are forbidden. As a result, one predicts a finite charge dispersion at resonance, but with a modified periodicity of $1e$ rather than $2e$. In this respect, the situation is similar to that of a topological Josephson junction with coupled Majorana zero modes [119, 120], with the crucial difference that in the resonant junction the two branches of the potential have the same fermion parity.

Given this scenario, it is appropriate to revisit quantum phase slips in the presence of a resonance, using as a starting point the existing knowledge on resonant Josephson tunneling [117, 118, 121, 122], which has seen a revival [18] in view of experimental progress on microwave measurements of Andreev bound states [123–126].

2.3 Model

We consider a minimal model for a resonant Josephson junction in which the current between two superconducting electrodes is mediated via a single spin-degenerate energy level (see figure 2.2). The parameters of the model are the two tunneling rates Γ_1 and Γ_2 between the leads and the resonant level, and the energy ϵ_r of the resonant level, measured with respect to the Fermi level in the leads. In what follows, we will refer to ϵ_r as the detuning.

We consider the case in which $\Gamma_{1,2} \ll \Delta$, the superconducting gap in the leads. In this limit, it is possible to integrate out the fermionic degrees of freedom of the superconductors and obtain a simple effective Hamiltonian for the coupled dynamics of the superconducting phase difference ϕ and of the resonant level. The effective Hamiltonian is

$$H = 4E_C(i\partial_\phi + n_g)^2 + V(\phi) \quad (2.1)$$

Here, E_C is the charging energy between the two electrodes, and $n_g = q_g/(2e)$ the charge induced by the electrostatic gates coupled to them, measured in units of $2e$. The operator $-i\partial_\phi$ counts the number of Cooper pairs transferred between the two superconductors. The matrix-valued potential energy $V(\phi)$ is [18–21]

$$V = -\epsilon_r \tau_z - \Gamma \cos(\phi/2) \tau_x - \delta\Gamma \sin(\phi/2) \tau_y, \quad (2.2)$$

where we have introduced the total tunneling rate

$$\Gamma = \Gamma_1 + \Gamma_2, \quad (2.3)$$

and the asymmetry parameter

$$\delta\Gamma = \Gamma_1 - \Gamma_2. \quad (2.4)$$

The Pauli matrices $\tau_{x,y,z}$ encode the dynamics of the two-level system in which the resonant level is either empty ($\tau_z = +1$) or occupied by a Cooper pair ($\tau_z = -1$).

The adiabatic eigenvalues $\pm E_A$ of the potential in Eq. (2.2) reproduce the well-known formula for the Andreev levels in a single-channel junction:

$$E_A(\phi) = \sqrt{\epsilon_r^2 + \Gamma^2 \cos^2(\phi/2) + \delta\Gamma^2 \sin^2(\phi/2)} \quad (2.5)$$

$$\equiv \Gamma_A \sqrt{1 - T \sin^2 \phi/2}, \quad (2.6)$$

with $\Gamma_A^2 = \Gamma^2 + \epsilon_r^2$ and $T = 1 - |r|^2$ the transparency of the junction, controlled by the reflection coefficient

$$r = \frac{\epsilon_r + i\delta\Gamma}{\Gamma_A}. \quad (2.7)$$

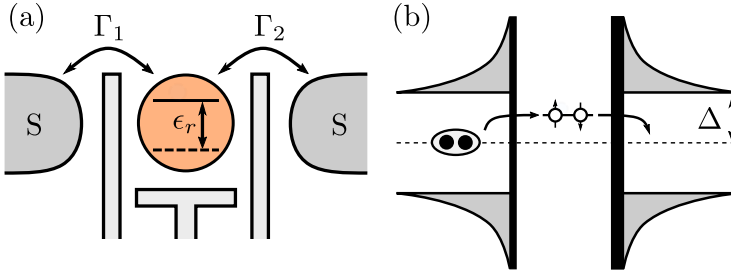


Figure 2.2. Illustration of the model of Eqs. (2.1) and (2.2). (a): A Josephson junction consisting of quantum dot (orange) with a single energy level. The detuning ϵ_r of the energy level from the Fermi level of the leads and the tunneling rates Γ_1 , Γ_2 can be controlled via gate electrodes. (b): Transport of Cooper pairs across the two insulating barriers is mediated by the spin-degenerate resonant level.

The salient features of the Andreev spectrum are the following. First, at perfect transparency, which is achieved when $\epsilon_r = \delta\Gamma = 0$ so that $r = 0$, the spectrum evolves into two decoupled, 4π -periodic branches with energy $\pm\Gamma \cos(\phi/2)$, with a zero-energy level crossing at $\phi = \pi$. Second, as long as $\Gamma_A \ll \Delta$, the Andreev bound state energy is well detached from the continuum spectrum for all values of ϕ , including $\phi = 0$ [see figure 2.1(e)]. This fact, in particular, justifies neglecting excited states in the continuum when considering the adiabatic dynamics of the phase difference.

The derivation of the effective Hamiltonian of Eq. (2.1), which is carried out in appendix ??, also yields the appropriate boundary condition for the spinor wave functions

$$\Psi(\phi + 2\pi) = \tau_z \Psi(\phi). \quad (2.8)$$

This twisted boundary condition incorporates a constraint on the dynamics that comes from charge conservation: if a Cooper pair occupies the resonant level, it must be subtracted from one of the two superconductors. In other words, the tunneling of a Cooper pair between one of the

two superconductors and the dot counts as *half* of a Cooper pair transfer between the two superconductors. This is the humble origin of the 4π -periodicity of the tunneling terms in the effective Hamiltonian.

We also point out that, despite the complete similarity at the level of the Andreev spectrum, Eq. (2.5), the effective two-level Hamiltonian of Eq. (2.1) is not the same as the corresponding two-level Hamiltonian for a quantum point contact [127, 128]. Besides the aforementioned fact that the Andreev levels are fully detached from the continuum, the main physical difference is that in the limit $T \rightarrow 0$ a sub-gap state is present in the resonant level model (provided that ϵ_r is small enough), while no sub-gap state remains for the quantum point contact.

These circumstances can be elucidated by inspecting the energy spectrum in the absence of tunneling, at $\Gamma_1 = \Gamma_2 = 0$, see figure 2.3(a). It consists of familiar parabolas with energy $E = 4E_c (n - n_g)^2$, each corresponding to a charge $q = 2en$ transferred between the superconductors. If the resonant level is empty, n is integer, leading to a set of parabolas centered around integer values of n_g . On the other hand, if the resonant level is occupied, n is half-integer, leading to a second set of parabolas centered around half-integer values of n_g . The resulting energy spectrum is always at least $2e$ -periodic as a function of n_g , and it becomes $1e$ -periodic if $\epsilon_r = 0$. If $|\epsilon_r| < E_C$, as in figure 2.3(a), there are two degeneracy points per period at which parabolas cross, otherwise only a single degeneracy point per period remains.

The effect of small but finite tunneling rates on the energy spectrum is shown in figure 2.3(b). A small Γ_1 hybridizes the resonant level with the left superconductor, and thus opens avoided crossings at the degeneracy points between energy levels corresponding to n and $n + \frac{1}{2}$ (with n integer). Conversely, a small Γ_2 hybridizes the resonant level with the right superconductor, and thus opens avoided crossings at the degeneracy points between energy levels corresponding to n and $n - \frac{1}{2}$ (again, with n integer). If the tunneling rates are different, namely if $\delta\Gamma \neq 0$, the avoided crossings have different magnitudes.

These simple arguments indicate that the energy spectrum will be $2e$ -periodic away from the resonant condition in which *both* $\epsilon_r = 0$ and $\delta\Gamma = 0$. At resonance, the energy spectrum is $1e$ -periodic in n_g , as illustrated in figure 2.3(c), since all the charge parabolas are aligned and the hybridization of the resonant level is balanced across the two leads.

Our discussion so far has been perturbative in nature, and it applies

directly to the weak tunneling regime $T\Gamma_A \lesssim E_C$ of figure 2.3. However, the conclusions regarding the periodicity of the energy spectrum remain valid in the strong tunneling regime, where they can be understood in terms of the relative strength of 2π and 4π phase slip amplitudes. This will be the focus of the next section.

2.4 WKB analysis

In this section we are going to derive approximate solutions for the energy levels of the Hamiltonian of Eq. (2.1) under the boundary condition (2.8) using the WKB approximation. The latter applies to the strong tunneling regime, defined as the parameter regime where the bandwidth of the Josephson potential is much larger than the charging energy: $T\Gamma_A \gg E_C$. In this limit, the low-lying energy levels near the bottom of the potential are almost harmonic, with exponentially small corrections dictated by the tunneling under the potential barrier. The calculation of the latter requires particular care near perfect transparency, $|r| \ll 1$.

After moving the induced charge n_g from the Hamiltonian to the boundary condition via a gauge transformation $\Psi \rightarrow e^{i\phi n_g} \Psi$, the problem to be solved is the stationary Schrödinger equation

$$-4E_C\Psi'' + V\Psi = (-\Gamma_A + E)\Psi. \quad (2.9)$$

We have shifted the zero of the energy E to the bottom of the Josephson potential, which is at energy $-\Gamma_A$, so that the eigenvalues are all positive. We are interested in solutions near the bottom of the potential, $E \ll T\Gamma_A$. In the WKB approximation, the solution Ψ is taken to be a wave with a locally-varying wave vector

$$k_{\pm}(\phi) = \sqrt{\frac{E - \Gamma_A \mp E_A(\phi)}{4E_C}}. \quad (2.10)$$

where the \pm index labels the two branches of the potential with energy $\pm E_A$. The wave vector is real (imaginary) when E is above (below) the potential energy.

The periodic boundary conditions (2.8) ensure that we need to solve Eq. (2.9) in a 2π interval, say $[-\pi, \pi]$. In this interval, the $-$ branch has a classically available region between the two turning points at $\pm\phi_c$, which are defined by the condition

$$E - \Gamma_A + E_A(\phi_c) = 0. \quad (2.11)$$

On the other hand, the + branch is classically forbidden in the entire interval, and thus for this branch the WKB ansatz consists of evanescent waves everywhere.

The WKB ansatz fails at the classical turning points, where the WKB momentum vanishes, and also, for small r , at $\phi = \pi$, because the adiabatic eigenstates (i.e. the spinors χ_s such that $V\chi_s = sE_A\chi_s$) rotate rapidly with the phase. In both cases, it is possible to linearize the potential $V(\phi)$ at the problematic boundary and, from the solutions of the resulting differential equations, use the method of matching asymptotes to derive connection formulas for the WKB solutions on the two sides of the boundary. At $\phi = \pm\phi_c$, the linearization involves only the $\sigma = -1$ energy branch and, as is well known, it leads to the Airy differential equation for the solutions close to the turning point [129]. In the case of the level crossing at $\phi = \pi$, the linearization involves both branches. It leads to the 2×2 system of equations of the Landau-Zener problem with imaginary time [114], mathematically equivalent to a Weber differential equation whose solutions are parabolic cylinder functions [130].

The result of these calculations, which are reproduced in detail in appendix 2.8, is a bound state equation for the energy which takes the form:

$$\cos \sigma = w e^{-\tau} \cos(2\pi n_g + \delta) + e^{-\rho} e^{-\tau} \cos(4\pi n_g) \quad (2.12)$$

On the left hand side, σ is the integral of k_- over the classically available region,

$$\sigma(E) = \int_{-\phi_c}^{\phi_c} \sqrt{\frac{E - \Gamma_A + E_A(\phi)}{4E_C}} d\phi. \quad (2.13)$$

On the right hand side, τ and ρ are WKB tunneling integrals, respectively under the smaller barrier of the - branch and the larger barrier of the + branch:

$$\tau(E) = \int_{\phi_c}^{2\pi - \phi_c} \sqrt{\frac{\Gamma_A - E - E_A(\phi)}{4E_C}} d\phi, \quad (2.14)$$

$$\rho(E) = \int_{-\pi}^{\pi} \sqrt{\frac{\Gamma_A - E + E_A(\phi)}{4E_C}} d\phi. \quad (2.15)$$

Furhermore, on the right hand side of Eq. (2.12), w represents the amplitude for the wave function to remain on the lower branch when evolving

through the avoided crossing. It is given by

$$w = \sqrt{\frac{2\pi}{\lambda} \frac{e^{-\lambda} \lambda^\lambda}{\Gamma(\lambda)}}, \quad (2.16)$$

with

$$\lambda = \frac{|r|^2}{4} \frac{\Gamma_A}{\Gamma} \sqrt{\frac{\Gamma_A}{E_C}} \quad (2.17)$$

the parameter controlling adiabaticity: w tends to one for $\lambda \gg 1$ (adiabatic limit), while $w \sim \sqrt{2\pi\lambda}$ for $\lambda \ll 1$. Note, in particular, that w vanishes when $r = 0$ (diabatic limit). Finally, in Eq. (2.12), $-\delta$ is the phase of the complex reflection coefficient r .

Before proceeding to solve the bound state equation, it is useful to discuss its structure. The first and second term on the right hand side of Eq. (2.12) originate from 2π and 4π phase slips respectively, as revealed by their different periodicity with respect to the induced charge n_g . The latter can be understood in terms of the Aharonov-Casher effect: in a 4π phase slip, the phase variable wraps around the circle twice, and so the wave function picks up a phase factor of $4\pi n_g$. The comparison of the two terms also tells us that 2π phase slips dominate 4π phase slips when $we^\rho \gg 1$, while in the opposite limit $we^\rho \ll 1$ the 4π -periodic component dominates. Finally, we note that the appearance of the phase shift δ is a consequence of the twisted boundary conditions (2.8).

Neglecting the occurrence of quantum phase slips means setting to zero the exponentially small tunneling amplitudes $e^{-\tau}$ and $e^{-\rho}$ on the right hand side of Eq. (2.12). In this case the left hand side yields a Bohr-Sommerfeld quantization condition for the energy levels E_n in the Josephson potential,

$$\sigma(E_n) = \pi \left(n + \frac{1}{2} \right), \quad (2.18)$$

with $n = 0, 1, 2, \dots$. The effect of quantum phase slips can then be introduced as a small correction δ_n to the eigenvalues E_n obtained via the Bohr-Sommerfeld condition. This correction is the charge dispersion of the n -th energy level due to quantum phase slips. Expanding the left hand

side of Eq. (2.12) as described in appendix 2.8 leads to the expression

$$\begin{aligned} \delta_n &= \frac{(-1)^{n+1}}{\sigma'_n} w e^{-\tau_n} \cos(2\pi n_g + \delta) \\ &+ \frac{(-1)^{n+1}}{\sigma'_n} e^{-\rho_n} e^{-\tau_n} \cos(4\pi n_g) \\ &- \frac{\tau'_n}{2(\sigma'_n)^2} w^2 e^{-2\tau_n} \cos(4\pi n_g + 2\delta). \end{aligned} \quad (2.19)$$

We adopted a shortened notation for the tunneling integrals evaluated at the eigenenergies, e.g. $\tau_n \equiv \tau(E_n)$.

Equation (2.19) is the central result of this chapter: it describes the oscillations of the energy levels of the S-R-S transmon circuit as a function of the induced charge, including the effects of 2π and 4π quantum phase slips on equal footing. The first term of Eq. (2.19) gives the contribution to the charge dispersion coming from 2π phase slips, which coincides with the one computed in Ref. [114, 116]. This term yields a charge dispersion with a period of $2e$ and it vanishes as $r \rightarrow 0$, since in this limit $w \rightarrow 0$. The second term gives the contribution coming from 4π phase slips, which is finite in the limit $r \rightarrow 0$. The last term is a 4π -periodic correction to the first term, of higher order in the tunneling integral τ_n . We retain it here since, as w increases, it becomes as large as the second term in the crossover between 2π - and 4π -dominated regimes, and eventually larger when $w \approx 1$.

Our next goal is to compare these analytical results with numerical results. To do so, we provide approximate expressions for the quantities appearing in Eq. (2.19) in terms of the model parameters. To begin with, in the limit $T\Gamma_A \gg E_C$ in which it is appropriate to approximate the potential as a parabola, the Bohr-Sommerfeld condition gives the harmonic spectrum

$$E_n = \sqrt{2T\Gamma_A E_C} \left(n + \frac{1}{2} \right) \equiv \omega_p \left(n + \frac{1}{2} \right). \quad (2.20)$$

We introduced the Josephson plasma frequency ω_p for later convenience. The anharmonic corrections to E_n are of order $\sqrt{E_C/T\Gamma_A}$ and will be neglected.

Evaluating the tunneling integrals at these energies we obtain

$$e^{-\tau_n} = \frac{\sqrt{2\pi}}{n!} \left(\frac{b^2 \omega_p}{4E_C} \right)^{n+\frac{1}{2}} e^{-a \omega_p / E_C} \quad (2.21)$$

$$e^{-\rho_n} = e^{-(c/\sqrt{T}) \omega_p / E_C + d\sqrt{T}(n+1/2)} \quad (2.22)$$

where a, b, c, d are positive numerical coefficients that depend weakly on T , and whose explicit expressions are given in appendix 2.9. Finally, we also find

$$\sigma'_n = \frac{\pi}{\omega_p}, \quad (2.23)$$

$$\tau'_n = \frac{1}{\omega_p} \log \frac{4E_C(n + \frac{1}{2})}{b^2 \omega_p}. \quad (2.24)$$

By simple replacement of Eqs. (2.21)-(2.24) into Eq. (2.19), it is possible to obtain explicit asymptotic expressions for the different contributions to the charge dispersion as a function of the model parameters.

2.5 Results

Armed with these expressions, we can compare the energy levels obtained from the WKB ansatz with those obtained from a numerical diagonalization of the Hamiltonian (2.1) in the charge basis. The comparison serves both as a verification of the results obtained analytically and as a way to illustrate the behavior of the quantum phase slips amplitude versus the model parameters. To do so, it is convenient to extract the $2e$ - and $1e$ -periodic components of the charge dispersion $\delta_n(n_g)$:

$$\delta_n(n_g) = \delta_n^{2e} \cos(2\pi n_g + \beta_n^{2e}) + \delta_n^{1e} \cos(4\pi n_g + \beta_n^{1e}) \quad (2.25)$$

This equation is just a re-writing of the right hand side of Eq. (2.19) as a Fourier series. In particular, δ_n^{2e} tracks the amplitude of the first term in Eq. (2.19), originating from 2π phase slips, while δ_n^{1e} tracks the amplitude of the second and third term in Eq. (2.19), originating from 4π phase slips; β_n^{2e} and β_n^{1e} are the corresponding total phase shifts.

In figure 2.4, we show the evolution of δ_n^{2e} and δ_n^{1e} for both the ground ($n = 0$) and first excited ($n = 1$) states, as the three model parameters $\Gamma, \delta\Gamma$ and ϵ_r are swept at fixed E_C . The parameter sweep is such that

the left end of the figure corresponds to the weak tunneling regime ($\Gamma = E_C$), finite asymmetry ($\delta\Gamma/E_C = 0.5$), and finite detuning from resonance ($\epsilon_r/E_C = 0.5$). On the other hand, the right end of the figure corresponds to the strong tunneling regime ($\Gamma/E_C = 15$) and the resonant condition $\delta\Gamma = \epsilon_r = 0$.

The first panel shows the exponential suppression of the charge dispersion as the tunneling rate Γ is increased at fixed $\delta\Gamma$ and ϵ_r . This behavior is familiar from conventional transmon model [26] and it originates from the increase in the Josephson potential barrier height due to the increase of Γ . The second panel shows that the trend continues as the asymmetry $\delta\Gamma$ is tuned to zero at fixed Γ and ϵ_r . This is because the effect of decreasing $\delta\Gamma$ at fixed detuning is to increase $T\Gamma_A$ and, thus, the Josephson potential barrier height. Up to now, both δ_n^{2e} and δ_n^{1e} exhibit a similar trend, because in these parameter ranges their magnitudes are both controlled by the exponent τ_n .

The third panel of figure 2.4 shows the effect of tuning the level to resonance. The 2π phase slip amplitude δ_n^{2e} drops to zero linearly towards resonance, because as the reflection coefficient r approaches zero, non-adiabatic effects related to the narrowly avoided crossing at $\phi = \pi$ start to kick-in, and the Landau-Zener parameter w vanishes. On the other hand, the 4π phase slip amplitude δ_n^{1e} saturates to a finite value determined by the exponent ρ_n , which is not sensitive to the closing of the avoided crossing. Eventually, the 4π -periodic component overcomes the 2π -periodic component of the charge dispersion at a value of ϵ_r determined by the condition $w \approx e^{-\rho_n}$, which depends slightly on n , as the figure shows. This crossover is well captured by the WKB solutions. In fact, figure 2.4 shows that the agreement between the asymptotic WKB results and the numerically determined eigenvalues is reasonable even at values of Γ/E_C not much larger than one, especially for the ground state $n = 0$.

The right panel of figure 2.4 also shows that if $\Gamma \gg E_C$, the crossover to the 4π -dominated regime only happens very close to resonance and at charge dispersion levels so small to be practically unobservable. For instance, in figure 2.4, δ_n^{1e} saturates at a value of order $10^{-6} E_C$ for $n = 1$, reached when $\epsilon_r \approx 10^{-5} E_C$. However, the effect becomes more striking, and experimentally detectable, when the ratio Γ/E_C is reduced.

To highlight this, in figure 2.5 we show the scaling of the charge dispersion when the tunneling strength Γ is varied while maintaining

the resonant condition. Here we focus on the average energy difference $\bar{\omega}_{01} = \int_0^1 dn_g (E_1 - E_0)$, where E_1 and E_0 are the numerically determined eigenvalues of the Hamiltonian, and on the peak-to-peak amplitude $\delta\omega_{01}$ of its charge dispersion $\delta_1 - \delta_0$. These are the quantities that can be more easily measured in a typical microwave spectroscopy experiment such as those in Refs. [16, 17], which we have in mind as a feasible way to test our predictions. We note that, in principle, the charge dispersion of energy levels is also accessible in the I-V characteristic of the junction [131–133].

Furthermore, we compare the behavior predicted by the resonant level model with that of a conventional transmon device described by the Hamiltonian

$$H = 4E_C(i\partial_\phi + n_g)^2 - E_J \cos \phi \quad (2.26)$$

with periodic boundary conditions on a 2π interval. In the resonant level model, $\bar{\omega}_{01}$ and $\delta\omega_{01}$ were both computed numerically for increasing Γ/E_C at fixed $\delta\Gamma = 0$ and $\epsilon_r = 0$. For the transmon model, the same quantities were instead computed increasing E_J/E_C , and they reproduce the well-known curve for the charge dispersion of a transmon [26]. Via the parametric plot of the observable quantities $\bar{\omega}_{01}$ and $\delta\omega_{01}$, computable for both models despite the different set of parameters, a direct comparison can be made.

The comparison shows that, while the charge dispersion decays exponentially in both models, the effect is much stronger in the presence of a resonant level. This is because we are essentially comparing the tunneling amplitude under a $-\Gamma \cos(\phi/2)$ barrier and that under a $-E_J \cos \phi$ barrier: the former corresponds to a higher potential and a longer tunneling path, and is therefore exponentially smaller than the latter. Thus, as Refs. [16, 17] pointed out, resonant tunneling provides a way to reach a target charge dispersion while keeping the superconducting island closer to the Cooper-pair box limit of weak tunneling ($\Gamma \gtrsim E_C$ rather than $\Gamma \gg E_C$). For instance, in order to achieve $\delta_{01}/E_C \approx 10^{-3}$ it is necessary to reach a ratio $\omega_{01}/E_C \approx 15$ (that is, $E_J/E_C \approx 32$) in the model of Eq. (2.26), but it may be enough to reach the ratio $\omega_{01}/E_C \approx 3$ (that is, $\Gamma/E_C \approx 5$) using the resonant level model of Eq. (2.1).

This fact is convenient for qubit design, since it mitigates a practical trade-off at play in the transmon: reducing the charge dispersion increases the dephasing time, but at the cost of an increase of device footprint and capacitive losses, due to the need for a large capacitor. However, the suppression of 2π phase slips, which is at the basis of the advantageous

scaling of figure 2.5, requires fine-tuning the junction to a resonance. Thus, the effect will be very sensitive with respect to noise, especially to noise in the detuning parameter ϵ_r , which would originate from charge noise in the gates required to tune the resonant level.

To illustrate this important point, in figure 2.6 we show the evolution of $\omega_{01}(n_g)$ as ϵ_r is varied from positive to negative through zero, in the case of a rather weak tunneling $\Gamma/E_C = 5$. In the top panel, we see how the charge dispersion evolves from a conventional $2e$ -periodic oscillation with a maximum at $n_g = 0$ ($\epsilon_r > 0$), to a $1e$ -periodic curve at resonance ($\epsilon_r = 0$, black dashed line), to a shifted $2e$ -periodic curve with a maximum at $n_g = 1/2$ ($\epsilon_r < 0$). The plot illustrates how the suppression of the charge dispersion occurs because the charge dispersion changes sign as ϵ_r passes through zero, signaling the ground state occupation of the resonant level by a Cooper pair when $\epsilon_r < 0$. Neglecting 4π phase slips, the dashed line at $\epsilon_r = 0$ would be flat.

In the bottom panel of figure 2.6 we show the $2e$ - and $1e$ -periodic amplitudes $\delta_{01}^{1e} \equiv \delta_1^{1e} - \delta_0^{1e}$ and $\delta_{01}^{2e} \equiv \delta_1^{2e} - \delta_0^{2e}$, extracted from the curves in the top panel (computed in a wider ϵ_r range). The 4π phase slip amplitude stays approximately constant, while the 2π phase slip amplitude goes through a dip at resonance, with its minimum value at $\epsilon_r = 0$ determined by the presence of a small, residual asymmetry ($\delta\Gamma \approx 10^{-4}E_C$ in figure 2.6) While the region dominated by 4π phase slips has widened with respect to the right panel of figure 2.4 due to the smaller ratio Γ/E_C , it still occurs in a relatively narrow interval, $|\epsilon_r|/E_C \lesssim 0.01$. The dephasing time of the plasma oscillation would be dictated by 4π phase slips only if time-dependent noise in the detuning parameter ϵ_r were to be contained in this interval. Nevertheless, the plot also shows that in this parameter regime it would be feasible, with reasonable experimental resolution, to detect the occurrence of 4π phase slips at resonance via a spectroscopic measurement of the $\omega_{01}(n_g)$ curve. Indeed, the residual charge dispersion at resonance is $\approx 2 \times 10^{-3}E_C$ in figure 2.6, and thus it would fall in the MHz frequency range for realistic values of $E_C/h \sim 1$ GHz.

2.6 Conclusions

We have studied in detail the quantum phase slips occurring in a Josephson junction in the presence of a resonant level mediating the tunneling of Cooper pairs. It was known since Ref. [114] that 2π phase slips are

fully suppressed in the presence of a level crossing in the Andreev spectrum. Here, we have extended this result by computing the amplitude of 4π phase slips, which remain finite in the presence of a level crossing and provide the mechanism by which the charge dispersion of the superconducting island remains finite, albeit possibly very small. Our central result is Eq. (2.19): obtained within the WKB approximation, it provides asymptotic expressions for the energy levels of a Cooper-pair box in the transmon limit, including the effect of both 2π and 4π quantum phase slips, and yielding results in good agreement with numerical simulations². To conclude this chapter we discuss several implications of our results.

2.6.1 Experimental observability of 4π phase slips in transmon circuits

The suppression of 2π phase slips occurs in a fairly narrow parameter range near resonance ($\epsilon_r = 0$) and symmetric barriers ($\delta\Gamma = 0$). Within this parameter range, a crossover to a regime dominated by 4π phase slips occurs (see figure 2.6). The width of the crossover region around resonance, as well as the residual level of charge dispersion at resonance given by 4π phase slips, both increase with decreasing Γ/E_C .

Although the suppression of 2π phase slips at resonance has been observed in Refs. [16, 17], coherent 4π quantum phase slips were not observed. We attribute this fact to the large ratio Γ/E_C of those measurements. Our calculations predict that coherent 4π quantum phase slips should be observable with the same technology of existing experiments, only in devices with larger charging energy. For instance, let us consider a situation in which $E_C/h = 1$ GHz, $\epsilon_r = \delta\Gamma = 0$ and $\Gamma/h = 3$ GHz. Then, our model predicts that $\omega_{01} \approx 2.16$ GHz while $\delta\omega_{01} \approx 33$ MHz, easily in the range of detectable frequency shifts.

The direct comparison with a transmon qubit based on a conventional tunnel junction with Josephson energy $-E_J \cos \phi$ shows that the resonant level provides a much lower charge dispersion at a fixed ratio of the qubit frequency to the charging energy (see figure 2.5). We have discussed critically the possible implications of this fact for qubit design, emphasizing that the circuit is likely to remain sensitive to charge noise modulating the energy of the resonant level.

²The code and notebooks used to generate the numerical results in this work are available on Zenodo [134]

2.6.2 Connection to novel qubit designs

Our results are relevant for the recently introduced bi-fluxon qubit [7], which uses a superconducting island tuned to the charge degeneracy point as a way to implement resonant Cooper pair tunneling with a 4π -periodic effective Josephson energy. Indeed, the model of Eqs. (2.1) and (2.2) also applies to such a case: the two degenerate charge states of the island, with charge differing by $2e$, map to the resonant level in our model being empty or occupied. In this mapping, the parameters ϵ_r and $\delta\Gamma$ indicate the detuning from the charge degeneracy point of the island and the asymmetry between two tunnel junctions. For noise protection, the bi-fluxon qubit relies on the suppression of 2π quantum phase slips and ideally operates in a regime where only 4π quantum phase slips are present. Our detailed results on the competition of 2π and 4π quantum phase slips, especially at finite detuning or junction asymmetry, are therefore relevant for its design.

A difference between the S-R-S transmon model studied in this chapter and the bi-fluxon is that the circuit of the latter features an inductive shunt, similar to the fluxonium circuit [28]. In the presence of an inductive loop, quantum phase slips couple coherently persistent current states characterized by a differing number of fluxons trapped in the loop [27]. By tuning the applied flux, it is therefore possible to measure separately the amplitude for 2π and 4π phase slips, making such a device ideal to observe the crossover between 2π and 4π -dominated regimes. In fact, a fluxonium circuit with a weak link of the S-R-S type could be a competitive version of the bi-fluxon qubit. We leave the analysis of this topic to future work.

2.6.3 Connection to Majorana zero modes

Our calculations also have a close connection with models of superconducting islands with Majorana zero modes (MZMs) [135, 136]. It is known that the 4π Josephson effect occurring in a junction between topological superconductors (due to the presence of a pair of coupled MZMs) [119, 120] suppresses the occurrence of 2π phase slips, leaving only the occurrence of 4π phase slips [137–139]. Even the boundary condition of Eq. (2.8) has a precise counterpart in models with topological superconducting islands, where it arises due to a fermion parity constraint on the BCS wave function [135, 140]. In fact, the model of Eq. (2.1), together with the boundary conditions, can be mapped exactly to a model of four MZMs,

two per superconducting side, coupled across a weak link. Such a model of four coupled MZMs could arise, for instance, because of finite-size effects in a topological nanowire [141].

2.6.4 Generality of our results

Finally, let us discuss the generality of our results. The regime with dominating 4π phase slips should persist even outside of the strict domain of validity of the model in Eq. (2.2), because it is a consequence of the presence of a level crossing in the Andreev spectrum rather than of the precise form taken by the Josephson potential energy. For instance, the assumption $\Gamma \ll \Delta$ could be relaxed; doing so would modify the phase dependence of the Andreev spectrum and the precise values of the WKB integrals, but not the essential feature that 2π phase slips are suppressed at resonance.

Similar conclusions can be drawn about multi-channel extensions of the single-channel model of Eq. (2.2). If the additional channels are not resonant, they simply provide a 2π -periodic contribution to the Josephson energy (a similar contribution is also provided by the above-gap, continuous part of the spectrum). This contribution will increase the height of the Josephson potential barrier, and thus lower all the quantum phase slips amplitudes, but it will not affect the resonant suppression of 2π phase slips illustrated in figure 2.6. The resonant suppression is controlled by the parameter w of Eq. (2.16), and thus by the most transparent channel only. Qualitative deviations from our central result, Eq. (2.19) are therefore only expected in the fine-tuned case where more than one transport channel achieves near-perfect transparency ($|r|^2 \ll \sqrt{E_C/\Gamma_A}$).

Our results also remain valid in the presence of a finite interaction energy U for the double-occupancy of the resonant level, a term neglected in this chapter. This is true at least as long as $U \ll \Gamma$, since such a weak interaction would only renormalize the couplings in the effective Hamiltonian of Eq. (2.1) [18]. For larger U , a transition to an odd-parity doublet ground state occurs close to resonance, diminishing the relevance of Eq. (2.1), which applies to an even-parity singlet ground state. The study of quantum phase slips when the junction is in the doublet ground state is an interesting problem left to future research.

2.7 Appendix: Derivation of the low-energy Hamiltonian

In this appendix, we derive Eq. (2.1) starting from the model of a level tunnel-coupled to two superconductors. Similar derivations have appeared in the literature before, e.g. in Refs. [18, 19]. Here we propose a simple derivation that motivates and clarifies the use of the boundary conditions of Eq. (2.8). The starting point is the following Hamiltonian:

$$H = H_{\text{sc}} + H_{\text{dot}} + H_{\text{tunn}} + H_{\text{c}}. \quad (2.27)$$

The first term H_{sc} is the Hamiltonian of the two superconductors,

$$H_{\text{sc}} = \sum_{\alpha n \sigma} \xi_n c_{\alpha n \sigma}^\dagger c_{\alpha n \sigma} - \Delta \sum_{\alpha n} \left(e^{-i\phi_\alpha} c_{\alpha \uparrow}^\dagger c_{\alpha \downarrow}^\dagger + \text{h.c.} \right) \quad (2.28)$$

where $\alpha = 1, 2$ denotes the two leads, n enumerates their spin-degenerate single-particle states with energy ξ_n , $\sigma = \uparrow, \downarrow$ is the spin quantum number, Δ is the pairing gap, and ϕ_α is the superconducting phase in the two leads.

The second term is the Hamiltonian of the resonant level:

$$H_{\text{dot}} = \epsilon_r \sum_{\sigma} \left(d_{\sigma}^\dagger d_{\sigma} - \frac{1}{2} \right), \quad (2.29)$$

where the operator $d_{\sigma}^\dagger, d_{\sigma}$ create and annihilate an electron with spin σ on the resonant level. For simplicity, we omit an Anderson U . The limitations of this choice are discussed in the main text and are not crucial for what follows. The third term is the tunneling Hamiltonian between the leads and the energy level in the dot:

$$H_{\text{tunn}} = \sum_{\alpha n \sigma} t_{\alpha} \left(d_{\sigma}^\dagger c_{\alpha n \sigma} + \text{h.c.} \right). \quad (2.30)$$

Again for simplicity, we only consider spin-conserving tunneling. In the presence of both time-reversal symmetry and spin-rotation symmetry, the couplings t_{α} can be chosen to be real.

Finally, the last term is the charging energy between the two leads:

$$H_{\text{c}} = 4E_C(N - n_g)^2 \quad (2.31)$$

where $E_C = e^2/2C$ is the charging energy and n_g the dimensionless charge induced by gates, and N is the charge transferred between the two leads.

Both N and n_g are expressed in units of the Cooper pair charge $2e$. Explicit expressions for E_C and n_g in terms of the capacitances and gate voltages of a capacitive network of two islands are given in Ref. [13]. In writing the charging energy, we have neglected the capacitance between the superconductors and the quantum dot hosting the energy levels, as well as the capacitance between the superconductors and any gates which may control the quantum dot.

At the mean-field level description of superconductivity, N is an operator which includes separate contributions from both the paired and unpaired electrons:

$$N = \frac{1}{2}(N_1 - N_2) + \frac{1}{4} \sum_{n\sigma} \left(c_{1n\sigma}^\dagger c_{1n\sigma} - c_{2n\sigma}^\dagger c_{2n\sigma} \right). \quad (2.32)$$

Here, we denoted with N_1, N_2 the number of Cooper pairs in each superconductor. They are operators with integer spectrum obeying the following commutation rules:

$$[N_\alpha, e^{\pm i\phi_\beta}] = \pm \delta_{\alpha\beta} e^{\pm i\phi_\beta}. \quad (2.33)$$

We stress the fact that the operator N keeps count of the charge *transferred* between the superconductors in units of $2e$. Thus, a transfer of a Cooper pair between superconductors ($N_1 \rightarrow N_1 \pm 1, N_2 \rightarrow N_2 \mp 1$) changes N by one unit (e.g. $N \rightarrow N \pm 1$). On the other hand, a transfer of a single electron changes N by $\pm(1/2)$. Simply, yet amusingly, the transfer of a Cooper pair from either superconductor to the quantum dot also changes N by $\pm(1/2)$.

It is convenient to use a gauge transformation that removes the operators $e^{i\phi_\alpha}$ from H_{sc} and which also simplifies the form of the charging energy [142]. The gauge transformation is $H \rightarrow U H U^\dagger$, with:

$$U = U_1 U_2, \quad U_\alpha = \exp \left(\frac{i\phi_\alpha}{2} \sum_{n\sigma} c_{\alpha n\sigma}^\dagger c_{\alpha n\sigma} \right) \quad (2.34)$$

In this new gauge, we have the following changes:

$$\begin{aligned} H_{sc} &\rightarrow \sum_{\alpha n\sigma} \xi_n c_{\alpha n\sigma}^\dagger c_{\alpha n\sigma} - \Delta \sum_{\alpha n} \left(c_{\alpha\uparrow}^\dagger c_{\alpha\downarrow}^\dagger + \text{h.c.} \right), \\ H_c &\rightarrow 4E_C (N - n_g)^2, \\ H_{\text{tunn}} &\rightarrow \sum_{\alpha n\sigma} t_\alpha \left(e^{-i\phi_\alpha/2} d_\sigma^\dagger c_{\alpha n\sigma} + \text{h.c.} \right), \end{aligned} \quad (2.35)$$

and $H_{\text{dot}} \rightarrow H_{\text{dot}}$. Note how the tunneling terms now contain operators $e^{\pm i\phi_\alpha/2}$, which shift N_α by one half.

The next step is to diagonalize H_{sc} and rewrite the tunneling Hamiltonian in terms of Bogoliubov quasiparticle operators:

$$c_{\alpha n \uparrow} = u_{\alpha n} \Gamma_{\alpha n \uparrow} + v_{\alpha n} \Gamma_{\alpha n \downarrow}^\dagger \quad (2.36)$$

$$c_{\alpha n \downarrow} = u_{\alpha n} \Gamma_{\alpha n \downarrow} - v_{\alpha n} \Gamma_{\alpha n \uparrow}^\dagger \quad (2.37)$$

with $u_n^2 = \frac{1}{2}(1 + \xi_n/\epsilon_n)$, $v_n^2 = \frac{1}{2}(1 - \xi_n/\epsilon_n)$, and $\epsilon_n^2 = \xi_n^2 + \Delta^2$. After the Bogoliubov rotation, the Hamiltonian changes as follows:

$$\begin{aligned} H_{\text{sc}} &\rightarrow \sum_{\alpha n \sigma} \epsilon_n \Gamma_{\alpha n \sigma}^\dagger \Gamma_{\alpha n \sigma} \\ H_{\text{tunn}} &\rightarrow \sum_{\alpha n \sigma} t_\alpha \left[e^{-i\phi_\alpha/2} d_\sigma^\dagger \left(u_n \Gamma_{\alpha n \sigma} + \sigma v_n \Gamma_{\alpha n \bar{\sigma}}^\dagger \right) \right. \\ &\quad \left. + e^{i\phi_\alpha/2} \left(u_n \Gamma_{\alpha n \sigma}^\dagger + \sigma v_n \Gamma_{\alpha n \bar{\sigma}} \right) d_\sigma \right], \end{aligned}$$

with the other terms left untouched.

At this point, assuming that Δ is the largest energy scale in the problem, we would like to integrate out the quasi-particles in the leads and derive an effective Hamiltonian describing the low-energy coupled dynamics of the condensate and of the quantum dot. Assuming that the total number of electrons in the system is even, a generic wave function in the even-parity low-energy space can be written as

$$|\Psi\rangle = \sum_{n \in \mathbb{Z}} \Psi_0(n) |n\rangle |0\rangle + \sum_{n \in \mathbb{Z} + \frac{1}{2}} \Psi_2(n) |n\rangle |2\rangle, \quad (2.38)$$

where $|n\rangle$ are states with a given number of Cooper pairs transferred: $N|n\rangle = n|n\rangle$, $|0\rangle$ denotes the empty dot state, and $|2\rangle = d_\uparrow^\dagger d_\downarrow^\dagger |0\rangle$ denotes the state in which the dot is occupied by a pair.

Using old-fashioned perturbation theory to the second order in the tunneling term, and integrating out states with unpaired quasiparticles, we obtain the following eigenvalue problem, written in terms of the wave function amplitudes $\Psi_0(n)$ and $\Psi_2(n)$:

$$\left[E - 4E_C(n - n_g)^2 + \epsilon_r \right] \Psi_0(n) = -\Gamma_1 \Psi_2(n - \frac{1}{2}) - \Gamma_2 \Psi_2(n + \frac{1}{2}), \quad (2.39)$$

$$\left[E - 4E_C(n - n_g)^2 - \epsilon_r \right] \Psi_2(n) = -\Gamma_2 \Psi_0(n - \frac{1}{2}) - \Gamma_1 \Psi_0(n + \frac{1}{2}), \quad (2.40)$$

where $\Gamma_\alpha = \sum_n (2t_\alpha^2 v_n u_n) / \epsilon_n = \pi t_\alpha^2 / \delta_\alpha$, with δ_α the level spacing in the superconductor. A Fourier series,

$$\Psi_0(\phi) = \sum_{n \in \mathbb{Z}} e^{i\phi n} \Psi_0(n), \quad (2.41)$$

$$\Psi_2(\phi) = \sum_{n \in \mathbb{Z} + \frac{1}{2}} e^{i\phi n} \Psi_2(n), \quad (2.42)$$

yields the effective Hamiltonian of the main text, acting on the spinor wave function

$$\Psi(\phi) = \begin{bmatrix} \Psi_0(\phi) \\ \Psi_2(\phi) \end{bmatrix} \quad (2.43)$$

The boundary condition of Eq. (2.8) follows from the fact that $\Psi_0(\phi + 2\pi) = \Psi_0(\phi)$ while $\Psi_2(\phi + 2\pi) = -\Psi_2(\phi)$.

2.8 Appendix: WKB solution

In this appendix we derive the bound state equation (2.12) of the main text, applying the WKB approach to the Schrödinger equation $H\Psi = (-\Gamma_A + E)\Psi$ for the Hamiltonian in Eq. (2.1).

We find it convenient to rotate the Hamiltonian such that the $\cos(\phi/2)$ term in the potential appears on the diagonal: the basis of the eigenstates of $V(\phi)$ at $\epsilon_r = 0$. The transformation consists of a rotation of Ψ by $-\pi/2$ around the y -axis. Simultaneously, as already mentioned in the main text, we also multiply the wave function by a phase that gets rid of n_g in the Hamiltonian, so that the transformation is

$$\Psi \rightarrow e^{i\phi n_g} e^{i(\pi/4)\tau_y} \Psi \quad (2.44)$$

$$H \rightarrow e^{i\phi n_g} e^{i(\pi/4)\tau_y} H e^{-i\phi n_g} e^{-i(\pi/4)\tau_y}. \quad (2.45)$$

Since

$$e^{i(\pi/4)\tau_y} = \frac{1}{\sqrt{2}} \begin{bmatrix} 1 & 1 \\ -1 & 1 \end{bmatrix}, \quad (2.46)$$

the transformation amounts to sending

$$H \rightarrow -4E_C \partial_\phi^2 + \epsilon_r \tau_x - \Gamma \cos(\phi/2) \tau_z - \delta \Gamma \sin(\phi/2) \tau_y. \quad (2.47)$$

In this new basis, the boundary condition is also different:

$$\Psi(\phi + 2\pi) = -\tau_x e^{i2\pi n_g} \Psi(\phi) \quad (2.48)$$

In the calculation that follows we will make use of the adiabatic eigenstates of the potential $V(\phi)$ after the transformation, which in matrix form is given by

$$V(\phi) = \begin{bmatrix} -\Gamma \cos(\phi/2) & \epsilon_r + i\delta\Gamma \sin(\phi/2) \\ \epsilon_r - i\delta\Gamma \sin(\phi/2) & \Gamma \cos(\phi/2) \end{bmatrix} \quad (2.49)$$

The two eigenvectors $V(\phi)\chi_\pm = \pm E_A(\phi)\chi_\pm$ are:

$$\chi_+ = \mathcal{N}^{-1/2}(\phi) \begin{bmatrix} E_A - \Gamma \cos(\phi/2) \\ \epsilon_r - i\delta\Gamma \sin(\phi/2) \end{bmatrix} \quad (2.50a)$$

$$\chi_- = \mathcal{N}^{-1/2}(\phi) \begin{bmatrix} -\epsilon_r - i\delta\Gamma \sin(\phi/2) \\ E_A - \Gamma \cos(\phi/2) \end{bmatrix} \quad (2.50b)$$

with a normalization factor given by

$$\mathcal{N}(\phi) = 2E_A(E_A - \Gamma \cos(\phi/2)). \quad (2.51)$$

For later use we note the following property of these spinors:

$$\chi_+(2\pi + \phi) = e^{i\delta(\phi)} \tau_x \chi_+(\phi), \quad (2.52)$$

$$\chi_-(2\pi + \phi) = -e^{-i\delta(\phi)} \tau_x \chi_-(\phi). \quad (2.53)$$

where $\delta(\phi)$ is the phase of $\epsilon_r + i\delta\Gamma \sin(\phi/2)$.

To solve the Schrödinger equation, we split the interval $[-\pi, \pi]$ into four regions as follows:

- Region I: $\phi \in (-\pi, -\phi_c)$, where ϕ_c is the classical turning point such that $\Gamma_A - E_A(\phi_c) = E$.
- Region II: $\phi \in (-\phi_c, \phi_c)$.

- Region III: $\phi \in (\phi_c, \pi)$.
- Region IV: $\phi \in (\pi, 2\pi - \phi_c)$.

Within each region we can write the solution using the WKB ansatz, with either oscillatory or decaying/growing solutions. In detail:

$$\Psi_I = \frac{A_1 \chi_-}{\sqrt{\kappa_1}} e^{-\int_{-\pi}^{\phi} \kappa_1 d\phi'} + \frac{A_2 \chi_-}{\sqrt{\kappa_1}} e^{+\int_{-\pi}^{\phi} \kappa_1 d\phi'} + \quad (2.54)$$

$$+ \frac{A_3 \chi_+}{\sqrt{\kappa_2}} e^{-\int_{-\pi}^{\phi} \kappa_2 d\phi'} + \frac{A_4 \chi_+}{\sqrt{\kappa_2}} e^{+\int_{-\pi}^{\phi} \kappa_2 d\phi'}, \quad (2.55)$$

$$\Psi_{II} = \frac{B_1 \chi_-}{\sqrt{k_1}} \cos\left(\frac{\pi}{4} + \int_{-\phi_c}^{\phi} k_1 d\phi'\right) + \frac{2B_2 \chi_-}{\sqrt{k_1}} \sin\left(\frac{\pi}{4} + \int_{-\phi_c}^{\phi} k_1 d\phi'\right) + \quad (2.56)$$

$$+ \frac{B_3 \chi_+}{\sqrt{\kappa_2}} e^{-\int_{-\phi_c}^{\phi} \kappa_2 d\phi'} + \frac{B_4 \chi_+}{\sqrt{\kappa_2}} e^{+\int_{-\phi_c}^{\phi} \kappa_2 d\phi'}, \quad (2.57)$$

$$\Psi_{III} = \frac{C_1 \chi_-}{\sqrt{\kappa_1}} e^{-\int_{\phi_c}^{\phi} \kappa_1 d\phi'} + \frac{C_2 \chi_-}{\sqrt{\kappa_1}} e^{+\int_{\phi_c}^{\phi} \kappa_1 d\phi'} + \quad (2.58)$$

$$+ \frac{C_3 \chi_+}{\sqrt{\kappa_2}} e^{-\int_{\phi_c}^{\phi} \kappa_2 d\phi'} + \frac{C_4 \chi_+}{\sqrt{\kappa_2}} e^{+\int_{\phi_c}^{\phi} \kappa_2 d\phi'}, \quad (2.59)$$

$$\Psi_{IV} = \frac{D_1 \chi_-}{\sqrt{\kappa_1}} e^{-\int_{\pi}^{\phi} \kappa_1 d\phi'} + \frac{D_2 \chi_-}{\sqrt{\kappa_1}} e^{+\int_{\pi}^{\phi} \kappa_1 d\phi'} + \quad (2.60)$$

$$+ \frac{D_3 \chi_+}{\sqrt{\kappa_2}} e^{-\int_{\pi}^{\phi} \kappa_2 d\phi'} + \frac{D_4 \chi_+}{\sqrt{\kappa_2}} e^{+\int_{\pi}^{\phi} \kappa_2 d\phi'}. \quad (2.61)$$

For brevity, we have introduced the following wave vectors (note that the notation differs slightly with that of Eq. (2.10) in the main text):

$$k_1 = \sqrt{\frac{E - (\Gamma_A - E_A)}{4E_C}}, \quad (2.62)$$

$$\kappa_1 = \sqrt{\frac{(\Gamma_A - E_A) - E}{4E_C}}, \quad (2.63)$$

$$\kappa_2 = \sqrt{\frac{(\Gamma_A + E_A) - E}{4E_C}}. \quad (2.64)$$

The sixteen complex coefficients A_1, \dots, D_4 must be determined via appropriate matching conditions at the boundaries between the different regions. The matching condition between regions IV and I will be determined via the boundary condition (2.48). The boundaries between regions I-II, II-III

and III-IV are meant to be fuzzy, and one must make use of appropriate connection formulas for the WKB solutions by obtaining approximate solutions that are valid across the boundaries. This is what we do next.

To connect solutions at the boundary between region I and II, we can use the standard WKB connection formulas that originate from linearizing the potential around the classical turning point, and then solving the Airy equations. One obtains:

$$\begin{pmatrix} A_1 \\ A_2 \\ A_3 \\ A_4 \end{pmatrix} = \begin{pmatrix} e^{+\tau_1} & 0 & 0 & 0 \\ 0 & e^{-\tau_1} & 0 & 0 \\ 0 & 0 & e^{+\tau_2} & 0 \\ 0 & 0 & 0 & e^{-\tau_2} \end{pmatrix} \begin{pmatrix} B_1 \\ B_2 \\ B_3 \\ B_4 \end{pmatrix} \quad (2.65)$$

with $\tau_1 = \int_{\phi_c}^{\pi} \kappa_1 d\phi'$ and $\tau_2 = \int_{\phi_c}^{\pi} \kappa_2 d\phi'$.

For the boundary between region II and III we can also use the standard WKB connection formulas based on the Airy equation, except that we must first take some care to rewrite the wave function in region II so that it is expressed in terms of integrals that have the boundary point ϕ_c as the upper end of the integration domain.

After some trigonometric manipulations one obtains the following connection matrix:

$$\begin{pmatrix} B_1 \\ B_2 \\ B_3 \\ B_4 \end{pmatrix} = \begin{pmatrix} 2 \cos \sigma & -\sin \sigma & 0 & 0 \\ \sin \sigma & \frac{1}{2} \cos \sigma & 0 & 0 \\ 0 & 0 & e^{+\rho_1} & 0 \\ 0 & 0 & 0 & e^{-\rho_1} \end{pmatrix} \begin{pmatrix} C_1 \\ C_2 \\ C_3 \\ C_4 \end{pmatrix} \quad (2.66)$$

where $\rho_1 = \int_{-\phi_c}^{\phi_c} \kappa_2 d\phi'$.

Notice that so far the connections matrices (2.65) and (2.66) leave the two branches of the Andreev spectrum decoupled. This situation breaks down at the boundary between regions III and IV at $\phi = \pi$. This is the position where Andreev levels cross at perfect transparency, and where they couple in the presence of a small but finite back-scattering. When the level crossing is narrowly avoided, the adiabatic spinors (2.50) vary rapidly with phase and the WKB ansatz, which relies on a slow variation of the spinors with ϕ , breaks down. To proceed we must linearize the potential around $\phi = \pi$, giving the equation:

$$-4E_C \Psi'' + V_\pi \Psi + \Gamma_A \Psi = 0. \quad (2.67)$$

where

$$V_\pi = \epsilon_r \tau_x + \frac{1}{2} \Gamma (\phi - \pi) \tau_z - \delta \Gamma \tau_y \quad (2.68)$$

In Eq. (2.67) we set $E = 0$ since the level crossing is at energies much higher than the bottom of the Josephson potential: thus, the form of the solutions around $\phi \approx \pi$ will not be sensitive to the precise position of low-lying energy levels. Inspired by the fact that we need to connect asymptotically to the wave functions in region II, we try an ansatz of the form:

$$\Psi = \Psi_\pi e^{\sigma\kappa(\phi-\pi)} \quad (2.69)$$

with $\sigma = \pm 1$ and $\kappa = \sqrt{\Gamma_A/4E_C}$. Inserting the ansatz in Eq. (2.67) and neglecting the term $\propto \Psi''_\pi$ results in the following equation for Ψ_π :

$$-\sigma\omega_0\Psi'_\pi + V_\pi\Psi_\pi = 0 \quad (2.70)$$

with $\omega_0 = 8E_C\kappa$. Adopting the spinor notation $\Psi_\pi = (u, d)^T$, we obtain the following coupled linear differential equation for u and d :

$$-\sigma(\omega_0/\Gamma)u' + \tilde{r}d + \frac{1}{2}(\phi - \pi)u = 0 \quad (2.71)$$

$$-\sigma(\omega_0/\Gamma)d' + \tilde{r}^*u - \frac{1}{2}(\phi - \pi)d = 0 \quad (2.72)$$

where we introduced a complex reflection coefficient \tilde{r} :

$$\tilde{r} \equiv \frac{\epsilon_r + i\delta\Gamma}{\Gamma}. \quad (2.73)$$

Note that this reflection coefficients differs from the one introduced in the main text in Eq. (2.7) because of the presence of Γ instead of Γ_A in the denominator. The difference arises because the linearized problem is not sensitive to the bandwidth Γ_A of the potential, but only to its slope Γ at $\phi = \pi$. The phase of \tilde{r} is the same as that for r , and can be gauged away from the linearized equations, by setting $d \rightarrow de^{-i\delta/2}$ and $u \rightarrow ue^{i\delta/2}$. Furthermore, it is also convenient to shift and rescale the coordinate,

$$x = \sqrt{\frac{\Gamma}{\omega_0}}(\phi - \pi). \quad (2.74)$$

After these two steps we obtain

$$-\sigma u' + \sqrt{\lambda}d + \frac{1}{2}xu = 0 \quad (2.75)$$

$$-\sigma d' + \sqrt{\lambda}u - \frac{1}{2}xd = 0 \quad (2.76)$$

where the prime now refer to differentiation with respect to x and we have introduced

$$\lambda \equiv |\tilde{r}|^2 (\Gamma/\omega_0), \quad (2.77)$$

the same parameter introduced in Eq. (2.17) of the main text. Proceeding by substitution we obtain the two equations (one for each value of σ):

$$u'' + \left(-\lambda - \frac{\sigma}{2} - \frac{x^2}{4} \right) u = 0 \quad (2.78)$$

which must be considered separately and, combined, give the four independent solutions we are looking for. They are instances of the Weber differential equation and are solved in terms of parabolic cylinder functions $D_p(x)$, which satisfy the differential equation $D_p''(z) + (p + \frac{1}{2} - z^2/4)D_p(z) = 0$. In our case we are dealing with $p = -\lambda$ when $\sigma = -1$ and $p = -\lambda - 1$ when $\sigma = +1$.

Let us solve the two cases separately, beginning with $\sigma = -1$. The general solution for u is the linear combination $u(x) = c_1 D_{-\lambda}(x) + c_2 \sqrt{\lambda} D_{\lambda-1}(ix)$. The corresponding solution for $d(x)$ can be obtained using known recursion formulas for parabolic cylinder functions, which read:

$$D_p'(z) - pD_{p-1}(z) + \frac{1}{2}zD_p(z) = 0, \quad (2.79)$$

$$D_p'(z) + D_{p+1}(z) - \frac{1}{2}zD_p(z) = 0. \quad (2.80)$$

Using these formulas we obtain $d(x) = c_1 \sqrt{\lambda} D_{-\lambda-1}(x) + ic_2 D_{\lambda}(ix)$. Due to a symmetry of the problem, the solutions for $\sigma = +1$ can be obtained from these by sending $x \rightarrow -x$ and exchanging u and d , so that, overall, the general solution is

$$\begin{aligned} \Phi(x) = & c_1 e^{-\tilde{\kappa}x} \begin{bmatrix} D_{-\lambda}(x) \\ \sqrt{\lambda} D_{-\lambda-1}(x) \end{bmatrix} + c_2 e^{-\tilde{\kappa}x} \begin{bmatrix} \sqrt{\lambda} D_{\lambda-1}(ix) \\ iD_{\lambda}(ix) \end{bmatrix} \\ & + c_3 e^{+\tilde{\kappa}x} \begin{bmatrix} \sqrt{\lambda} D_{-\lambda-1}(-x) \\ D_{-\lambda}(-x) \end{bmatrix} + c_4 e^{+\tilde{\kappa}x} \begin{bmatrix} iD_{\lambda}(-ix) \\ \sqrt{\lambda} D_{\lambda-1}(-ix) \end{bmatrix}. \end{aligned} \quad (2.81)$$

Here, $\tilde{\kappa} = \kappa \sqrt{\omega_0/\Gamma}$. This solution captures the interval around $\phi = \pi$ where diabatic effects not captured by the WKB ansatz may occur. This region has a width $\sim \sqrt{\lambda}$. Thus, the solution has to be matched with Ψ_{III} from Eq. (2.58) for $x \ll -\sqrt{\lambda}$ and with Ψ_{IV} from Eq. (2.60) for $x \gg \sqrt{\lambda}$. For the matching purposes, it's useful to derive the asymptotic behaviour of these WKB solutions. In the case of Ψ_{III} , to do so we must first rewrite the WKB solution such that the integrals run up to the level crossing.

Thus, we rewrite Eq. (2.58) as

$$\begin{aligned} \Psi_{\text{III}} = & \frac{C_1 \chi_-}{\sqrt{\kappa_1}} e^{-\tau_1} e^{+\int_{\phi}^{\pi} \kappa_1 d\phi'} + \frac{C_2 \chi_-}{\sqrt{\kappa_1}} e^{+\tau_1} e^{-\int_{\phi}^{\pi} \kappa_1 d\phi'} \\ & + \frac{C_3 \chi_+}{\sqrt{\kappa_2}} e^{-\tau_2} e^{+\int_{\phi}^{\pi} \kappa_2 d\phi'} + \frac{C_4 \chi_+}{\sqrt{\kappa_2}} e^{+\tau_2} e^{-\int_{\phi}^{\pi} \kappa_2 d\phi'}. \end{aligned} \quad (2.82)$$

Let's introduce the distance R from the level crossing, $R = |x|$. When $R \gg \sqrt{\lambda}$, the asymptotes for the adiabatic spinors are:

$$\chi_-(-R) \sim \begin{bmatrix} -1 \\ \sqrt{\lambda}/R \end{bmatrix}, \quad (2.83)$$

$$\chi_+(-R) \sim \begin{bmatrix} \sqrt{\lambda}/R \\ 1 \end{bmatrix}, \quad (2.84)$$

$$\chi_-(R) \sim \begin{bmatrix} -\sqrt{\lambda}/R \\ 1 \end{bmatrix}, \quad (2.85)$$

$$\chi_+(R) \sim \begin{bmatrix} 1 \\ \sqrt{\lambda}/R \end{bmatrix}. \quad (2.86)$$

Note that $\chi_{\pm}(-R) = \pm \tau_x \chi_{\pm}(R)$. Taking into account the fact that, approaching the level crossing,

$$\kappa_{1,2} \approx \kappa \mp \frac{1}{2} \sqrt{4\lambda + R^2} \sqrt{\frac{\Gamma}{\omega_0}}, \quad (2.87)$$

we obtain the following expressions for the WKB integrals:

$$\begin{aligned} \int_{\phi}^{\pi} \kappa_1 d\phi' &= \tilde{\kappa} R - \frac{1}{4} R^2 - \frac{1}{2} \lambda - \lambda \log R + \lambda \log \sqrt{\lambda}, \\ \int_{\phi}^{\pi} \kappa_2 d\phi' &= \tilde{\kappa} R + \frac{1}{4} R^2 + \frac{1}{2} \lambda + \lambda \log R - \lambda \log \sqrt{\lambda}. \end{aligned} \quad (2.88)$$

Finally, when $\kappa \gg R \gg \sqrt{\lambda}$, one has that

$$\frac{1}{\sqrt{\kappa_{1,2}}} \approx \frac{1}{\sqrt{\kappa}} \quad (2.89)$$

The condition $\kappa \gg R \gg \sqrt{\lambda}$ is the necessary condition for the existence of a range of coordinates where asymptotes can be matched. In practice,

it requires the transition region around the level crossing at $\phi = \pi$ to be narrow enough to be far away from the classical turning point at $\phi = \phi_c$. Note that this condition is automatically satisfied since $\kappa \propto (\Gamma_A/E_C)^{1/2}$ while $\sqrt{\lambda} \sim (\Gamma_A/E_C)^{1/4}$.

With all that said, the expression approaching the level crossing from region III is:

$$\begin{aligned} \Psi_{\text{III}} \sim & \left(\frac{C_1}{\sqrt{\kappa}} e^{-\tau_1} e^{-\lambda/2} \lambda^{\lambda/2} \right) e^{\tilde{\kappa}R} e^{-R^2/4} R^{-\lambda} \chi_{-}(-R) \\ & + \left(\frac{C_2}{\sqrt{\kappa}} e^{+\tau_1} e^{+\lambda/2} \lambda^{-\lambda/2} \right) e^{-\tilde{\kappa}R} e^{R^2/4} R^{\lambda} \chi_{-}(-R) \\ & + \left(\frac{C_3}{\sqrt{\kappa}} e^{-\tau_2} e^{+\lambda/2} \lambda^{-\lambda/2} \right) e^{\tilde{\kappa}R} e^{R^2/4} R^{\lambda} \chi_{+}(-R) \\ & + \left(\frac{C_4}{\sqrt{\kappa}} e^{+\tau_2} e^{-\lambda/2} \lambda^{\lambda/2} \right) e^{-\tilde{\kappa}R} e^{-R^2/4} R^{-\lambda} \chi_{+}(-R) \end{aligned} \quad (2.90)$$

while the one for Ψ_{IV} , obtained from Eq. (2.54), is:

$$\begin{aligned} \Psi_{\text{IV}} \sim & \left(\frac{D_1}{\sqrt{\kappa}} e^{\lambda/2} \lambda^{-\lambda/2} \right) e^{-\tilde{\kappa}R} e^{R^2/4} R^{\lambda} \chi_{-}(R) \\ & + \left(\frac{D_2}{\sqrt{\kappa}} e^{-\lambda/2} \lambda^{\lambda/2} \right) e^{\tilde{\kappa}R} e^{-R^2/4} R^{-\lambda} \chi_{-}(R) \\ & + \left(\frac{D_3}{\sqrt{\kappa}} e^{-\lambda/2} \lambda^{\lambda/2} \right) e^{-\tilde{\kappa}R} e^{-R^2/4} R^{-\lambda} \chi_{+}(R) \\ & + \left(\frac{D_4}{\sqrt{\kappa}} e^{\lambda/2} \lambda^{-\lambda/2} \right) e^{\tilde{\kappa}R} e^{R^2/4} R^{\lambda} \chi_{+}(R) \end{aligned} \quad (2.91)$$

These two expressions must now be compared to and matched with the expansion of Eq. (2.81). The matching procedure will yield us a connection matrix between the wave function coefficients in regions III and IV. This connection matrix will take the form:

$$\begin{pmatrix} C_1 \\ C_2 \\ C_3 \\ C_4 \end{pmatrix} = \begin{pmatrix} e^{\tau_1} & 0 & 0 & 0 \\ 0 & e^{-\tau_1} & 0 & 0 \\ 0 & 0 & e^{\tau_2} & 0 \\ 0 & 0 & 0 & e^{-\tau_2} \end{pmatrix} M \begin{pmatrix} D_1 \\ D_2 \\ D_3 \\ D_4 \end{pmatrix} \quad (2.92)$$

where M is a 4×4 matrix whose elements must be determined via the matching procedure. We expect half of the matrix elements of M to be zero, because the exponentially decaying sector is decoupled from the

exponentially growing sector, as assumed by the ansatz (2.69). More in detail, the matrix M will have the following structure,

$$M = \begin{pmatrix} m_{11} & 0 & m_{12} & 0 \\ 0 & m'_{11} & 0 & m'_{12} \\ m_{21} & 0 & m_{22} & 0 \\ 0 & m'_{21} & 0 & m'_{22} \end{pmatrix} \quad (2.93)$$

with two interleaved 2×2 sub-blocks M^+ and M^- which separately connect exponentially decaying and growing solutions on either side of the level crossing:

$$M^- = \begin{pmatrix} m_{11} & m_{12} \\ m_{21} & m_{22} \end{pmatrix}, \quad (2.94)$$

$$M^+ = \begin{pmatrix} m'_{11} & m'_{12} \\ m'_{21} & m'_{22} \end{pmatrix}. \quad (2.95)$$

To simplify the derivation of M , we will make use of two useful identities that connect M^+ and M^- and thus allow to shorten the calculation.

The first identity is

$$\det M^+ = \det M^-. \quad (2.96)$$

It follows from the fact that, given two spinors $\Phi_1 = (u_1, d_1)^T$ and $\Phi_2 = (u_2, d_2)^T$ which are solutions of Eq. (2.75), one has

$$\frac{d}{dx} \det [\Phi_1 | \Phi_2] = 0, \quad (2.97)$$

where $[\Phi_1 | \Phi_2]$ is the matrix obtained joining the two spinors:

$$[\Phi_1 | \Phi_2] \equiv \begin{pmatrix} u_1 & u_2 \\ d_1 & d_2 \end{pmatrix}. \quad (2.98)$$

To verify this property one observes that:

$$\begin{aligned} \frac{d}{dx} \det [\Phi_1 | \Phi_2] &= \det [\Phi'_1 | \Phi_2] + \det [\Phi_1 | \Phi'_2] \\ &= \sigma \det [O\Phi_1 | \Phi_2] + \sigma \det [\Phi_1 | O\Phi_2], \end{aligned} \quad (2.99)$$

where $\sigma = \pm 1$ and $O = \frac{1}{2}x\tau_z + \sqrt{\lambda}\tau_x$. The last passage in the equation above follows directly from Eq. (2.75). To conclude the argument, one notices that

$$\det [O\Phi_1 | \Phi_2] = \det(O) \det [\Phi_1 | O^{-1}\Phi_2] \quad (2.100)$$

Furthermore, in our case, $O^{-1} = -\det^{-1}(O)O$. Thus,

$$\det[O\Phi_1|\Phi_2] = -\det[\Phi_1|O\Phi_2] \quad (2.101)$$

The conclusion is that

$$\det[\Phi_1|\Phi_2] = \text{constant}. \quad (2.102)$$

Let us apply it to the case in which Φ_1 and Φ_2 are the two exponentially decaying solutions ($\sigma = -1$) of Eq. (2.75) that enter Eq. (2.81) with coefficients c_1 and c_3 . We observe that the $\det[\Phi_1, \Phi_2]$ must remain constant also for the matched asymptotic expansions of Φ_1 and Φ_2 on either side of the crossing. A direct calculation gives

$$\det[\Phi_1|\Phi_2] = -\frac{D_1 D_3}{\tilde{\kappa}} \quad (2.103)$$

for $x \gg \sqrt{\lambda}$, and, using (2.92)

$$\det[\Phi_1|\Phi_2] = -\frac{D_1 D_3}{\tilde{\kappa}} \det M^- \quad (2.104)$$

for $x \ll -\sqrt{\lambda}$. It follows that $\det M^- = 1$. The reasoning is analogous for $\sigma = 1$, so $\det M^+ = 1$ too.

The second identity we will make use of is a pseudo-inverse identity which relates M^+ and M^- :

$$M^+ = \tau_z (M^-)^{-1} \tau_z \quad (2.105)$$

The idea behind this identity is that, as noticed earlier, there is a reflection symmetry around the level crossing: namely, if $[u(x), d(x)]^T$ is a solution of Eq. (2.75), then $[d(-x), u(-x)]^T$ is also a solution. This symmetry maps decaying solutions to growing ones and thus it suggests that there must be a relation between M^+ and M^- . Applying this symmetry argument to the asymptotic solutions and observing that their spinors obey $\chi_{\pm}(-x) = \pm \tau_x \chi_{\pm}(x)$, one arrives at the identity (2.105).

At this point we have to find the elements of M^- by looking at the asymptotic expansion of the parabolic cylinder functions [130], which can be applied term by term to (2.81) and then compared to the WKB asymptotes in Eq. (2.90) and (2.91). For instance, the last term in (2.81) has the following asymptotic behaviour (recall that $R = |x|$):

$$\begin{bmatrix} \sqrt{\lambda} D_{\lambda-1}(ix) \\ i D_{\lambda}(ix) \end{bmatrix} \sim i e^{-i\pi\lambda/2} e^{R^2/4} R^{\lambda} \chi_+(-R) \quad (2.106)$$

for $x \ll -\sqrt{\lambda}$ and

$$\begin{bmatrix} \sqrt{\lambda} D_{\lambda-1}(ix) \\ iD_{\lambda}(ix) \end{bmatrix} \sim ie^{i\pi\lambda/2} e^{R^2/4} R^{\lambda} \chi_{-}(R) \quad (2.107)$$

for $x \gg \sqrt{\lambda}$. Matching these asymptotes with Eq. (2.90) and (2.91) yields the matrix elements

$$m_{11} = 0, \quad (2.108)$$

$$m_{21} = e^{-i\pi\lambda}. \quad (2.109)$$

The third term in (2.81) has the asymptotic expansion

$$\begin{aligned} \begin{bmatrix} D_{-\lambda}(x) \\ \sqrt{\lambda} D_{-\lambda-1}(x) \end{bmatrix} &\sim -e^{i\pi\lambda} e^{-R^2/4} R^{-\lambda} \chi_{-}(-R) \\ &+ \frac{\sqrt{2\pi}}{\sqrt{\lambda}\Gamma(\lambda)} e^{R^2/4} R^{\lambda} \chi_{+}(-R) \end{aligned} \quad (2.110)$$

for $x \ll \sqrt{\lambda}$ and

$$\begin{bmatrix} D_{-\lambda}(x) \\ \sqrt{\lambda} D_{-\lambda-1}(x) \end{bmatrix} \sim e^{-R^2/4} R^{-\lambda} \chi_{+}(R) \quad (2.111)$$

for $x \gg \sqrt{\lambda}$. Again by comparison with (2.90) and (2.91), we derive

$$m_{22} = w \quad (2.112)$$

where w is the same as defined in the main text Eq. (2.16). The determinant identity for M^{-} then yields

$$m_{12} = -e^{i\pi\lambda} \quad (2.113)$$

This completes the matrix M^{-} . The matrix M^{+} can be derived using the pseudo-inverse identity, and both can be combined into the final form for the connection matrix M entering Eq. (2.92):

$$M = \begin{pmatrix} 0 & 0 & -e^{i\pi\lambda} & 0 \\ 0 & w & 0 & -e^{i\pi\lambda} \\ e^{-i\pi\lambda} & 0 & w & 0 \\ 0 & e^{-i\pi\lambda} & 0 & 0 \end{pmatrix} \quad (2.114)$$

The final step is to find the connection matrix at the boundary between region IV and I. In order to do so, we impose the twisted boundary conditions (2.48) evaluated at the point at $\phi = \pi + \epsilon$:

$$\Psi_{\text{IV}}(\pi + \epsilon) = -\tau_x e^{2\pi i n_g} \Psi_{\text{I}}(-\pi + \epsilon) \quad (2.115)$$

Using Eq. (2.52), this leads to two equations:

$$e^{-i\delta} (D_1 + D_2) = e^{2\pi i n_g} (A_3 + A_4) \quad (2.116)$$

$$e^{+i\delta} (D_1 + D_2) = -e^{2\pi i n_g} (D_3 + D_4) \quad (2.117)$$

where δ is the phase of $\epsilon_r - i\delta\Gamma$. We need two more equations, which we can get from taking the derivative of Eq. (2.48) at $\phi = \pi + \epsilon$:

$$\Psi'_{\text{IV}}(\pi + \epsilon) = -\tau_x e^{2\pi i n_g} \Psi'_{\text{I}}(-\pi + \epsilon), \quad (2.118)$$

to be computed neglecting the change in the slow components of the WKB wave functions. This leads to the following connection matrix:

$$\begin{pmatrix} D_1 \\ D_2 \\ D_3 \\ D_4 \end{pmatrix} = e^{2\pi i n_g} \begin{pmatrix} e^{i\delta} & 0 & 0 & 0 \\ 0 & e^{i\delta} & 0 & 0 \\ 0 & 0 & -e^{-i\delta} & 0 \\ 0 & 0 & 0 & -e^{-i\delta} \end{pmatrix} \begin{pmatrix} A_1 \\ A_2 \\ A_3 \\ A_4 \end{pmatrix} \quad (2.119)$$

Putting together Eqs. (2.65), (2.66), (2.114) and (2.119), we obtain a linear system of equation that must be satisfied by the coefficients in region I. After some matrix multiplication this linear system takes the form:

$$\vec{A} = e^{2\pi i n_g} M_1 M_2 M_3 \vec{A} \quad (2.120)$$

with $\vec{A} = (A_1, A_2, A_3, A_4)^T$ and

$$M_1 = \begin{pmatrix} 2e^\tau \cos \sigma & -\sin \sigma & 0 & 0 \\ \sin \sigma & \frac{1}{2}e^{-\tau} \cos \sigma & 0 & 0 \\ 0 & 0 & e^\rho & 0 \\ 0 & 0 & 0 & e^{-\rho} \end{pmatrix} \quad (2.121)$$

$$M_2 = \begin{pmatrix} 0 & 0 & -e^{i\pi\lambda} & 0 \\ 0 & w & 0 & -e^{i\pi\lambda} \\ e^{-i\pi\lambda} & 0 & w & 0 \\ 0 & e^{-i\pi\lambda} & 0 & 0 \end{pmatrix} \quad (2.122)$$

$$M_3 = \begin{pmatrix} e^{i\delta} & 0 & 0 & 0 \\ 0 & e^{i\delta} & 0 & 0 \\ 0 & 0 & -e^{-i\delta} & 0 \\ 0 & 0 & 0 & -e^{-i\delta} \end{pmatrix}. \quad (2.123)$$

The WKB integrals that appear in these matrices are those defined in the main text Eq. (2.13), (2.14), and (2.15). A non-trivial solution occurs only if

$$\det \left(1 - e^{2\pi i n_g} M_1 M_2 M_3 \right) = 0 \quad (2.124)$$

This condition yields a transcendental equation for the energy E , taking the form:

$$\cos \sigma = \frac{4e^\rho e^\tau [\cos(4\pi n_g) + e^\rho w \cos(2\pi n_g + \delta)]}{1 + e^{2\rho} (4e^{2\tau} + w^2) + 2e^\rho w \cos(2\pi n_g - \delta)} \quad (2.125)$$

Using the fact that $e^{-\rho} \ll 1$ and $w e^{-\tau} \ll 1$, we can simplify the denominator on the right hand side as follows:

$$1 + e^{2\rho} (4e^{2\tau} + w^2) + 2e^\rho w \cos(2\pi n_g - \delta) \approx 4e^{2\rho} e^{2\tau}.$$

Thus, the transcendental equation takes the simpler form reported as Eq. (2.12) in the main text:

$$\cos \sigma = e^{-\rho} e^{-\tau} \cos(4\pi n_g) + w e^{-\tau} \cos(2\pi n_g + \delta) \quad (2.126)$$

Note that the energy enters the bound state equation via the WKB integrals σ, ρ and τ , where it appears in both the integrand and the limits of integration.

As observed in the main text, to solve this equation a good starting point is to set the right hand side to zero, since it contains only exponentially small terms. The zeros of the left hand side occur if

$$\sigma(E_n) = \pi \left(n + \frac{1}{2} \right). \quad (2.127)$$

When taking into account the right hand side, some corrections will come from the 4π -phase slip term $e^{-\rho} e^{-\tau} \cos(4\pi n_g)$ and others will come from the 2π phase slip term $w e^{-\tau} \cos(2\pi n_g + \delta)$. We are not interested in the corrections smaller than the corrections from 4π phase slips, so the cross-terms are neglected. For the rest, we can distinguish the following three situations:

1. $w e^{-\tau} \gg e^{-\rho-\tau}$: it only makes sense to keep the leading order corrections in $w e^{-\tau}$ to each of the harmonics in the dispersion relation
2. $w e^{-\tau} \approx e^{-\rho-\tau}$: we keep the leading order $w e^{-\tau}$ corrections and the first order $e^{-\rho-\tau}$ - corrections

3. $w e^{-\tau} \ll e^{-\rho-\tau}$: enough to keep only the first order in $e^{-\rho-\tau}$.

We can conclude that in any situation it is enough to keep the leading order in $w e^{-\tau}$ and the first order in $e^{-\rho-\tau}$ for the second harmonic, although having something of the order of $e^{-\rho-\tau}$ and ignoring higher order corrections in $w e^{-\tau}$ may look inconsistent when $w e^{-\tau} \gg e^{-\rho-\tau}$.

Let's introduce the following notation:

$$E = E_n + \delta E^{(1)} + \delta E^{(2)} + \Delta E_n + \dots \quad (2.128)$$

Where $\delta E^{(m)}$ stand for m -th order corrections in $w e^{-\tau}$ (0-th in $e^{-\rho-\tau}$) and ΔE_n for the first order corrections in $e^{-\rho-\tau}$. By solving Eq. (2.126) with iterative expansions, we find:

$$\Delta E_n = \frac{(-1)^{n+1}}{\sigma'_n} e^{-\rho_n} e^{-\tau_n} \cos(4\pi n g), \quad (2.129)$$

$$\delta E_n^{(1)} = \frac{(-1)^{n+1}}{\sigma'_n} w e^{-\tau_n} \cos(2\pi n g + \delta). \quad (2.130)$$

$$\delta E_n^{(2)} = -\frac{w^2 e^{-2\tau_n} \cos^2(2\pi n g + \delta)}{(\sigma'_n)^2} \left(\tau'_n + \frac{\sigma''_n}{2\sigma'_n} \right) \quad (2.131)$$

The corrections have quite intuitive meaning. The term with τ' comes from the fact that after we consider the first order in $w e^{-\tau}$ contribution, different energies see different heights of the tunneling barrier. The term proportional to σ''_n/σ'_n is due to second order corrections to σ_n when the splitting $\delta E_n^{(1)}$ is included, and it vanishes in the harmonic limit. On the other hand, as will be shown in the next appendix, τ'_n is logarithmically large when $T\Gamma_A \gg E_C$ and thus cannot be neglected. This leads to the solution presented in the main text, Eq. (2.19). Note that in the main text we have omitted the n_g -independent part of $\delta E_n^{(2)}$, which does not affect the charge dispersion.

2.9 Appendix: Evaluation of the WKB integrals

In this appendix we derive expressions (2.21), (2.22), (2.23), and (2.24) from the main text. In doing so we assume that $\Gamma_A T \gg E_C$ and thus only look at leading contributions in the ratio $T\Gamma_A/E_C$ to the WKB integrals.

In this limit, the Bohr-Sommerfeld condition $\sigma(E_n) = \pi(n + \frac{1}{2})$ can be evaluated by expanding the integrand of $\sigma(E)$ around $\phi = 0$, and adjusting the position of the classical turning point accordingly. The result is:

$$\sigma(E) = \frac{\pi E}{\omega_p}, \quad (2.132)$$

where ω_p is the plasma frequency introduced in the main text. The result above immediately yields Eq. (2.20) of the main text as well as Eq. (2.23), $\sigma'(E) = \pi/\omega_p$.

With respect to the integral $\rho(E)$, one can see that the coefficients c and d in Eq. (2.22) are given by the integrals

$$c(T) = \frac{1}{\sqrt{8}} \int_{-\pi}^{\pi} \sqrt{1 + u(\phi)} d\phi, \quad (2.133)$$

$$d(T) = \frac{1}{\sqrt{8}} \int_{-\pi}^{\pi} \frac{d\phi}{\sqrt{1 + u(\phi)}} \quad (2.134)$$

where $u(\phi) = E_A(\phi)/\Gamma_A$. The only WKB integral which is relatively non-trivial to calculate is τ_n :

$$\tau_n = \sqrt{\frac{\Gamma_A}{E_C}} \int_{\phi_n}^{\pi} \sqrt{1 - y_n - u(\phi)} d\phi, \quad (2.135)$$

where $y_n = E_n/\Gamma_A$ and $\pm\phi_n$ are the classical turning points for E_n . It is convenient to split τ_n into three parts:

$$\tau_n \sqrt{\frac{E_C}{\Gamma_A}} \approx \int_{\epsilon}^{\pi} \sqrt{1 - u(\phi)} d\phi - \frac{y_n}{2} \int_{\epsilon}^{\pi} \frac{1}{\sqrt{1 - u(\phi)}} d\phi + \int_{\phi_n}^{\epsilon} \sqrt{1 - y_n - u(\phi)} d\phi \quad (2.136)$$

Here, ϵ is small enough so that $\sin^2 \epsilon/2 \ll 1$ but big enough such that $\sqrt{1 - y_n - u}$ can be expanded in y_n . By splitting these terms further, we may arrive at a representation in terms of elliptic functions:

$$I \approx \int_0^{\pi} \sqrt{1 - u(\phi)} d\phi - \lim_{\psi \rightarrow 0} \frac{y_n}{2} \int_{\psi}^{\pi} \frac{1}{\sqrt{1 - u(\phi)}} d\phi - \int_0^{\epsilon} \sqrt{1 - u(\phi)} d\phi \quad (2.137)$$

$$+ \lim_{\psi \rightarrow 0} \frac{y_n}{2} \int_{\psi}^{\epsilon} \frac{1}{\sqrt{1 - u(\phi)}} d\phi + \int_{\phi_n}^{\epsilon} \sqrt{1 - y_n - u(\phi)} d\phi = i_1 - i_2 + i_3 + i_4 + i_5 \quad (2.138)$$

Since $\phi_n, \epsilon \ll 1$, $i_3 + i_4 + i_5$ is quite straightforward to calculate and is equal to :

$$i_3 + i_4 + i_5 = -\sqrt{\frac{T}{2}} \frac{\sin^2 \frac{\phi_n}{2}}{2} + \frac{\sin^2 \frac{\phi_n}{2}}{2} \sqrt{\frac{T}{2}} \ln \frac{\sin^2 \frac{\phi_n}{2}}{\psi^2}, \quad \psi \rightarrow 0 \quad (2.139)$$

For i_1 we obtain the representation

$$i_1 = \frac{-4|r|}{\sqrt{1+|r|}} F(\mu(0), k) + \frac{8|r|}{\sqrt{1+|r|}} \Pi(\mu(0), 1, k) \quad (2.140)$$

where F, Π are elliptic integrals of the first and second kind, and

$$\mu(\phi) = \arcsin \sqrt{\frac{u(\phi) - |r|}{u(\phi) + |r|}}, \quad (2.141)$$

$$k = \sqrt{\frac{1 - |r|}{1 + |r|}} \quad (2.142)$$

Similarly, for i_2 we obtain:

$$\sqrt{\frac{\Gamma_A}{E_C}} i_2 = (2n + 1) \frac{\sqrt{2}|r|}{\sqrt{1 - |r|(1 + |r|)}} \times \quad (2.143)$$

$$\times \lim_{\psi \rightarrow 0} \left(2\Pi(\mu(\psi), \frac{1}{k^2}, k) - (1 - |r|)F(\mu(0), k) \right) \quad (2.144)$$

Putting all the pieces together, we obtain Eq. (2.21) of the main text with the coefficients

$$b = \lim_{\psi \rightarrow 0} \psi e^{\frac{\sqrt{2}|r|}{\sqrt{1 - |r|(1 + |r|)}} (2\Pi(\mu(\psi), \frac{1}{k^2}, k) - (1 - |r|)F(\mu(0), k))}, \quad (2.145)$$

$$a = \frac{\sqrt{8}|r|}{(1 + |r|)\sqrt{1 - |r|}} (-F(\mu(0), k) + 2\Pi(\mu(0), 1, k)). \quad (2.146)$$

These coefficients were already reported in Ref. [116]. In a similar way, for $\tau'(E_n)$ we find:

$$\tau'_n = \frac{1}{\omega_p} \ln \frac{2E_n}{\Gamma_A T b^2} \quad (2.147)$$

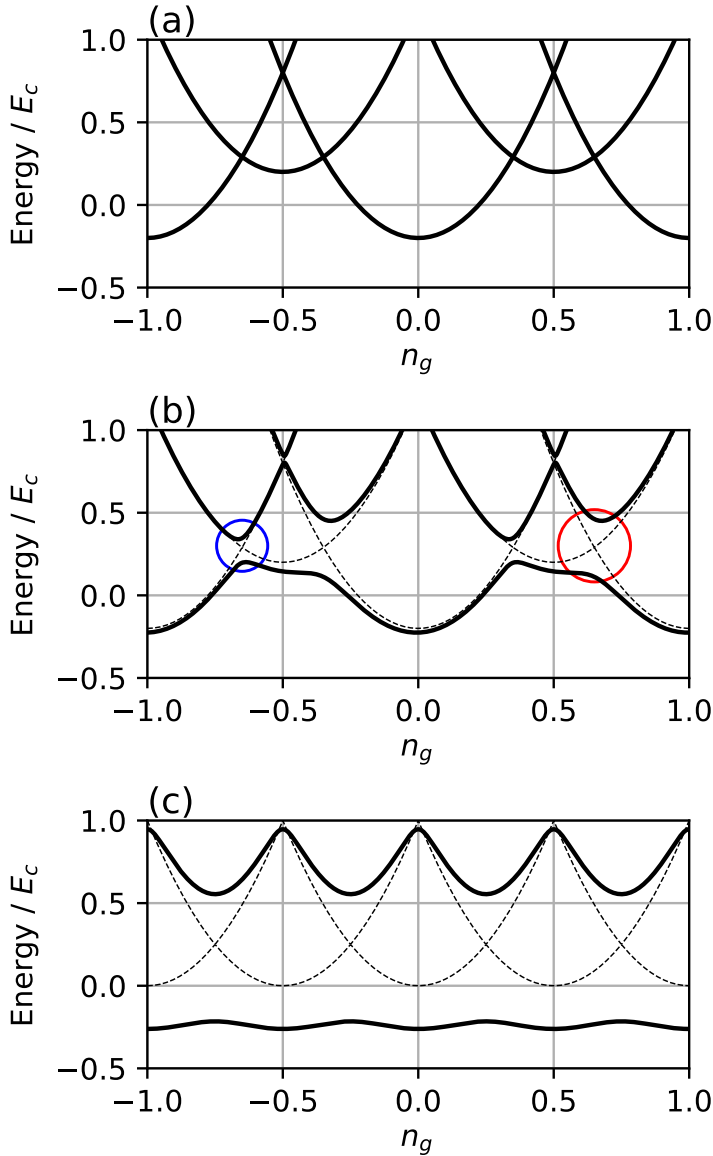


Figure 2.3. Energy spectrum of the model in the weak tunneling limit. We recall that n_g is the charge induced on the island in units of $2e$. (a): Energy levels of the model of Eq. (2.1) with $\epsilon_r/E_C = 0.2$, $\Gamma_1 = \Gamma_2 = 0$. Note that charge parabolas with the dot empty (occupied) are centered around integer (half-integer) values of n_g . (b): Energy levels with $\Gamma/E_C = 0.12$ and $\delta\Gamma/E_C = 0.06$. Blue and red circles identify avoided crossings opened by a finite Γ_1 and Γ_2 , respectively. (c): Energy levels for $\epsilon_r = 0$, $\delta\Gamma = 0$ and $\Gamma/E_C = 0.8$. In panels (b) and (c) the dashed lines represent the charge parabolas for $\Gamma_1 = \Gamma_2 = 0$.

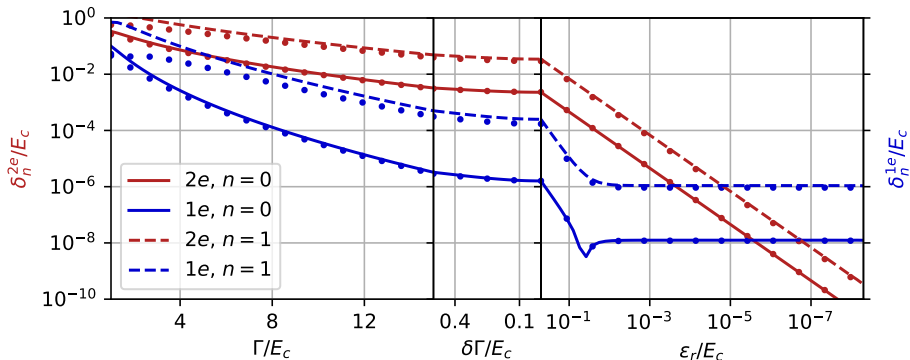


Figure 2.4. Dispersion of the energy levels of the resonant model of Eq. (2.1) versus the model parameters, as the system is tuned from the de-tuned weak-tunneling regime (left end of the plot) to the resonant strong-tunneling regime (right end of the plot). The quantities shown are the $2e$ - and $1e$ -periodic components of the charge dispersion $\delta_n(n_g)$ of the n -th energy level, for $n = 0$ and $n = 1$. For each quantity we show both the WKB prediction (solid or dashed line) as well as numerical prediction via the diagonalization of the Hamiltonian (dots). In the left panel, Γ/E_C is varied at fixed $\epsilon_r/E_C = 0.5$ and $\delta\Gamma/E_C = 0.5$. In the middle panel $\delta\Gamma/E_C$ is varied at fixed $\Gamma/E_C = 15$ and $\epsilon_r/E_C = 0.5$. In the third panel ϵ_r/E_C is varied at fixed $\Gamma/E_C = 15$ and $\delta\Gamma = 0$. Note that in the right panel the horizontal axis is also on a log scale.

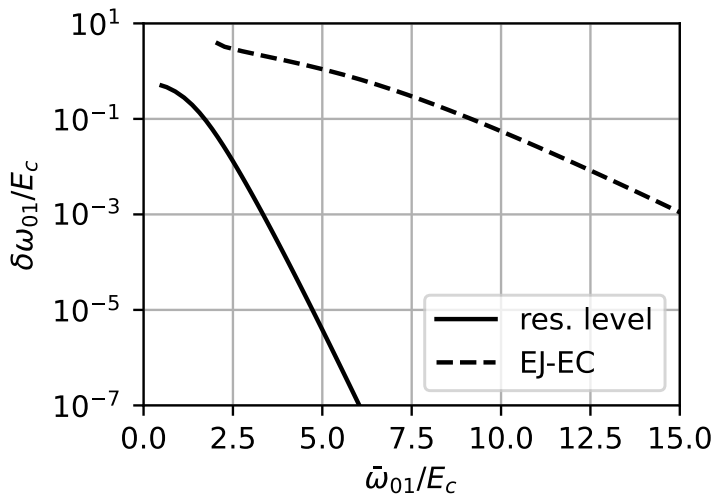


Figure 2.5. Comparison of the charge dispersion scaling in the resonant model (solid line) versus the traditional Cooper-pair box (transmon) model. We plot the peak-to-peak amplitude of the charge dispersion of the fundamental frequency $\omega_{01} = E_1 - E_0$ versus the averaged (over n_g) value of ω_{01} . For the resonant model, the curve shown is obtained varying the ratio Γ/E_C with $\delta\Gamma = \epsilon_r = 0$, while for the transmon model of Eq. (2.26) it is obtained varying E_J/E_C . In the first case, δ_{01} is dictated by 4π phase slips under a $-\Gamma \cos(\phi/2)$ barrier, while in the second case by 2π phase slips under a $-E_J \cos \phi$ barrier.

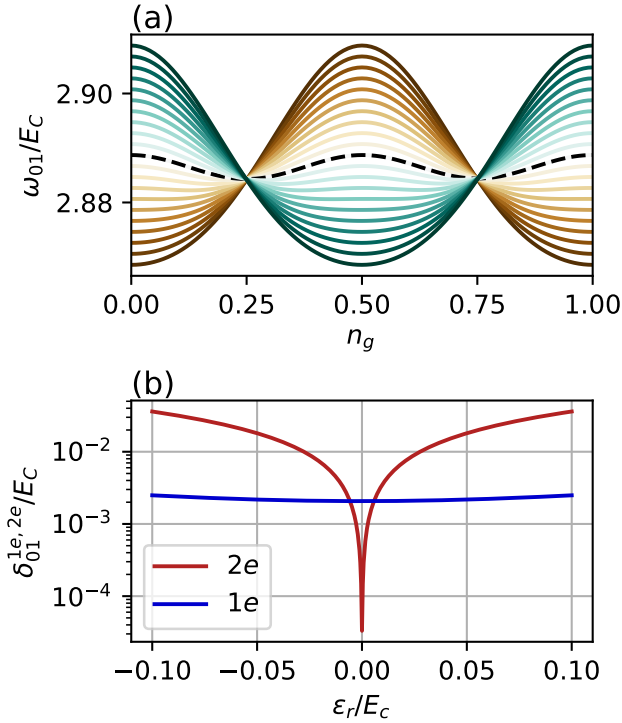


Figure 2.6. (a): Evolution of the energy difference $\omega_{01} = E_1 - E_0$, where E_1 and E_0 are the two lowest eigenvalues of Eq. (2.1), determined numerically, as a function of n_g , for different values of the detuning ϵ_r , varying between $\epsilon_r/E_C = 0.04$ (dark green) to $\epsilon_r/E_C = -0.04$ (dark brown). The black dashed line emphasizes the doubling of the periodicity at $\epsilon_r = 0$. Other parameters are $\Gamma/E_C = 5$, $\delta\Gamma/E_C = 10^{-4}$. (b): Amplitudes of the $2e$ - and $1e$ -periodic components of the charge dispersion as the resonant level is swept through resonance.

Chapter 3

Tunneling of fluxons via a Josephson resonant level

3.1 Introduction

The inductively shunted Josephson junction plays an important role in the field of superconducting quantum devices [143, 144]. The inductive link changes the topology of the circuit from that of an island to that of a loop, removing the $2e$ charge quantization associated with a superconducting island. The charge sensitivity of the device is exchanged for its flux sensitivity [27], which is exploited in the design and operation of the fluxonium qubit [28, 30–33]. Furthermore, a large shunting inductance suppresses the sensitivity to flux noise, as recently demonstrated in the blochonium qubit [34]. For this reason, the inductive shunt is a common feature of noise-protected qubit designs [111].

The minimal circuit that models this class of superconducting devices is simple: it consists of an inductor, a capacitor and a Josephson element connected in parallel [Fig. 3.1(a)]. The inductor and the Josephson junction form a loop through which an applied magnetic flux Φ is threaded. The circuit supports persistent current states, also known as *fluxons*, in which the superconducting phase winds by an integer multiple m of 2π when circling the loop [94]. Fluxons are coupled by quantum phase slips occurring at the Josephson junction¹, which change m by an integer Δm (see Fig. 3.2).

¹In principle, phase slips may also occur at other points in the loop, through the inductor. We neglect this possibility, which is analyzed in Ref. [89]

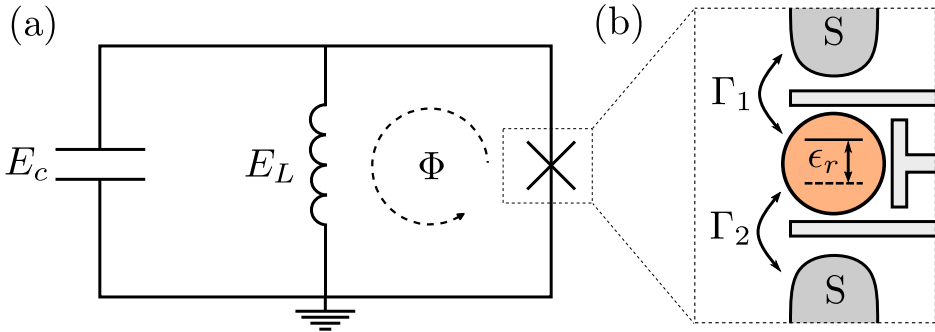


Figure 3.1. (a) Circuit of the inductively shunted Josephson junction. (b) A junction realized by a resonant level with a tunable energy ϵ_r and Cooper pair tunneling rates Γ_1 and Γ_2 .

In a typical Josephson element, e.g. in a tunnel junction, the amplitude of 2π quantum phase slips ($\Delta m = 1$) is much larger than that of 4π quantum phase slips ($\Delta m = 2$). However, if Cooper pair tunneling across the Josephson element is resonant – a type of weak link we call the Josephson resonant level – 2π quantum phase slips are suppressed [22, 114–116] and 4π quantum phase slips become the dominant coupling between fluxons. The bifluxon qubit proposal [7] achieves resonant tunneling using as a Josephson element a series of two (almost) identical tunnel junctions separated by a small superconducting island tuned (close) to a charge degeneracy point. Alternatively, resonant tunneling can also occur in a semiconductor junction, via an isolated energy level forming in a quantum dot [117, 118, 121], as represented in Fig. 3.1(b). In the latter system, experiments have demonstrated the drastic suppression of 2π quantum phase slips close to resonance [16, 17], but not yet the occurrence of the regime dominated by 4π quantum phase slips [22].

In this chapter, motivated by these experimental developments, we study in detail the energy spectrum of an inductively shunted junction with a Josephson coupling mediated by a single energy level [Fig. 3.1(b)]. We focus on the avoided crossings between energy levels directly connected to the quantum phase slip amplitudes, and measurable via microwave spectroscopy. We provide analytical expressions, backed by numerics, that capture the entire crossover between 2π - and 4π -dominated regimes near the resonance, as well as the regime away from resonance.

We also show that, when the inductive energy of the loop becomes much smaller than the Josephson plasma frequency, the circuit is well

described by a low-energy theory dual to that of a topological superconducting island. The duality we uncover extends a known duality between a superconducting loop and a superconducting island [86]. It does so by including an additional degree of freedom: the *fluxon parity* of the loop (i.e. the parity of m), which we show to be dual to the *fermion parity* of the island. Similar to fermion parity states encoded non-locally in Majorana zero modes, states with opposite fluxon parity have disjoint support in phase and provide a two-fold quasi-degeneracy to the energy spectrum; thus, they become an attractive degree of freedom to encode qubit states [7, 145]. We discuss the implications of our findings for the design of protected qubits [111, 145] in the concluding section.

3.2 Model

Given a capacitance C and an inductance L , the inductively shunted junction of Fig. 3.1(a) is described by the quantum Hamiltonian [27]:

$$\hat{H} = 4E_C \hat{n}^2 + \frac{1}{2} E_L (\hat{\phi} + \phi_{\text{ext}})^2 + V(\hat{\phi}), \quad (3.1)$$

where $E_C = e^2/2C$ and $E_L = (\Phi_0/2\pi)^2/L$. The parameter $\phi_{\text{ext}} = 2\pi\Phi/\Phi_0$ gives the applied flux Φ through the inductive loop in units of the flux quantum $\Phi_0 = h/2e$. The Cooper pair number \hat{n} and phase $\hat{\phi}$ are conjugate variables satisfying $[\hat{\phi}, \hat{n}] = i$.

The potential term $V(\hat{\phi})$ gives the Josephson energy, which for a tunnel junction would be the familiar $-E_J \cos \hat{\phi}$. For the case in which Josephson coupling is mediated by an isolated energy level, as in Fig. 3.1(b), a minimal model for the potential is:

$$V(\hat{\phi}) = -\Gamma \cos(\hat{\phi}/2)\tau_x - \delta\Gamma \sin(\hat{\phi}/2)\tau_y - \epsilon_r \tau_z. \quad (3.2)$$

Here, the Pauli matrices τ_x, τ_y, τ_z act on the two-level system corresponding to the resonant level being empty or doubly occupied; $\Gamma = \Gamma_1 + \Gamma_2$ and $\delta\Gamma = \Gamma_1 - \Gamma_2$ are the sum and difference of the $2e$ tunneling rates Γ_1 and Γ_2 between the two leads and the resonant level; and finally ϵ_r is the energy of the resonant level [see Fig. 3.1(b)]. This model for the Josephson resonant level has been discussed in Refs. [18, 19, 22]. Among other things, these works discuss the role of a charging energy of the resonant level, as well as the effect of additional transport channels and the continuum part of the density of states; all elements which we do not include in our work for simplicity.

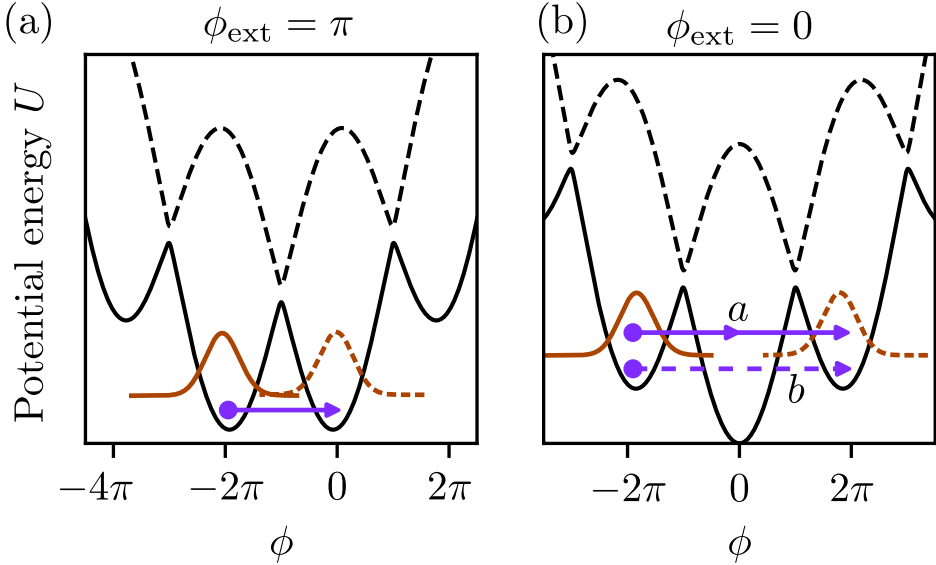


Figure 3.2. Potential landscape of the model of Eq. (3.1). We depict the two branches of the potential energy $U(\phi) = \frac{1}{2}E_L(\phi + \phi_{\text{ext}})^2 \pm E_A(\phi)$. (a) When the external flux is equal to half a flux quantum, fluxons are localized around the Josephson potential minima at $\phi = 0, 2\pi$ (wave functions shown in orange). Fluxons can tunnel between the minima via a 2π quantum phase slip (purple arrow). (b) When the external flux is zero, fluxons localized around $\phi = \pm 2\pi$ can tunnel via 4π quantum phase slips. Because of the second branch of the potential, the 4π quantum phase slips can follow two interfering paths labeled a and b (solid and dashed arrows), as described in the text.

The potential in Eq. (3.2) also applies to the bifluxon circuit deep in the charging regime of the middle island [7], but parameters have a slightly different meaning: Γ_1 and Γ_2 are Josephson energies of two tunnel junctions, and ϵ_r is the energy difference between two even-parity charge states of the superconducting island.

Fluxonium devices are typically operated in a parameter regime such that there is approximately one bound state in each of the local minima of the modulated potential of Eq. (3.1) [28]. These bound states are fluxons with a parabolic energy dispersion $\approx \frac{1}{2}E_L(2\pi m + \phi_{\text{ext}})^2$ [see Fig. 3.3(a)], and become degenerate for particular values of ϕ_{ext} . At the degeneracy points, quantum phase slips create coherent superpositions of fluxons.

In particular, at $\phi_{\text{ext}} = \pi$ the potential landscape is a degenerate double well for fluxons with $m = 0$ and $m = -1$, which couple via 2π

quantum phase slips [see Fig. 3.2(a)]. At $\phi_{\text{ext}} = 0$, instead, fluxons with $m = \pm 1$ occupy degenerate minima symmetrically placed around $\phi = 0$, and are coupled by 4π quantum phase slips [see Fig. 3.2(b)]. When $V(\phi) = -E_J \cos \phi$, the 4π quantum phase slips have a much smaller amplitude than 2π ones, since they are a higher-order process involving two 2π -slips [27].

This is not necessarily the case for the Josephson resonant level [Eq. (3.2)], because of the presence of a second branch corresponding to an excited Andreev pair in the junction [146]. Indeed, the matrix-valued potential $V(\hat{\phi})$ has eigenvalues $\pm E_A$, with

$$E_A = \Gamma_A \sqrt{\cos^2(\phi/2) + |r|^2 \sin^2(\phi/2)}, \quad (3.3)$$

where

$$\Gamma_A = \sqrt{\Gamma^2 + \epsilon_r^2}, \quad (3.4)$$

and

$$r = \frac{\epsilon_r + i\delta\Gamma}{\Gamma_A} \quad (3.5)$$

is the reflection amplitude of the junction.

The excited energy branch $+E_A$ is shown as a black dashed line in Fig. 3.2(a,b). The relevant feature of Eq. (3.3) is an avoided crossing of magnitude $|r|\Gamma_A$ at $\phi = \pm\pi, \pm 3\pi, \dots$. In the next section we show that in the limit $r \rightarrow 0$, when the branches cross, the amplitude of 2π phase slips vanishes. The system thus enters the regime in which 4π phase slips are dominant.

3.3 Wentzel–Kramers–Brillouin (WKB) analysis

An observable consequence of quantum phase slips are avoided crossings in the flux dependence of the energy spectrum of the circuit, see Fig. 3.3. There, $\Delta_{2\pi}$ is the splitting of the crossing between states with $m = 0$ and $m = -1$ at $\phi_{\text{ext}} = \pi$; it originates from 2π phase slips. $\Delta_{4\pi}$ is the splitting of the crossing between states with $m = -1$ and $m = 1$ at $\phi_{\text{ext}} = 0$; it originates from 4π phase slips. The magnitude of these avoided crossings can be computed using the WKB method [129], with calculations similar to the one described in detail in Ref. [22]. One must perform separate calculations to determine $\Delta_{2\pi}$ and $\Delta_{4\pi}$, respectively using the two potential landscapes at $\phi_{\text{ext}} = \pi$ and $\phi_{\text{ext}} = 0$ [Fig. 3.2(a,b)]. In both

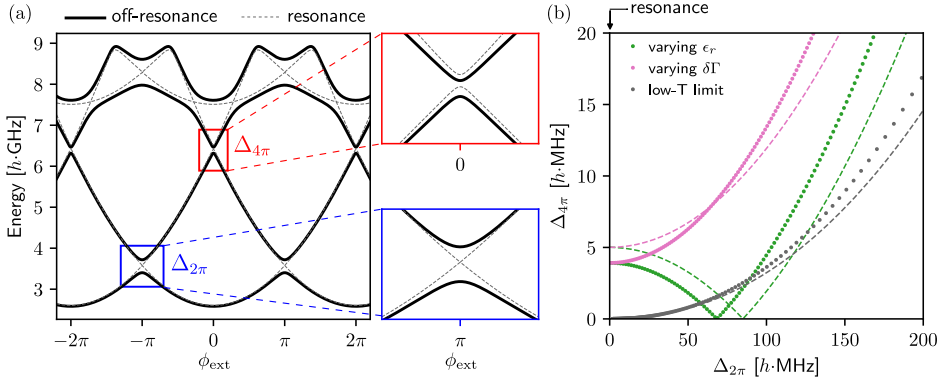


Figure 3.3. (a) Energy spectrum as a function of flux, ϕ_{ext} . The blue and red insets zoom in on the avoided crossings due to 2π and 4π quantum phase slips respectively (the vertical span of the insets is 1 GHz). The energies are computed numerically from Eq. (3.1), with $E_C/h = 2.5$ GHz, $E_L/h = 0.25$ GHz, $\Gamma/h = 5$ GHz, $\delta\Gamma/h = \epsilon_r = 0.5$ GHz. These parameters correspond to a reflection coefficient $|r| = 0.14$. The dashed gray lines illustrate the resonant case in which $\epsilon_r = \delta\Gamma = 0$ and so $r = 0$. (b) Comparison of the avoided crossings $\Delta_{2\pi}$ and $\Delta_{4\pi}$ when sweeping system parameters. For all curves, we fix $E_C/h = 2.5$ GHz and $E_L/h = 0.25$ GHz. The pink and green data show results obtained approaching resonance in two different ways. In both cases we set $\Gamma/h = 10$ GHz. In green, ϵ_r/h is varied between 0 and 1 GHz, with $\delta\Gamma = 0$. In pink, $\delta\Gamma/h$ is varied instead between 0 and 1 GHz, with $\epsilon_r = 0$. For both curves, $|r| \approx 0.1$ on the right side of the plot, and tends towards 0 on the left side of the plot, where $\delta\Gamma = \epsilon_r = 0$ and $\Delta_{2\pi}$ vanishes. Dots are computed numerically by diagonalizing Eq. (3.1), while dashed lines are obtained from the WKB result of Eqs. (3.6) and (3.9). The grey dots show the low-transparency scaling obtained from numerical diagonalization of Eq. (3.1) with $V(\hat{\phi}) = -E_J \cos \hat{\phi}$, varying E_J/h between 10 and 40 GHz. The dashed line corresponds to the $T \ll 1$ limit of Eqs. (3.6) and (3.9), with the correspondence $E_J = \Gamma_A T/4$.

cases, the presence of a second branch of the potential crucially modifies the WKB tunneling amplitude under the barrier separating different local minima [22, 114–116, 136].

In this section, we discuss the implications of this fact using a WKB calculation appropriate for the parameter regime typical of fluxonium qubits, in particular with respect to the value of E_L . In the next section, the results are generalized to arbitrarily low values of the inductive energy.

For the 2π quantum phase slips at $\phi_{\text{ext}} = \pi$, under validity conditions

discussed at the end of the Section, one obtains

$$\Delta_{2\pi} = w(r) \omega_p \left(\frac{b_0^2 \omega_p}{2\pi E_C} \right)^{1/2} \exp \left(-b_1 \frac{\omega_p}{E_C} + b_2 \frac{E_L}{\omega_p} \right). \quad (3.6)$$

where

$$\omega_p = \sqrt{2T\Gamma_A E_C}, \quad T = 1 - |r|^2, \quad (3.7)$$

and b_0, b_1, b_2 are numerical coefficients which depend smoothly on the transmission probability T . They are given in Appendix 3.6. The prefactor $w(r)$ is given by

$$w = \sqrt{\frac{2\pi}{\lambda} \frac{e^{-\lambda} \lambda^\lambda}{\Gamma(\lambda)}}, \quad \lambda = \frac{|r|^2 \Gamma_A}{4} \frac{\Gamma_A}{\Gamma} \sqrt{\frac{\Gamma_A}{E_C}}. \quad (3.8)$$

with $\Gamma(\lambda)$ the gamma function evaluated at λ , not to be confused with tunneling rates. The amplitude w vanishes when $r \rightarrow 0$, making the fluxon bound states degenerate at $\phi_{\text{ext}} = \pi$. The parameter λ sets the scale for the crossover into the degenerate regime: the suppression of $\Delta_{2\pi}$ takes place when $\lambda \ll 1$, namely when $|r|^2 \ll \sqrt{E_C/\Gamma}$, while $w \approx 1$ in the opposite limit $\lambda \gg 1$. The mechanism behind the suppression is the imaginary-time Landau-Zener transition across the avoided crossing [114].

The WKB calculation of $\Delta_{4\pi}$ is more delicate, because there are two tunneling paths between the minima at $\phi = \pm 2\pi$, labeled a and b in Fig. 3.2(b). They differ by the branch of the potential that they take between the two avoided crossings at $\phi = \pm\pi$. Path a takes place via the lower branch of the potential. It consists of the sequence of two 2π phase slips, passing through a classically available region around $\phi = 0$. Path b , instead, takes place via the excited branch of the potential and passes through a single 4π -wide tunneling barrier.

Notably, the two contributions interfere. The interference phase is that of the reflection amplitude $r = |r| e^{i\alpha}$, which distinguishes the path going through the avoided crossings from the one which does not. The sensitivity of energy levels to the phase acquired at the avoided crossing is akin to the Landau-Zener-Stückelberg interference [147]. The final result for the energy splitting takes the form

$$\Delta_{4\pi} = \sqrt{\Delta_a^2 + \Delta_b^2 - 2 \Delta_a \Delta_b \cos(2\alpha)}. \quad (3.9)$$

Here, Δ_a is the contribution due to the sequence of two 2π phase slips. It takes the form:

$$\Delta_a = \frac{\Delta_{2\pi}^2}{4\pi^2 E_L} \left(\frac{b_0^2 \omega_p}{2E_C} \right)^{2\pi^2 E_L / \omega_p} \quad (3.10)$$

where $\Delta_{2\pi}$ is the same as given in Eq. (3.6). Note that this contribution vanishes when $r \rightarrow 0$. On the other hand, Δ_b is the amplitude of a direct 4π quantum phase slip. It does not vanish at resonance, and is given by

$$\Delta_b = \omega_p \left(\frac{b_0^2 \omega_p}{2\pi E_C} \right)^{1/2} \exp \left(-b_3 \sqrt{\frac{\Gamma_A}{E_C}} + b_4 \frac{E_L}{\omega_p} + b_5 \right) \quad (3.11)$$

with b_3, b_4, b_5 another three coefficients smoothly depending on T , also given in Appendix 3.6.

The results of Eq. (3.6) and (3.9) are illustrated in Fig. 3.3. The parametric plot of $\Delta_{4\pi}$ versus $\Delta_{2\pi}$ shows that, close to resonance, $\Delta_{2\pi}$ vanishes and $\Delta_{4\pi}$ remains finite. The 4π -dominated regime is approached differently depending on whether the junction is tuned to resonance by varying $\delta\Gamma$ or by varying ϵ_r . When $\delta\Gamma \neq 0$, $\alpha = \pi/2$ in Eq. (3.9), and so Δ_a and Δ_b can never cancel out. When $\epsilon_r \neq 0$, $\alpha = 0$, and so complete cancellation ($\Delta_{4\pi} = 0$) occurs at the value of ϵ_r such that $\Delta_a = \Delta_b$.

Eqs. (3.6) and (3.9) are valid when $E_C \ll \Gamma_A T/4$, $E_L \ll \omega_p$, and $\max(\Delta_{2\pi}, \Delta_{4\pi}) \ll E_L$, and apply only to the splitting of fluxons belonging to the lowest harmonic level in the relevant potential minima. The first condition is required for the validity of the semiclassical WKB approach. The second condition guarantees that we can disregard fluxons originating from the other harmonic levels inside the wells. Finally, the third condition allows us to ignore the presence of the higher-energy minima of the potential energy. The assumed hierarchy of energy scales is in line with experimentally reported parameters of fluxonium devices [28, 148, 149], with better accuracy in the ‘‘heavy’’ regime $E_C \ll \Gamma_A T/4$ [148, 149].

In Eqs. (3.6) and (3.11) we include contributions to the WKB exponent proportional to the small parameter E_L/ω_p . These contributions originate from the lifting of the energy minima of the periodic potential $V(\phi)$, as well as the change in the WKB momentum due to the E_L term. Although they are sub-leading contributions to the WKB integrals, and are subtle to compute, we find that they are important for the agreement with numerical calculations in the parameter regime of the aforementioned experiments, such as the parameters used in Fig. 3.3.

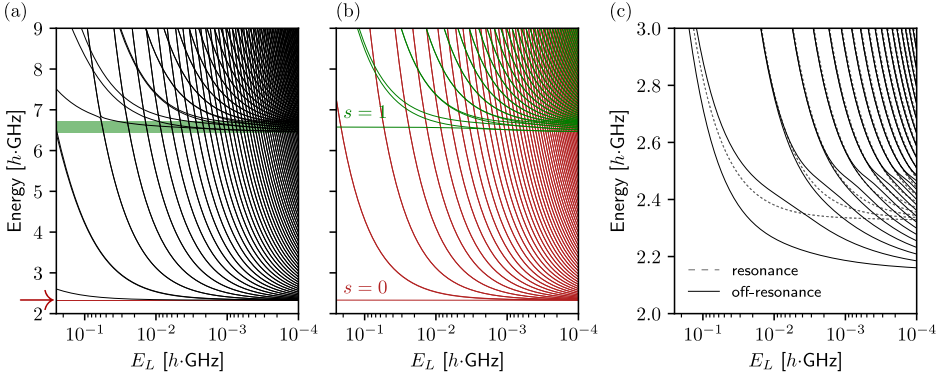


Figure 3.4. Energy spectrum as a function of decreasing inductive energy E_L . (a) Energy levels determined from direct numerical diagonalization of Eq. (3.1); the parameters are $E_C/h = 2.5$ GHz, $\Gamma/h = 5$ GHz, $\phi_{\text{ext}} = 0$, $\epsilon_r/h = 10$ MHz and $\delta\Gamma = 0$, corresponding to $r \approx 0.002$, very close to resonance. As $E_L \rightarrow 0$, the energy levels tend to fill the areas shaded in red and green. These correspond to the energy bands defined in Eq. (3.15) for $s = 0, 1$. The bandwidth of the $s = 0$ band is barely resolvable at about 16 MHz and so it is also indicated by the red arrow. (b) Result of the numerical diagonalization of the effective Hamiltonian H_s of Eq. (3.18), separately for $s = 0, 1$. The quantum phase slip amplitudes used in the effective Hamiltonian are $A_0 \approx 2.8$ MHz, $B_0 \approx 6.6$ MHz; and $A_1 \approx 7.8$ MHz, $B_1 \approx 133$ MHz. While the effective spectrum in (b) faithfully reproduces the clustering of energy levels into bands, it does not capture avoided crossings in (a) that originate from the inter-band couplings. (c) Low-lying energy levels computed for the $s = 0$ band at $\phi_{\text{ext}} = \pi$ both on resonance ($\delta\Gamma = \epsilon = 0$) and off-resonance ($\delta\Gamma = \epsilon_r = 0.5$ GHz, i.e., $|r| \approx 0.14$). The low-energy effective parameters are $A_0 = 0$ and $B_0 \approx 6.6$ MHz for the resonant case, and $A_0 \approx 160$ MHz and $B_0 \approx 7.3$ MHz for the off-resonant case. The panel illustrates the different degeneracy of energy levels that is observed in the two cases: degenerate doublets in the resonant case split off-resonance due to 2π quantum phase slips.

As long as $E_C \ll \Gamma_A T/4$, Eqs. (3.6) and (3.9) remain valid also in the low-transparency regime $T \ll 1$, away from resonance. In fact, in the limit $T \ll 1$, Eq. (3.6) and (3.9) match exactly the results of an equivalent WKB calculation done with the tunnel junction potential $V(\hat{\phi}) = -E_J \cos \hat{\phi}$, provided that one sets $E_J = \Gamma_A T/4$ so that $\omega_p = \sqrt{8E_J E_C}$. In this off-resonant regime one always has $\Delta_{4\pi} \ll \Delta_{2\pi}$, as shown by the gray lines in Fig. 3.3.

3.4 Duality with a topological superconducting island

We now ask what happens to the low energy spectrum when E_L is lowered, so that the assumption $E_L \gg \max(\Delta_{4\pi}, \Delta_{2\pi})$ behind the results from the last section is violated and the discussed eigenstates are delocalized over more minima.

The scaling of the energy spectrum of Eq. (3.1) towards the limit $E_L \rightarrow 0$ is shown in Fig. 3.4. In the limit $E_L \ll \omega_p$, as more and more local minima of the potential appear at energies below ω_p , we observe the condensation of bands of narrowly spaced energy levels. We now derive an effective Hamiltonian appropriate to describe this regime, via similar steps as those described in Ref. [27] for the standard fluxonium Hamiltonian. The derivation will establish the duality with the topological superconducting island mentioned in the introduction.

To begin with, when $E_L \ll \omega_p$, it becomes convenient to write the Hamiltonian (3.1) in the eigenbasis of its $E_L \rightarrow 0$ limit. The eigenfunctions can be represented in the following way:

$$\Psi_{ns}(\phi) = e^{-in\phi} u_{ns}(\phi) \equiv \langle \phi | n, s \rangle. \quad (3.12)$$

Here, s is an integer number that refers to a band index and n is a continuous variable, $n \in [0, 1)$. By substitution into (3.1), the spinor wave functions $u_{ns}(\phi)$ satisfy a transmon-like equation:

$$[4E_C(-i\partial_\phi - n)^2 + V(\phi)] u_{ns} = E_s(n) u_{ns}, \quad (3.13)$$

with the boundary condition that was derived in Ref. [22]:

$$u_{ns}(\phi + 2\pi) = \tau_z u_{ns}(\phi). \quad (3.14)$$

Note that u_{ns} are defined on the circle $\phi \in [0, 2\pi)$ and, at a fixed n , they form an orthonormal basis with respect to the band index s . This ensures that $\Psi_{ns}(\phi)$, which are functions of a non-compact phase, form an orthonormal basis with different s and n .

This eigenvalue problem was analyzed in Ref. [22], where we showed that the eigenspectrum takes the form:

$$E_s(n) = \epsilon_s + A_s \cos(2\pi n + \alpha_s) + B_s \cos(4\pi n + \beta_s). \quad (3.15)$$

Here, A_s and B_s are the 2π and 4π quantum phase slip tunneling amplitudes for the periodic potential $V(\phi)$, and α_s and β_s are associated phase

shifts. The bands are harmonically spaced, $\epsilon_s \approx \omega_p(s + \frac{1}{2})$, while A_s and B_s are exponentially small in ω_p/E_C . Detailed expressions as a function of E_C , Γ , $\delta\Gamma$ and ϵ_r are derived in Ref. [22] and restated in Appendix 3.7. The simple form above for the energy bands was derived via the WKB method. It is accurate for $E_C \ll \Gamma_A T/4$ and for low-lying bands.

For the lowest band, the parameters A_0 and B_0 are closely connected to the quantities $\Delta_{2\pi}$ and $\Delta_{4\pi}$ computed in the previous section. In particular, A_0 can be identified with the limit $E_L/\omega_p \rightarrow 0$ of $\Delta_{2\pi}$ in Eq. (3.6), but the same is not true for B_0 , since in Eq. (3.9) the ratio $\Delta_{2\pi}/E_L$ appears as well (i.e., both A_0 and B_0 contribute to $\Delta_{4\pi}$). We have verified numerically that the low-energy spectrum of the $s = 0$ band, discussed in more detail below, matches the expressions for the energy splittings given in Eqs. (3.6) and (3.9). This is true provided E_L is low enough to neglect the sub-leading E_L/ω_p terms in those equations, but large enough so that $E_L \gg \max(\Delta_{2\pi}, \Delta_{4\pi})$ as required in the previous section.

In the basis $|n, s\rangle$, the phase operator is represented as $\hat{\phi} = -i\partial_n - \hat{\Omega}$. It couples different bands only via the connection matrix elements $\Omega_{ss'}$:

$$\begin{aligned} \langle n, s | \hat{\Omega} | n', s' \rangle &= \delta(n - n') \Omega_{ss'}(n) \\ \Omega_{ss'}(n) &= i \int_0^{2\pi} u_{ns}^\dagger \partial_n u_{ns'} d\phi \end{aligned} \quad (3.16)$$

These can be evaluated in the same limit where (3.15) was calculated:

$$\Omega_{ss'}(n) \approx - \left(\frac{8E_C}{\Gamma_A T} \right)^{1/4} \left(\sqrt{s} \delta_{s', s+1} + \sqrt{s+1} \delta_{s', s-1} \right). \quad (3.17)$$

The interband couplings can be neglected for $E_C \ll \Gamma_A T/4$. Therefore, the original Hamiltonian of Eq. (3.1) separates into blocks labelled by the band index s :

$$H_s = \frac{1}{2} E_L (-i\partial_n + \phi_{\text{ext}})^2 + E_s(n). \quad (3.18)$$

It must be solved with the periodic boundary conditions $\psi_s(n+1) = \psi_s(n)$. The eigenvalues of this block-diagonal Hamiltonian, shown in the right panel of Fig. 3.4, compare favorably to the numerical solution of the full Hamiltonian, Eq. (3.1), shown in the left panel of Fig. 3.4.

The fluxon states localized around minima $\phi = 2\pi m$ with integer m are related to $|n, s\rangle$ via the Fourier transform:

$$|2\pi m, s\rangle = \int_0^1 dn e^{2\pi i m n} |n, s\rangle. \quad (3.19)$$

It is easy to see that, at resonance, A_s vanishes and the parity of m becomes conserved. With this in mind, we introduce in lieu of $|n, s\rangle$ a new basis $|n, \sigma, s\rangle$ endowed with a spin-like degree of freedom related to the fluxon parity:

$$|n, \uparrow, s\rangle = \frac{|n, s\rangle + |n + 1/2, s\rangle}{\sqrt{2}}, \quad (3.20)$$

$$|n, \downarrow, s\rangle = \frac{|n, s\rangle - |n + 1/2, s\rangle}{\sqrt{2}}, \quad (3.21)$$

with $n \in [0, 1/2)$. In terms of these basis states,

$$|2\pi m, s\rangle = \sqrt{2} \int_0^{1/2} dn |n, \sigma, s\rangle e^{2\pi i m n}, \quad (3.22)$$

where m is even for $\sigma = \uparrow$ and odd for $\sigma = \downarrow$.

The Hamiltonian H_s in this doubled space reads

$$H_s = \frac{1}{2} E_L (i\partial_n - \phi_{\text{ext}})^2 + A_s \sigma_x \cos(2\pi n + \alpha_s) + B_s \cos(4\pi n + \beta_s) + \epsilon_s. \quad (3.23)$$

The Pauli matrices act on the spin-like degree of freedom and the boundary conditions in the halved Brillouin zone become twisted:

$$\psi_s(n + \frac{1}{2}) = \sigma_z \psi_s(n). \quad (3.24)$$

Although Eq. (3.23) is just a re-writing of Eq. (3.18), it illuminates the fact that the low-energy description is precisely dual to that of a superconducting island shunted to ground by a topological Josephson junction with coupled Majorana zero modes [see Fig. 3.5(a)]. The Hamiltonian of such an island is [140, 150–152]

$$H_M = 4E_C (i\partial_\phi - n_g)^2 + E_M i\gamma_1 \gamma_2 \cos(\phi/2) - E_J \cos \phi. \quad (3.25)$$

Here, the first term is the charging energy of the island, n_g is the induced charge in units of $2e$, E_J represent standard Cooper pair tunneling, and the last term represents single-charge tunneling due to the Majorana zero modes γ_1 and γ_2 coupled across the topological junction (the fractional Josephson effect). Note that there are four Majorana zero modes in the model, with γ_0 and γ_1 located on the island and γ_2 and γ_3 located

on the ground plane (see Fig. 3.5). Although only γ_1 and γ_2 appear in the Hamiltonian, the boundary condition for Eq. (3.25) depends on the fermion parity operator of the island $i\gamma_0\gamma_1$:

$$\psi(\phi + 2\pi) = (-1)^p \psi(\phi), \quad (3.26)$$

with $p = (1 - i\gamma_0\gamma_1)/2 = 0$ or 1 if the parity is even or odd. The operator $i\gamma_0\gamma_1$ appearing in the boundary condition anticommutes with $i\gamma_1\gamma_2$ appearing in the Hamiltonian, just like the fluxon parity σ_z entering the boundary condition of Eq. (3.24) anticommutes with σ_x .

As illustrated in Fig. 3.5(a) and (b), the duality is established via the following correspondences: $\phi \leftrightarrow 4\pi n$, $\phi_{\text{ext}} \leftrightarrow 4\pi n_g$, $E_C \leftrightarrow 2\pi^2 E_L$, $E_J \leftrightarrow B_s$, $E_M \leftrightarrow A_s$. The operator $i\gamma_1\gamma_2$ changes the fermion parity of the island, just like the operator σ_x changes the fluxon parity. The phase shifts α_s and β_s can be included in the correspondence by adding a relative phase between the E_M and E_J terms, which could arise for instance in a superconducting quantum interference device (SQUID) configuration. Finally, we note a difference between this duality and the one between the Cooper-pair box and the phase-slip junction discussed by Mooij and Nazarov [86]: in our case, 2π quantum phase slips are dual to charge $1e$ tunneling, rather than $2e$ tunneling. This different mapping means that the duality of Mooij and Nazarov cannot be recovered simply by disregarding 4π phase slips.

It follows from the duality that, in the limit of low E_L , the flux dispersion of the energy levels of the circuit is equivalent to the charge dispersion of the energy levels of a superconducting island governed by Eq. (3.25). The first consequence of the duality is illustrated in Fig. 3.4(c), where we focus on the lowest energy levels of the $s = 0$ band when $\phi_{\text{ext}} = \pi$. In this case, at resonance, fluxon parity provides a two-fold degeneracy to the energy spectrum of the circuit, which is broken by 2π quantum phase slips away from resonance. The flux dispersion of energy levels away from this point is instead shown in Fig. 3.5: when $2\pi^2 E_L \gg B_0$, the circuit is in a ‘‘Cooper-pair box regime’’: the energy levels are essentially given by parabolas with small avoided crossings at degeneracy points [see Fig. 3.5(b)]. On the other hand, when $2\pi^2 E_L \ll B_0$, the circuit is in a ‘‘transmon regime’’ [see Fig. 3.5(c)], characterized by a flattening of the dispersion of energy levels as a function of flux. The spacing between these flat energy levels depends on the value of A_0 . If $A_0 = 0$, the energy levels become fluxon-parity degenerate doublets at all values of the flux in the

limit $E_L \rightarrow 0$, with a spacing between doublets $\sim \sqrt{E_L B_0}$ [dashed lines in Fig. 3.5(c)]. A finite but small 2π quantum phase slip amplitude splits the doublets by an amount $\approx A_0$ [solid lines in Fig. 3.5(c)].

3.5 Conclusion

The difficulty of measuring directly the 4π -dominated regime occurring at resonance lies in the smallness of 4π quantum phase slips. This was the reason, for instance, that the effect of 4π quantum phase slips was not detected in the transmon experiments of Ref. [16, 17]. The results of Fig. 3.3 show that measuring the 4π -dominated regime should be feasible in circuit with typical fluxonium parameters: $E_C/h = 2.5$ GHz and $E_L/h = 0.25$ GHz. At perfect resonance, when $\Delta_{2\pi}$ vanishes, $\Delta_{4\pi}/h \approx 5$ MHz if $\Gamma/h \approx 5$ GHz: albeit small, splittings of this magnitude have been detected and exploited in heavy fluxonium circuits [148, 153]. Larger values of $\Delta_{4\pi}$ can be obtained by decreasing Γ_A/E_C (somewhat exiting the domain of validity of our WKB results).

The 4π -dominated regime is narrow: with the parameters of Fig. 3.3, one needs $\epsilon_r/\Gamma \lesssim 10^{-3}$ and $\delta\Gamma/\Gamma \lesssim 10^{-3}$ to achieve $\Delta_{2\pi} \lesssim \Delta_{4\pi}$. For bifluxon circuits, it may be difficult to limit the asymmetry $\delta\Gamma$, which is set by the fabrication of the tunnel junctions [154, 155] and cannot be tuned afterwards, unless SQUIDs are added to the design for the purpose. For semiconductor junctions, instead, a difficulty would be to maintain ϵ_r and $\delta\Gamma$ in such narrow ranges in the presence of charge noise. However, we argue that semiconductor junctions present a qualitative advantage relative to the bifluxon: stronger coupling between the weak link region and the superconducting leads can be achieved without sacrificing anharmonicity, namely without compromising the two-level approximation used in the model for the weak link [156]. As we explain below, the possibility to increase Γ without exiting the regime of validity of the model may be beneficial to find a parameter regime which offers more benevolent conditions to observe the 4π -dominated regime.

The duality derived in Sec. 3.4 is suggestive for the design of protected qubits. In the topological superconducting island, the regime $E_M = 0$ defines a parity-protected qubit [108]: as long as $E_J \gg E_C$, noise acting on the island can neither dephase nor flip the qubit encoded in the parity of the Majorana pair. In our inductive loop, a similar regime corresponds to the resonant condition $A_0 = 0$ together with the condition $2\pi^2 E_L \ll$

B_0 [7]. In this regime, noise in the loop cannot dephase or flip the qubit encoded in the fluxon parity of the loop. The former process is suppressed exponentially in the ratio $\sqrt{8B_0}/(2\pi^2 E_L)$.

From the theoretical point of view, both models discussed in Sec. 3.5 can be cast as a one-dimensional tight-binding model in which the nearest-neighbor hopping (E_M or A_0) can become smaller than the next-nearest neighbor hopping (E_J or B_0); the hopping represents tunneling of charge or flux depending on the side of the duality. When the nearest-neighbor hopping is set to zero but the next-nearest neighbor hopping is not, the one-dimensional lattice disconnects in two separate pieces, corresponding to “even” and “odd” sites of the lattice. Protected qubits can then be encoded in the parity degree of freedom: parity states are degenerate and have disjoint support. The degeneracy is broken by the inductive or charging energy, which assigns different energies to even and odd sites, but does not couple them ². With this general picture in mind, it becomes intuitive to see that the duality can be extended to other circuits – for instance, a transmon with both a $\cos(\phi)$ and a $\cos(2\phi)$ Josephson element – thus defining a sort of equivalence class of different models of protected superconducting qubits. Dualities of this type have also been discussed in Ref. [157].

From a practical point of view, an immediate problem with the protected regime of our model is the requirement for extreme smallness of E_L : to the best of our knowledge, the current record in the literature stands at $E_L/h \approx 65$ MHz [34], likely higher than what would be needed for the condition $2\pi^2 E_L \ll B_0$. A related issue is that the level spacing would be in the MHz range, requiring some active cooling to reach the quantum regime at accessible temperatures (milliKelvin scale). At low values of E_L – often reached via high-kinetic inductance thin-films with very low Cooper-pair densities – the occurrence of phase slips across the inductor, neglected here, may also have to be taken into account. A common strategy to minimize all the problems mentioned so far is to increase the quantum phase slip rates as well as the plasma frequency, essentially trying to maximize both Γ_A and E_C while keeping the ratio Γ_A/E_C constant and of order one. Using superconductors with a larger energy gap than Al in the resonant level junction would allow more room to increase

²When dealing with the Hamiltonian (3.25), one has to keep in mind that the boundary conditions (3.26) are twisted. After one makes a gauge transform to change the boundary conditions to periodic, the equilibrium charge n_g in the kinetic term is shifted differently for different parities.

Γ_A without exiting the tunneling limit. It is also essential to minimize the quasiparticle poisoning rate of the quantum dot (which is an analogue of the poisoning events of the Cooper pair box island in the bifluxon [7]), as our model (3.2) assumes even occupation numbers of the Andreev bound state.

Even then, the protected regime is fine-tuned by the need for the resonant condition to eliminate 2π quantum phase slips, which couple fluxons of different parity, breaking the parity protection. Possible circuit extensions that work around this fine-tuning problem were already discussed in the bifluxon proposal of Ref. [7] and could be adapted to semiconductor junctions as well.

Despite these obstacles, the existence of a protected regime, corroborated by the duality derived in this work, will make it interesting and rewarding to reach the hard-to-reach parameter regime in which the inductive energy becomes much smaller than the quantum phase slip rates.

3.6 Appendix: Definitions of the coefficients

In this Appendix, we give the explicit expressions for the coefficients $b_0, b_1, b_2, b_3, b_4, b_5$ used in the previous sections of this chapter. We introduce auxiliary definitions first:

$$u(\phi) = E_A(\phi)/\Gamma_A = \sqrt{1 - T \sin^2(\phi/2)}, \quad (3.27)$$

$$\mu(\phi) = \arcsin \sqrt{\frac{u(\phi) - |r|}{u(\phi) + |r|}}, \quad (3.28)$$

$$h = \frac{|r|}{(1 + |r|) \sqrt{1 - |r|}}, \quad (3.29)$$

$$k = \sqrt{\frac{1 - |r|}{1 + |r|}}. \quad (3.30)$$

Then b_0 and b_1 are defined in terms of elliptic integrals of the first and second kind, as follows:

$$b_0 = \lim_{\psi \rightarrow 0} \psi e^{\sqrt{2}h[2\Pi(\mu(\psi), k^{-2}, k) - (1 - |r|)F(\mu(0), k)]} \quad (3.31)$$

$$b_1 = \sqrt{8}h [-F(\mu(0), k) + 2\Pi(\mu(0), 1, k)]. \quad (3.32)$$

For the rest of the coefficients, we have:

$$b_2 = \sqrt{\frac{T}{8}} \int_0^\pi \frac{(\pi^2 - \phi^2) d\phi}{\sqrt{1 - \sqrt{1 - T \cos^2 \phi/2}}}. \quad (3.33)$$

$$b_3 = \sqrt{2T} b_1 + \int_0^\pi \sqrt{1 + u(\phi)} d\phi \quad (3.34)$$

$$b_4 = \sqrt{\frac{T}{8}} \int_0^\pi \left[\frac{\phi(4\pi - \phi)}{\sqrt{1 - u(\phi)}} + \frac{4\pi^2 - \phi^2}{\sqrt{1 + u(\phi)}} \right] d\phi, \quad (3.35)$$

$$b_5 = \sqrt{\frac{T}{8}} \int_0^\pi \frac{d\phi}{\sqrt{1 + u(\phi)}}. \quad (3.36)$$

3.7 Appendix: Expressions for the low-energy Hamiltonian parameters

The expressions below are given in Ref. [22], where A_s, B_s are denoted $\delta_s^{2e}, \delta_s^{1e}$ and α_s, β_s are denoted $\beta_s^{2e}, \beta_s^{1e}$ respectively. We state them here for convenience. They have been derived using parabolic cylinder functions near the minima of the Josephson potential. The intermediate expressions (3.37), (3.39), (3.40) are different from [22], but the results for A_s, α_s and B_s, β_s are the same after the substitution of (3.39) into (3.37), (3.40). The 2π -tunneling amplitude and phase for a band s are given by:

$$A_s = \frac{w\omega_p}{z\pi} e^{-\tau_s}, \quad \alpha_s = \pi(s+1) - \alpha \quad (3.37)$$

$$z = \frac{s! e^{s+1/2}}{(s+1/2)^{s+1/2} \sqrt{2\pi}}, \quad (3.38)$$

with w and α as defined in the main text. Here, τ_s is some WKB integral that can be evaluated to:

$$e^{-\tau_s} = \frac{z\sqrt{2\pi}}{s!} \left(\frac{b_0^2 \omega_p}{4E_C} \right)^{s+1/2} \exp \left(-b_1 \frac{\omega_p}{E_C} \right). \quad (3.39)$$

Note that the expression for $A_{s=0}$ coincides with Eq. (3.6) when $E_L/\omega_p \rightarrow 0$.

For 4π phase slips, there are two terms contributing to the overall amplitude B_s and phase β_s , which are defined by the equality:

$$B_s \cos(4\pi n + \beta_s) = \frac{(-1)^{s+1} \omega_p}{\pi z} e^{-\rho_s} e^{-\tau_s} \cos(4\pi n) + \frac{w^2 \omega_p}{2\pi^2 z^2} \log \left[\frac{b_0^2 \omega_p}{4E_C \left(s + \frac{1}{2}\right)} \right] e^{-2\tau_s} \cos(4\pi n - 2\alpha). \quad (3.40)$$

Here ρ_s is another WKB integral, this time evaluating to

$$\rho_s = (b_3 - \sqrt{2T}b_1) \sqrt{\frac{\Gamma_A}{E_C}} - b_5 (2s + 1). \quad (3.41)$$

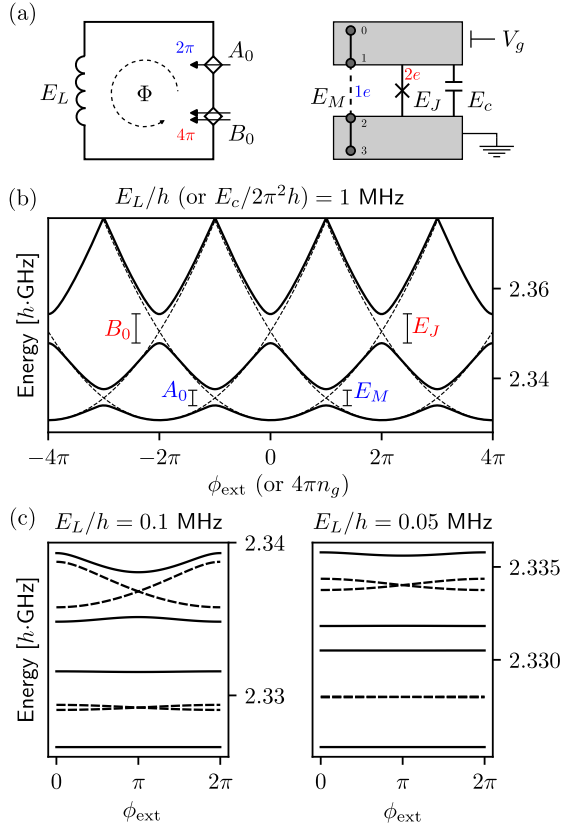


Figure 3.5. (a) Schematic illustration of the duality between a superconducting loop (left) with 2π and 4π phase slip elements A_0 and B_0 and a topological superconducting island (right) with $1e$ and $2e$ tunnel couplings E_M and E_J . The four grey dots on the right represent four Majorana zero modes, two on the island and two on the ground. Φ and V_g are the flux and voltage applied to the loop and island, corresponding to the tuning parameters $\phi_{\text{ext}} = 2\pi \Phi/\Phi_0$ and $n_g = CV_g/2e$. (b) Dispersion of the three lowest energy levels of the circuit as a function of flux, obtained from diagonalization of the $s = 0$ band Hamiltonian of Eq. (3.18). We set $E_C/h = 2.5$ GHz and $\Gamma/h = 5$ GHz, and $\epsilon_r/h = \delta\Gamma/h = 10$ MHz. In these conditions, the quantum phase slip parameters of Eq. (3.18) are $A_0 \approx 3.3$ MHz and $B_0/h \approx 6.7$ MHz. The dashed parabolas are the energies of uncoupled fluxons, which are dual to uncoupled charge states. Labels relate avoided crossings to model parameters on either side of the duality. (c) Flux dispersion of the energy levels of the circuit for lower values of E_L , illustrating the “transmon” regime. The solid lines are obtained for the same parameters as in panel (b), while the dashed lines are obtained at resonance: $\epsilon_r = \delta\Gamma = 0$. In this case, $A_0 = 0$ and energy levels gather in almost degenerate doublets. In panel (b), $B_0/(2\pi^2 E_L) \approx 0.3$, while in panel (c) $B_0/(2\pi^2 E_L) \approx 3.3$ and 6.6 . Note that the vertical energy scale changes between plots, following the reduction in E_L .

Chapter 4

Phase-shifted Andreev levels in an altermagnet Josephson junction

4.1 Introduction

Altermagnets (metals with a d -wave magnetization that "alternates" direction in momentum space) differ from ferromagnets and antiferromagnets in that they combine a spin-polarized Fermi surface with a vanishing net magnetization [64, 65, 69, 70]. Candidate altermagnetic materials include RuO_2 , MnTe , and Mn_5Si_3 [67, 72, 158, 159]. The interplay of altermagnetism and superconductivity produces unusual effects [160], including orientation-dependent Andreev reflection [77, 78], negative critical supercurrent with finite-momentum Cooper pairing [8, 9], and topological Majorana modes [79, 80].

A basic building block for these effects is the altermagnet Josephson junction, in which two s -wave superconductors (gap Δ_0 , phase difference ϕ) are connected by a d -wave magnetic region (see Fig. 4.1). The subgap excitations are Andreev levels, electron-hole superpositions confined to the junction. If the length L of the junction is short compared to the superconducting coherence length $\xi_0 = \hbar v_F / \Delta_0$, there is one Andreev level per spin direction and per transverse mode.

For a non-magnetic Josephson junction the Andreev levels are spin-degenerate, and the ϕ -dependence of the excitation energy is given by

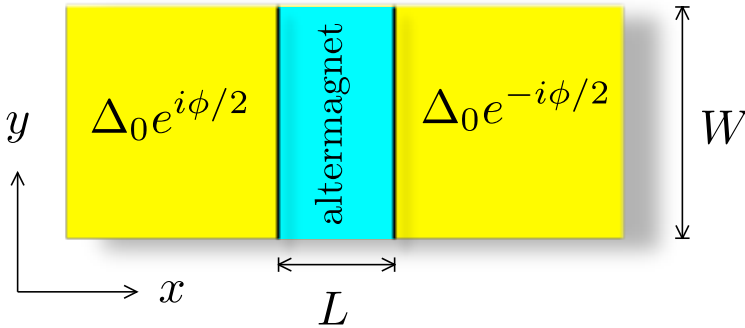


Figure 4.1. Josephson junction consisting of a pair of superconductors (pair potential Δ_0 , phase difference ϕ) connected by an altermagnet. We consider a short planar junction, $W \gg \xi_0 \gg L$.

[161]

$$E = \Delta_0 \sqrt{1 - T \sin^2(\phi/2)}, \quad (4.1)$$

where $T \in (0, 1)$ is the transmission probability through the junction of an electron mode at the Fermi level in the normal state.

Here we investigate how the altermagnet modifies the excitation spectrum. For unit transmission through a planar junction the $\cos(\phi/2)$ Andreev band is split into spin-polarized branches. The splitting is a phase shift $\pm\delta\phi$ that depends on the angle θ of the junction with the crystalline axis of d_{xy} -wave symmetry. For $\theta = 0$ the relation (4.1) with $\phi \mapsto \phi \pm \delta\phi$ still holds for non-unit transmission. We test these analytical predictions with a computer simulation of a tight-binding model of the altermagnet Josephson junction.

These results provide an alternative description of the $0-\pi$ transition reported recently [8, 9], where the sign of the critical current oscillates with increasing L . The description is particularly simple for $\theta = 0$, when the phase shift $\delta\phi$ is proportional to the transverse momentum k_y , so $\partial E/\partial\phi \propto \partial E/\partial k_y$. The supercurrent $I \propto \int_{-k_F}^{k_F} dk_y (dE/d\phi)$ is therefore directly given by an energy difference — the integral operation cancels the derivative. The resulting critical current I_c oscillates $\propto (\sin \delta\phi_{\max})/\delta\phi_{\max}$, with $\delta\phi_{\max} \propto k_F L$.

4.2 Altermagnet Josephson junction

We consider the Josephson junction geometry of Fig. 4.1, consisting of a pair of superconducting regions ($x < 0$ and $x > L$) connected by a non-superconducting magnetic metal ($0 < x < L$). The superconducting pair potential Δ has s -wave symmetry, while the magnetization has the d -wave symmetry characteristic of an altermagnet. The junction has length L and width W .

For large width W , and without impurity scattering, we may assume translational invariance in the y -direction, so that the transverse momentum k_y is a good quantum number. We work in the short-junction regime $L \ll \xi_0$.

The excitation spectrum is described by the Bogoliubov-De Gennes (BdG) Hamiltonian

$$\mathcal{H}(\mathbf{k}) = \begin{pmatrix} H_0(\mathbf{k}) & \Delta \\ \Delta^* & -\sigma_y H_0^*(-\mathbf{k}) \sigma_y \end{pmatrix}, \quad (4.2)$$

$$H_0(\mathbf{k}) = \frac{\hbar^2}{2m}(k_x^2 + k_y^2) - \mu + \frac{\hbar^2}{m} t_1 k_x k_y \sigma_z + \frac{\hbar^2}{m} t_2 (k_y^2 - k_x^2) \sigma_z. \quad (4.3)$$

The σ_α 's are Pauli spin matrices, $\mathbf{k} = (k_x, k_y)$ is the electron momentum (two-dimensional, for simplicity), and $\mu = \hbar^2 k_F^2 / 2m = \frac{1}{2} m v_F^2$ is the Fermi energy. In what follows we set $\hbar = 1$ and the electron mass $m = 1$ (restoring units in the final results).

The d -wave exchange interaction is characterised by two dimensionless parameters t_1 and t_2 , which depend on the angle θ of the altermagnet-superconductor (AS) interface relative to the crystalline axes,

$$t_1 = 2t_0 \cos 2\theta, \quad t_2 = t_0 \sin 2\theta. \quad (4.4)$$

The parameter t_0 is of order 10^{-1} [72]. For $\theta = 0$ the magnetization has pure d_{xy} -wave symmetry, for $\theta = \pi/4$ it has pure $d_{x^2-y^2}$ -wave symmetry.

The 4×4 Hamiltonian (4.2) decouples into 2×2 blocks \mathcal{H}_\uparrow and \mathcal{H}_\downarrow . The blocks are spin-polarized in the sense that electrons and holes occupy opposite spin bands, so that each block describes quasiparticles with a definite magnetic moment.

We consider the spin-up block

$$\mathcal{H}_\uparrow(\mathbf{k}) = \begin{pmatrix} H_+(\mathbf{k}) & \Delta \\ \Delta^* & -H_-(\mathbf{k}) \end{pmatrix}, \quad (4.5)$$

$$H_\pm(\mathbf{k}) = \frac{1}{2}(k_x^2 + k_y^2) - \mu \pm t_1 k_x k_y \pm t_2(k_y^2 - k_x^2). \quad (4.6)$$

The spin-down block \mathcal{H}_\downarrow is obtained by switching $t_1 \mapsto -t_1$, $t_2 \mapsto -t_2$.

Near the Fermi level ($E = 0$) we may linearize the k_x -dependence of \mathcal{H}_\uparrow at given momentum k_y , parallel to the AS interfaces at $x = 0$ and $x = L$. In the altermagnet region $0 < x < L$, where $\Delta = 0$, we have

$$\mathcal{H}_\uparrow = (\bar{v} - \tau_z \delta v) \nu_z \tau_z (k_x - Q_0 - Q_z \tau_z). \quad (4.7)$$

The Pauli matrix τ_z acts on the electron-hole degree of freedom, while ν_z distinguishes right-movers from left-movers.

In Eq. (4.7) we have introduced the velocities

$$v_\pm = v_F \sqrt{1 \pm 2t_2 - (k_y/k_F)^2 (1 - t_1^2 - 4t_2^2)} \equiv \bar{v} \pm \delta v, \quad (4.8)$$

and momentum offsets

$$\begin{aligned} Q_0 &= k_F (1 - 4t_2^2)^{-1} (\nu_z (\bar{v} - 2t_2 \delta v) / v_F - 2t_1 t_2 k_y / k_F), \\ Q_z &= k_F (1 - 4t_2^2)^{-1} (\nu_z (2t_2 \bar{v} - \delta v) / v_F - t_1 k_y / k_F). \end{aligned} \quad (4.9)$$

For later use we also define

$$\begin{aligned} Q_0^\pm &= k_F (1 - 4t_2^2)^{-1} (\pm (\bar{v} - 2t_2 \delta v) / v_F - 2t_1 t_2 k_y / k_F), \\ Q_z^\pm &= k_F (1 - 4t_2^2)^{-1} (\pm (2t_2 \bar{v} - \delta v) / v_F - t_1 k_y / k_F). \end{aligned} \quad (4.10)$$

4.3 Andreev levels without normal reflection

Andreev reflection at $x = 0$ and $x = L$ converts electrons into holes, with absorption of the missing charge of $2e$ into the superconducting condensate [14]. It coexists with normal reflection, without charge conversion. In this section we neglect normal reflections, we will include these in the next section.

Andreev reflection from electron to hole with energy E , at a pair potential $\Delta = \Delta_0 e^{i\phi}$, is associated with a phase shift $e^{-i\phi - i\alpha(E)}$, where

$$\alpha(E) = \arccos(E/\Delta_0) \in (0, \pi), \quad |E| < \Delta_0. \quad (4.11)$$

The phase shift for reflection from hole to electron is $e^{+i\phi-i\alpha(E)}$. We set $\Delta = \Delta_0 e^{i\phi/2}$ at the left superconductor ($x < 0$) and $\Delta = \Delta_0 e^{-i\phi/2}$ at the right superconductor ($x > L$).

The condition for a bound state is that the phase increment on a round-trip $x = 0 \mapsto L \mapsto 0$ is a multiple of 2π . For $k_F L \ll \mu/\Delta_0$ (equivalently, $L \ll \xi_0$, the short-junction regime) we may ignore the energy dependence of the phase shift accumulated in the normal region, while retaining the energy dependence of the Andreev reflection phase shift $\alpha(E)$. This gives the bound-state condition

$$\phi + 2LQ_z^\pm = \pm 2\alpha(E) \bmod (2\pi). \quad (4.12)$$

The \pm sign distinguishes whether the right-moving quasiparticle is an electron or a hole. The contribution Q_0 to the phase shift cancels in the round-trip, only the increment Q_z contributes.

We thus obtain two branches of Andreev levels E_\uparrow^\pm , with

$$E_\uparrow^\pm = \pm \Delta_0 \text{sign}(\sin \psi_\uparrow^\pm) |\cos \frac{1}{2} \psi_\uparrow^\pm|, \quad (4.13a)$$

$$\psi_\uparrow^\pm = \phi + 2LQ_z^\pm. \quad (4.13b)$$

We have added the subscript \uparrow as a reminder that these are the bound states of \mathcal{H}_\uparrow . For \mathcal{H}_\downarrow one replaces $L \mapsto -L$.

In a non-magnetic Josephson junction the Andreev levels are spin degenerate, with a cosine phase dependence [162]: $E = \pm \Delta_0 \cos(\phi/2)$. As illustrated in Fig. 4.2, the altermagnet breaks up the cosine into branches that are phase shifted by a spin-dependent amount. Each branch connects the edges of the gap at $\pm \Delta_0$, where the bound states merge with the continuous spectrum. Electron-hole symmetry ($\pm E$ symmetry of the spectrum) is ensured by the identity

$$Q_z^+(k_y) = -Q_z^-(-k_y) \Rightarrow E_\uparrow^\pm(k_y) = -E_\downarrow^\mp(-k_y). \quad (4.14)$$

4.4 Including normal reflection

An electron incident on the superconductor may be Andreev reflected as a hole, but it may also be reflected as an electron. Such normal reflection can be modeled by the insertion of a tunnel barrier at the two ends of the altermagnet. We assume that the barrier potential $V(x)$ does not break the translational invariance along the y -direction, so that the transverse

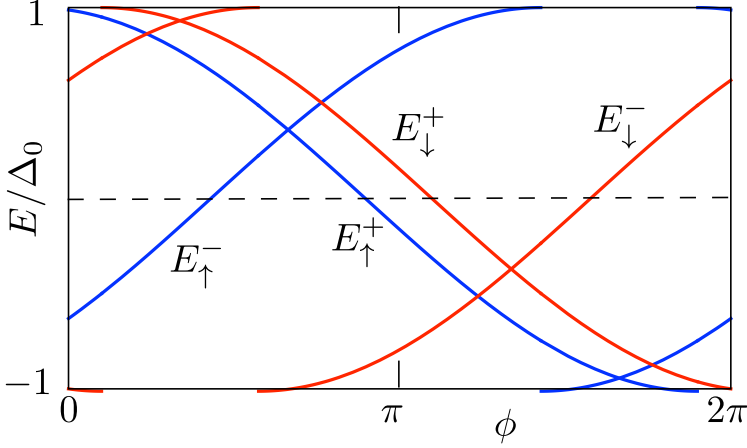


Figure 4.2. Phase dependence of the Andreev levels, computed from Eq. (4.13) for $t_1 = t_2 = 0.1$, $k_F L = 20$, $k_y/k_F = 1/2$. There are four levels at each value of the phase difference, distinguished by the spin direction \uparrow, \downarrow and by the \pm sign of the current $\propto dE/d\phi$ which they carry. Another four levels at $k_y/k_F = -1/2$ ensures the electron-hole symmetry of the spectrum. Normal reflections are neglected in this calculation.

momentum k_y remains a good quantum number. We also assume the potential is spin-independent.

A simple solution of the scattering problem is possible for pure d_{xy} -wave pairing ($t_2 = 0$). The BdG Hamiltonian then reads

$$\begin{aligned} \mathcal{H} = & \left[\frac{1}{2}k_x^2 + \frac{1}{2}k_y^2 + V(x) - \mu \right] \tau_z \\ & + \frac{1}{2} [t_1(x)k_x + k_x t_1(x)] k_y \sigma_z \\ & + \Delta_0(x) [\tau_x \cos \phi(x) - \tau_y \sin \phi(x)]. \end{aligned} \quad (4.15)$$

The x -dependence of the magnetization and pair potential is included to describe the entire junction profile. The anticommutator of $t_1(x)$ and k_x ensures the hermiticity of \mathcal{H} [77].

We make the unitary transformation $\mathcal{H} \mapsto U(x)\mathcal{H}U^\dagger(x)$, with

$$U(x) = \exp \left(i\tau_z \sigma_z k_y \int_0^x t_1(x') dx' \right), \quad (4.16)$$

resulting in

$$\begin{aligned} \mathcal{H} = & \left(\frac{1}{2}k_x^2 + \frac{1}{2}(1 - t_1^2)k_y^2 + V(x) - \mu \right) \tau_z \\ & + \Delta_0(x) (\tau_x \cos \tilde{\phi}(x) - \tau_y \sin \tilde{\phi}(x)), \end{aligned} \quad (4.17)$$

where $\tilde{\phi}(x) = \phi(x) + 2\sigma_z k_y \int_0^x t_1(x') dx'$ is a spin-dependent phase difference.

So for a given k_y and given spin direction, the altermagnet Josephson junction is equivalent to a nonmagnetic Josephson junction with phase difference $\phi \pm 2k_y L t_1$. The factor $1 - t_1^2$ that multiplies k_y^2 in Eq. (4.17) amounts to an anisotropic mass, this factor can be set to unity for $t_1 \ll 1$. We can then use the known result (4.1) for the Andreev levels in a nonmagnetic Josephson junction,

$$\begin{aligned} E_{\uparrow}^{\pm}(k_y) &= \pm \Delta_0 \sqrt{1 - T(k_y) \sin^2(\phi/2 - k_y L t_1)}, \\ E_{\downarrow}^{\pm}(k_y) &= \pm \Delta_0 \sqrt{1 - T(k_y) \sin^2(\phi/2 + k_y L t_1)}, \end{aligned} \quad (4.18)$$

where $T(k_y)$ is the transmission probability through the junction in the normal state ($\Delta_0 = 0$).

If t_2 is nonzero we do not have such a closed-form and general expression for the Andreev levels. We specify to the case of a tunnel barrier at each AS interface, with tunnel probability Γ (the same at $x = 0$ and at $x = L$). The scattering matrix calculation in App. (4.8) gives the spin-up Andreev levels E_{\uparrow}^{\pm} as the two solutions of the nonlinear equation

$$\begin{aligned} (1 - \Gamma)^2 \cos(2\alpha(E) + L(Q_z^+ - Q_z^-)) + \cos(2\alpha(E) - L(Q_z^+ - Q_z^-)) - \\ - \Gamma^2 \cos(\phi + L(Q_z^+ + Q_z^-)) = 2(1 - \Gamma) \cos(L(Q_z^+ - Q_z^-)) + \\ + 4(1 - \Gamma) \cos(L(Q_0^+ - Q_0^-))(1 - E^2/\Delta_0^2). \end{aligned} \quad (4.19)$$

The spin-down Andreev levels E_{\downarrow}^{\pm} are the solutions of Eq. (4.19) upon replacement of L by $-L$.

As a check, if we now set $t_2 = 0$ we have $Q_z^+ = Q_z^-$, $Q_0^+ = -Q_0^-$, and Eq. (4.19) has the solution (4.18) with

$$T(k_y) = \frac{\Gamma^2}{2(1 - \Gamma) \cos 2LQ_0^+ + 1 + (1 - \Gamma)^2}. \quad (4.20)$$

This is indeed the normal-state transmission probability through a double-barrier junction, at momentum $Q_0^+ = \sqrt{k_F^2 - (1 - t_1^2)k_y^2}$.

If $t_2 \neq 0$ Eq. (4.19) can readily be solved numerically. As illustrated in Fig. 4.3, crossings in the spectrum between levels of the same spin become anticrossings.

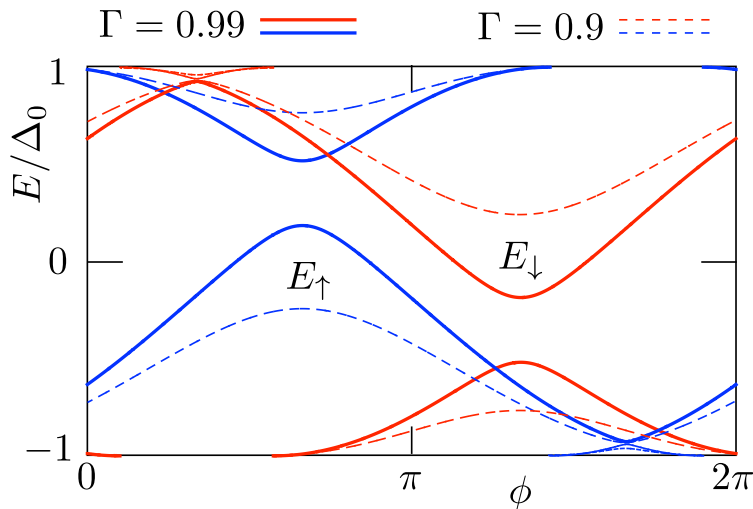


Figure 4.3. Same as Fig. 4.2, but now including normal reflections at each AS interface. The spectra are calculated from Eq. (4.19) for two values of the transmission probability Γ , at $t_1 = t_2 = 0.1$, $k_F L = 20$, $k_y/k_F = 1/2$.

4.5 Comparison with computer simulations

To test these analytical predictions we have discretized the BdG Hamiltonian (4.3) on a square lattice and computed the subgap excitation spectrum numerically (see App. 4.9). These computer simulations fully include the normal reflections at the AS interfaces and they do not rely on the short-junction approximation.

In Fig. 4.4 we compare with the analytical predictions that ignore normal reflection. As expected, the main effect of normal reflection at the AS interfaces is to transform the crossings between same-spin branches into anticrossings. The effect is most pronounced when t_1 and t_2 are both nonzero: In the two cases of pure d_{xy} -wave or pure $d_{x^2-y^2}$ -wave magnetization the crossings are only weakly affected.

In Fig. 4.5 we test the relation (4.18) between the Andreev levels and the normal-state transmission probability in the case of d_{xy} -wave pairing. The agreement is quite good, without any adjustable parameter.

4.6 Josephson energy and supercurrent

The supercurrent in the short-junction regime is carried entirely by the bound states, the continuous spectrum does not contribute [5, 161]¹. In equilibrium at inverse temperature β the supercurrent I is given by the phase derivative of the Josephson energy F ,

$$I = \frac{2e}{\hbar} \frac{d}{d\phi} F, \quad F = - \sum_{E>0} \frac{1}{2} E \tanh(\frac{1}{2}\beta E), \quad (4.21)$$

where $\sum_{E>0}$ is a sum over the transverse momentum k_y and spin \uparrow, \downarrow of the Andreev levels in the interval $(0, \Delta_0)$.

In the absence of normal reflections, we find from Eqs. (4.13) and (4.14) that

$$F = - \sum_{k_y} \sum_{s=\pm} \frac{1}{2} \varepsilon_s \Delta_0 \tanh(\frac{1}{2} \varepsilon_s \beta \Delta_0), \quad (4.22a)$$

$$\varepsilon_s = |\cos(\phi/2 + sLQ_z^+)|. \quad (4.22b)$$

The transverse momenta range over the interval $(-k_{\max}, k_{\max})$, with

$$k_{\max} = k_F \sqrt{\frac{1 - 2t_2}{1 - t_1^2 - 4t_2^2}}. \quad (4.23)$$

in view of Eq. (4.8). In a junction of width $W \gg L, \xi_0$, and at zero temperature, one has

$$I(\phi) = - \frac{e\Delta_0 W}{\hbar} \frac{1}{2\pi} \int_{-k_{\max}}^{k_{\max}} dk_y \frac{d}{d\phi} (\varepsilon_+ + \varepsilon_-). \quad (4.24)$$

The integral over k_y in Eq. (4.24) can be carried out in closed form for the case $t_2 = 0$ of a pure d_{xy} -wave magnetization, when $\varepsilon_s = |\cos(\phi/2 - st_1 k_y L)|$. We find

$$I = \frac{I_0}{2\alpha} \left(|\cos(\phi/2 - \alpha)| - |\cos(\phi/2 + \alpha)| \right), \quad (4.25)$$

with $I_0 = (e\Delta_0/\hbar)(k_{\max}W/\pi)$ and $\alpha = t_1 k_{\max}L$.

¹Our analysis applies to a symmetric Josephson junction, where the superconductors on both sides of the interface have the same gap Δ_0 . In a strongly asymmetric junction one would also need to include contributions to the supercurrent from the continuous spectrum, see L.-F. Chang and P. F. Bagwell, *Ballistic Josephson-current flow through an asymmetric superconductor-normal-metal-superconductor junction*, Phys. Rev. B **49**, 15853 (1994).

The critical current from Eq. (4.25) is given by

$$I_c = I_0 \frac{\sin 2\alpha}{2\alpha}, \quad (4.26)$$

see Fig. 4.6. A negative sign of I_c means that the maximum supercurrent is reached in the interval $-\pi < \phi < 0$. When $I_c < 0$ the Josephson energy is minimal at $\phi = \pi$ rather than at $\phi = 0$, the altermagnet Josephson junction has become a π -junction [8, 9].

With increasing L a negative critical current first appears in the interval $\pi/2 < t_1 k_{\max} L < \pi$. At $L = L^* \equiv 3\pi/(4t_1 k_{\max})$ one has $I_c = -(2/3\pi)I_0$, so the negative I_c is comparable in magnitude to the value I_0 at $L = 0$. Note that this characteristic length L^* is still in the short-junction regime provided that t_1 is not too small, we need $\Delta_0/\mu \ll t_1 \ll 1$.

These results are not changed qualitatively if we include a $d_{x^2-y^2}$ contribution to the magnetization, see Fig. 4.7. In the case $t_1 = 0$ of a pure $d_{x^2-y^2}$ -wave magnetization the negative critical current first appears in the interval $\pi/2 < \tilde{t}_2 k_{\max} L < \pi$, with

$$\tilde{t}_2 = \frac{1}{2}(1 - 2t_2)^{-1/2} - \frac{1}{2}(1 + 2t_2)^{-1/2} = t_2 + \mathcal{O}(t_2^2). \quad (4.27)$$

All of this was without normal reflections. We consider the effect of a tunnel barrier (transmission probability Γ) at each AS interface in the case of pure d_{xy} -wave magnetization, when we have the closed-form expression (4.18) for the Andreev levels. As illustrated in Fig. 4.8, the barrier reduces the magnitude of the critical current, but its sign remains unchanged. For $\Gamma \ll 1$ the critical current (4.26) is reduced by a factor Γ , because only the transmission resonance peaks (unit height, width Γ) contribute.

We can compare our analytical result (4.25) for the supercurrent-phase relationship with Ref. [8], which studies the same system in a different formulation. (The numerical study of Ref. [9] does not contain results that can be directly compared with ours.) While qualitatively we find the same sign changes in the critical current with increasing L , the decay rate of the oscillations is different in Ref. [8]: $I_c \propto L^{-3/2}$ instead of the $1/L$ decay in Eq. (4.26). Moreover, Eq. (4.25) is strongly nonsinusoidal, while Ref. [8] finds $I(\phi) \propto \sin \phi$. The absence of higher harmonics suggests a perturbative approximation ($\Gamma \ll 1$). We emphasise that our result is fully non-perturbative.

4.7 Conclusion

In summary, we have extended the scattering theory of nonmagnetic Josephson junctions to the case of an altermagnetic junction. The basic effect of the d -wave magnetization is to spin-polarize the Andreev levels, by giving the spin-up and spin-down spectra $E(\phi)$ opposite phase shifts $\pm\delta\phi$.

For a planar junction aligned along the crystalline axes of d_{xy} -wave symmetry the phase shift is proportional to the transverse momentum k_y , which upon integration of $dE/d\phi$ over k_y gives the simple closed-form result (4.25) for the supercurrent.

As noticed previously [8, 9], the altermagnet Josephson junction undergoes 0 – π transitions with increasing junction length L , where the critical current changes sign. Our approach is non-perturbative in the transmission probability through the junction, producing the strongly non-sinusoidal current-phase relationship of Figs. 4.6 and 4.7. To observe this the junction length L should be below the superconducting coherence length ξ_0 and also below the mean free path l for impurity scattering. The characteristic value of L for a negative critical current is $3\pi/(4t_1 k_F)$, which for $t_1 \simeq 0.1$ and $k_F \simeq 10^9 \text{ m}^{-1}$ amounts to a realistically short junction length of $L \simeq 20 \text{ nm}$.

4.8 Appendix: Scattering matrix calculation of the Andreev levels

We consider the altermagnet Josephson junction of Fig. 4.1, with a tunnel barrier (transmission probability Γ) at $x = 0$ and $x = L$. We calculate the Andreev level spectrum by means of the scattering formulation of Ref. [161].

The scattering matrix $S(E)$ of electrons (e) and holes (h) at energy E , incident on the altermagnet from the left (L) or the right (R) with transverse momentum k_y , has the block-diagonal form

$$S(E) = \begin{pmatrix} S_e(E) & 0 \\ 0 & S_h(E) \end{pmatrix}, \quad (4.28)$$

$$\Psi_{\text{out}} = S\Psi_{\text{in}}, \quad \Psi = (\psi_{e,L}, \psi_{e,R}, \psi_{h,L}, \psi_{h,R}).$$

Without the tunnel barrier and at the Fermi level ($E = 0$) one would have

simply

$$S_e(0) = \begin{pmatrix} 0 & \exp(-iL[Q_0^- + Q_z^-]) \\ \exp(iL[Q_0^+ + Q_z^+]) & 0 \end{pmatrix}, \quad (4.29a)$$

$$S_h(0) = \begin{pmatrix} 0 & \exp(-iL[Q_0^+ - Q_z^+]) \\ \exp(iL[Q_0^- - Q_z^-]) & 0 \end{pmatrix}, \quad (4.29b)$$

in terms of the momentum offsets defined in Eq. (4.10).

Multiple reflections by the two barriers change this into

$$S_e(0) = \frac{1}{1 + (1 - \Gamma)e^{iLK_e}} \begin{pmatrix} \sqrt{1 - \Gamma}(1 + e^{iLK_e}) & \Gamma \exp(-iL[Q_0^- + Q_z^-]) \\ \Gamma \exp(iL[Q_0^+ + Q_z^+]) & -\sqrt{1 - \Gamma}(1 + e^{iLK_e}) \end{pmatrix}, \quad (4.30a)$$

$$K_e = Q_0^+ - Q_0^- + Q_z^+ - Q_z^-, \quad (4.30b)$$

$$S_h(0) = \frac{1}{1 + (1 - \Gamma)e^{iLK_h}} \begin{pmatrix} \sqrt{1 - \Gamma}(1 + e^{iLK_h}) & \Gamma \exp(-iL[Q_0^+ - Q_z^+]) \\ \Gamma \exp(iL[Q_0^- - Q_z^-]) & -\sqrt{1 - \Gamma}(1 + e^{iLK_h}) \end{pmatrix}, \quad (4.30c)$$

$$K_h = -Q_0^+ + Q_0^- + Q_z^+ - Q_z^-. \quad (4.30d)$$

We set $\Delta = \Delta_0 e^{i\phi/2}$ at the left superconductor ($x < 0$) and $\Delta = \Delta_0 e^{-i\phi/2}$ at the right superconductor ($x > L$). The condition for a bound state is

$$\text{Det}[1 - R(E)S(E)] = 0, \quad (4.31)$$

in terms of the scattering matrix $S(E)$ of the normal region and the Andreev reflection matrix

$$R(E) = e^{-i\alpha(E)} \begin{pmatrix} 0 & R_{eh} \\ R_{he} & 0 \end{pmatrix}, \quad (4.32)$$

$$R_{eh} = R_{he}^* = \begin{pmatrix} e^{i\phi/2} & 0 \\ 0 & e^{-i\phi/2} \end{pmatrix}.$$

The function $\alpha(E)$, given by Eq. (4.11), varies on the scale of Δ_0 . The energy scale on which $S(E)$ varies is of order $\Gamma\bar{v}/L$. If $L \ll \Gamma\bar{v}/\Delta_0$ it is consistent to evaluate $S(E)$ at $E = 0$, while retaining the energy dependence of $R(E)$.

Substitution of Eqs. (4.30) and (4.32) into Eq. (4.31) gives the determinantal equation (4.19) from the main text.

4.9 Appendix: Tight-binding calculations

For the computer simulations we discretized the altermagnet Hamiltonian (4.3) on a square lattice (lattice constant a , mass m , and \hbar all set to unity),

$$H_0 = 2 - \cos k_x - \cos k_y - \mu + t_1 \sin k_x \sin k_y \sigma_z + 2t_2 (\cos k_x - \cos k_y) \sigma_z. \quad (4.33)$$

In the two superconducting regions we set $t_1 = 0 = t_2$ and couple the electron and hole blocks by a pair potential $\Delta_0 e^{\pm i\phi/2}$. We keep the same chemical potential μ throughout.

The system is infinitely extended in the y -direction. In the x -direction the altermagnet is in the interval $0 < x < L$, while the superconductors occupy the regions $-L_S < x < 0$ and $L < x < L_S$. The length L_S is chosen much larger than the superconducting coherence length $\xi_0 = \sqrt{2\mu}/\Delta_0$. We took $\mu = 0.5$ and $\Delta_0 = 5 \cdot 10^{-4}$, hence $\xi_0 = 2000$. With $L = 20$ we are therefore deep in the short-junction regime. The tight-binding model is implemented by means of the Kwant toolbox [163].

For Fig. 4.5 we inserted a tunnel barrier at $x = 0$ and $x = L$, by locally modifying the hopping matrix elements. The transmission probability T through the junction was calculated separately for $\Delta_0 = 0$, so that there are no adjustable parameters in the comparison with the analytics.

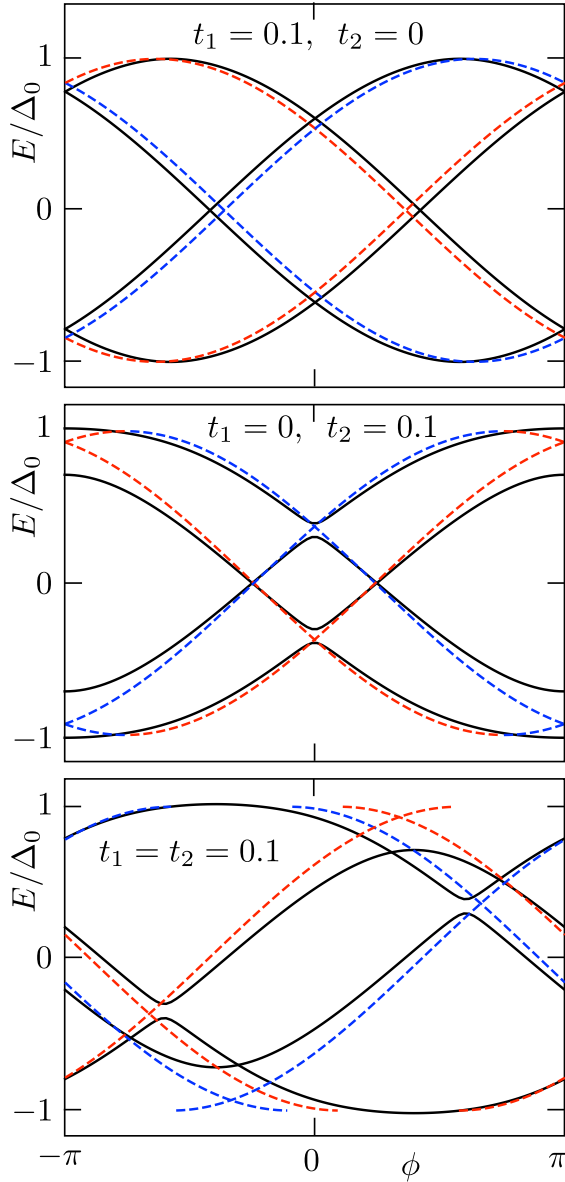


Figure 4.4. Andreev level spectra in the altermagnet Josephson junction, for $k_{\text{F}}L = 20$, $k_y/k_{\text{F}} = 1/2$, and different choices of t_1, t_2 . The solid curves result from the numerical solution of the BdG equation on a lattice. The dashed curves are the analytical predictions (4.13), in which normal reflections at the AS interfaces are neglected (blue for spin-up, red for spin-down).

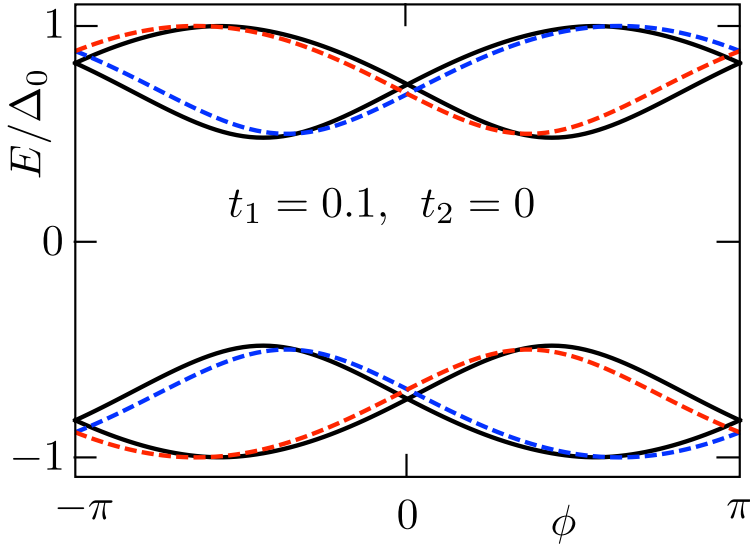


Figure 4.5. Solid curves: Andreev levels for d_{xy} -wave pairing in the presence of a tunnel barrier at the two AS interfaces ($k_{\text{F}}L = 20$, $k_y/k_{\text{F}} = 1/2$). The normal-state transmission probability $T = 0.75$ through the junction was obtained directly from the computer simulation (by setting $\Delta_0 \equiv 0$). The dashed curves are the analytical prediction (4.18), for the same value of T (blue for spin-up, red for spin-down).

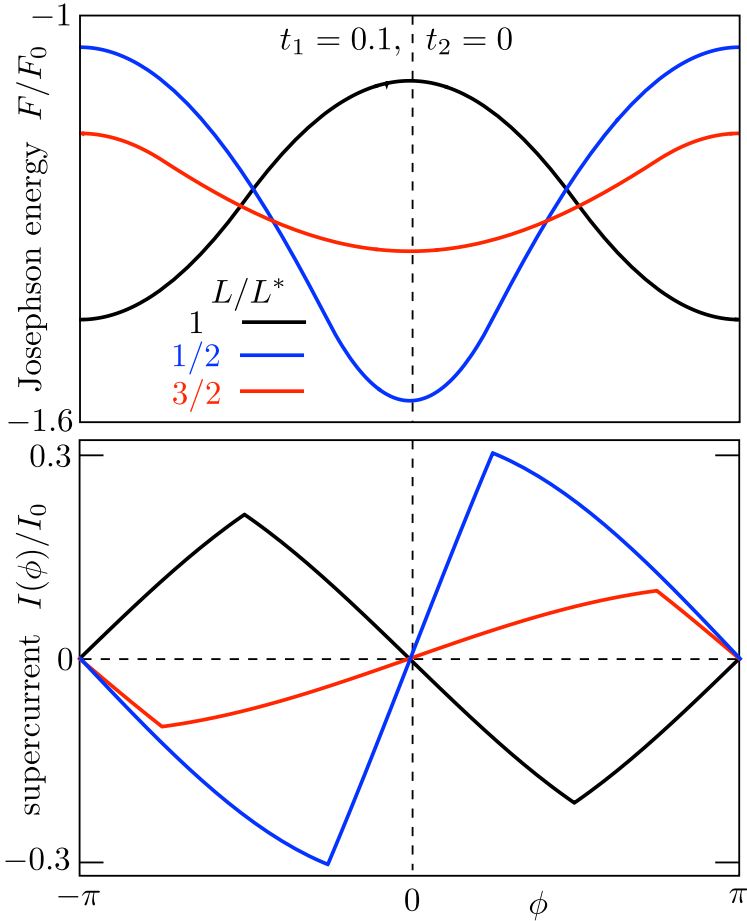


Figure 4.6. Phase dependence of the Josephson energy (top panel, in units of $F_0 = \Delta_0 k_{\max} W / \pi$) and the supercurrent (lower panel, in units of $I_0 = (e/\hbar)F_0$) in the altermagnet Josephson junction, for different lengths L of the junction [in units of $L^* = 3\pi / (4t_1 k_{\max})$]. In the interval $2/3 < L/L^* < 4/3$ the Josephson energy is maximal rather than minimal at $\phi = 0$, resulting in a negative critical current. These are results for pure d_{xy} -wave magnetization ($t_2 = 0$) and without normal reflection ($\Gamma = 1$).

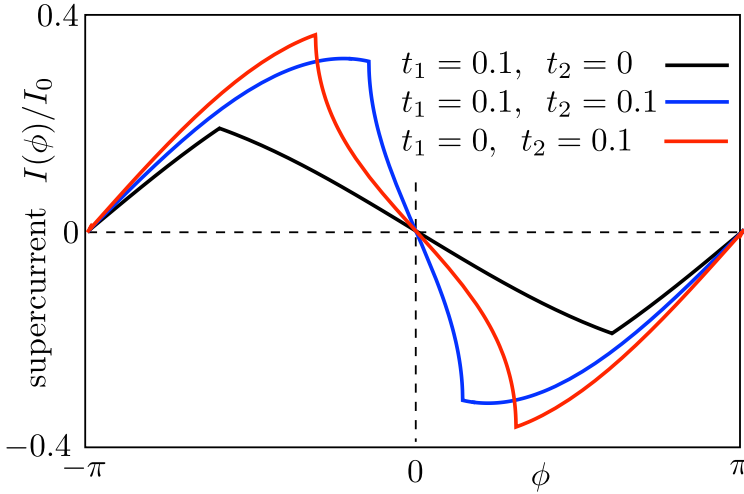


Figure 4.7. Current-phase relationship for the case of pure d_{xy} -wave magnetization (black, $t_2 = 0, t_1 = 0.1, k_F L = 25$), pure $d_{x^2-y^2}$ -wave magnetization (red, $t_1 = 0, t_2 = 0.1, k_F L = 20$) and the equal weight case (blue, $t_1 = t_2 = 0.1, k_F L = 15$).

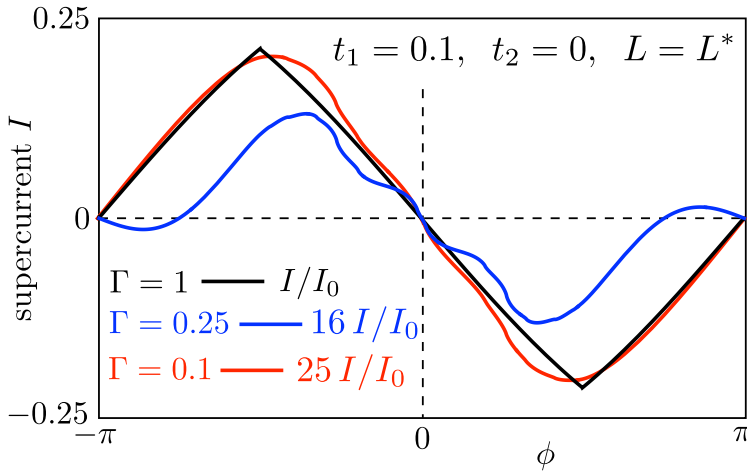


Figure 4.8. The black curve shows the supercurrent (4.25) without normal reflections, the blue and red curves include normal reflections from a barrier at each AS interface [transmission probability Γ , Andreev levels given by Eqs. (4.18) and (4.20)]. Each curve is for the same junction length $L = L^*$ and d_{xy} magnetization strength $t_1 = 0.1$ (with $t_2 = 0$).

Chapter 5

Bloch oscillations in the magnetoconductance of twisted bilayer graphene

5.1 Introduction

It is one of the early counterintuitive predictions of solid state physics that an electric field in a crystal induces an *oscillatory* electron motion [52, 53]¹: While the momentum $\hbar k$ increases linearly with time, according to $\hbar k(t) = e\mathcal{E}t$ in an electric field \mathcal{E} , the corresponding velocity $v(t) \propto \sin k(t)$ in a Bloch band (unit lattice constant) has a periodic time dependence, with frequency $\omega_B = e\mathcal{E}/\hbar$. The amplitude $\mathcal{A} \approx \Delta/e\mathcal{E}$ of the Bloch oscillations is set by the energy band width Δ .

Electronic Bloch oscillations have been studied in the time domain at THz frequencies in semiconductor superlattices [54–57, 164, 165] and in graphene bilayers [58]. With few exceptions [166], and unlike the familiar Aharonov-Bohm oscillations [167], Bloch oscillations do not typically play a role in quantum transport, which is probed in the energy domain at low frequencies. Here we show that Bloch oscillations may appear in the magnetoconductance of a two-dimensional (2D) system, a twisted graphene bilayer, by virtue of a mapping to a quantum walk in one space and one time dimension.

¹Historical note: The oscillatory motion follows from equation 48 in Bloch's 1929 paper [52], but this was not noticed until Zener pointed it out in 1934 [53]. See <https://hsm.stackexchange.com/q/14442/1697>

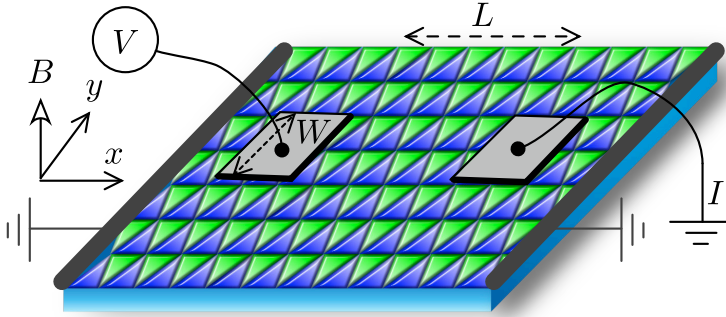


Figure 5.1. Moiré lattice in a twisted graphene bilayer. Triangular domains of AB and BA stacking are indicated by different colors. Domain walls conduct a current $I = VG$ between narrow source and drain contacts (width W , a distance L apart). This is a four-terminal geometry, including two additional wide grounded contacts at the left and right.

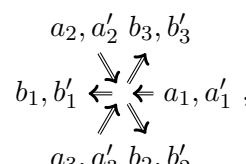
The magnetic field B perpendicular to the bilayer maps onto a parallel electric field $\mathcal{E} \leftrightarrow Bv/2$, with v the Fermi velocity. As a consequence, the conductance measured between two point contacts at a distance L oscillates periodically in B . These Bloch magnetoconductance oscillations appear at much weaker fields, smaller by a factor L over lattice constant, than the known Aharonov-Bohm oscillations in twisted bilayer graphene [50, 51, 168, 169].

5.2 Network model

We start from the established network model of minimally twisted bilayer graphene [41–43, 48, 49, 81, 82]: Two layers of graphene are misaligned by a rotation angle $\theta \approx 0.1^\circ$, forming a moiré pattern of triangular domains with different stacking (AB versus BA) of the carbon atoms on the A and B sublattices of the two layers. (See Fig. 5.1.) An interlayer bias voltage gaps out the interior of the AB and BA domains, leaving a conducting network formed by AB/BA domain walls that meet at angles of 60° on a metallic node. The lattice constant $a = a_0[2\sin(\theta/2)]^{-1}$ of the moiré pattern is of the order of 100 nm, two orders of magnitude larger than the atomic lattice constant a_0 of graphene.

The direction of motion along a domain wall is tied to the valley degree of freedom. (The spin degree of freedom is decoupled from the motion

and plays no role in what follows.) In a single valley each domain wall supports two modes, both of the same chirality (propagating in the same direction with velocity v). Neglecting intervalley scattering (justified for $a \gg a_0$ with smooth disorder, and experimentally verified [48]) the scattering process at a node thus involves 6 incoming and 6 outgoing mode amplitudes, related by a scattering matrix S of the form [41, 168]:

$$S \cdot \{a_1, a_2, a_3, a'_1, a'_2, a'_3\}^\top = \{b_1, b_2, b_3, b'_1, b'_2, b'_3\}^\top,$$


$$S = \begin{pmatrix} S_1 & S_2 \\ S_2^\dagger & -S_1^\dagger \end{pmatrix}, \quad (5.1a)$$

$$S_1 = e^{i\alpha} \sqrt{P_{d1}} \begin{pmatrix} 0 & 1 & 1 \\ 1 & 0 & 1 \\ 1 & 1 & 0 \end{pmatrix} + e^{i\beta} \mathbb{1} \sqrt{P_{f1}}, \quad (5.1b)$$

$$S_2 = \sqrt{P_{d2}} \begin{pmatrix} 0 & 1 & -1 \\ -1 & 0 & 1 \\ 1 & -1 & 0 \end{pmatrix} - \mathbb{1} \sqrt{P_{f2}}. \quad (5.1c)$$

The 3×3 submatrices S_1 and S_2 describe intramode and intermode scattering, respectively. Forward scattering happens with probability $P_f = P_{f1} + P_{f2}$, scattering with a $\pm 120^\circ$ deflection happens with probability $P_d = P_{d1} + P_{d2}$. Unitarity of S requires that

$$P_{f1} + P_{f2} + 2P_{d1} + 2P_{d2} = 1, \quad (5.2)$$

$$\cos(\beta - \alpha) = \frac{1}{2}(P_{d2} - P_{d1})(P_{f1}P_{d1})^{-1/2} \in [-1, 1].$$

To reduce the number of free parameters, we take equal intra-channel and inter-channel probabilities: $P_{f1} = P_{f2} = \frac{1}{2}P_f$ and $P_{d1} = P_{d2} = \frac{1}{4}(1 - P_f)$. Then $\beta = \alpha + \pi/2$ and we are left with the two parameters $P_f \in [0, 1]$ and $\alpha \in [0, \pi/2]$. The parameter α governs the appearance of closed loops of scattering sequences [168]. At $\alpha = 0$, the network does not support closed loops (quasi-1D transport), while for $\alpha = \pi/2$ closed loops dominate (2D transport).

The propagation between two nodes along a domain wall introduces a phase factor $e^{iEa/\hbar v}$, at energy E . The scattering matrix (5.1) of the nodes is assumed to be energy independent, so the scattering sequences consist of instantaneous nodal scattering events, spaced by the constant time a/v . A stroboscopic (Floquet) description of the scattering is then appropriate [170, 171]. In the quasi-1D regime this corresponds to a quantum walk.

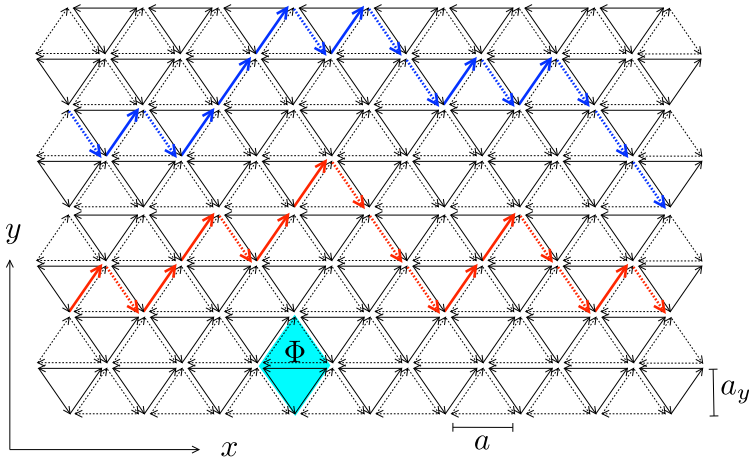


Figure 5.2. Network of domain walls with two realizations of the quantum walk in a single valley (blue and red arrows). Even and odd parity chiral modes are indicated by solid and dashed lines. Forward scattering at a node preserves the parity, while a deflection switches the parity. The quantum walk propagates along the y -axis with step size $a_y = \frac{1}{2}\sqrt{3}a$, the x -axis playing the role of time ($t \leftrightarrow 2x/v$). The unit cell of the lattice, of area aa_y and enclosing a flux Φ , is indicated in blue.

5.3 Quantum walk

Two scattering sequences in the quasi-1D regime ($\alpha = 0$) are shown in Fig. 5.2. The solid and dashed lines distinguish even and odd parity modes in a given valley, both propagating in the same direction. (The counterpropagating modes are in the other valley.) We can interpret a scattering sequence as a quantum walk [172], with time step $t_0 = a/v$. There are six independent quantum walks, rotated relative to each other by 60° , three in one valley and three in the other valley. We focus on one of these.

At each step the x -coordinate is increased by $a/2$. The y -coordinate changes by $\pm \frac{1}{2}a\sqrt{3} \equiv \pm a_y$, the even parity mode moves up and the odd parity mode moves down. The wave amplitudes $\psi = (\psi_+, \psi_-)$ of the even and odd parity states form a pseudospin degree of freedom, which is

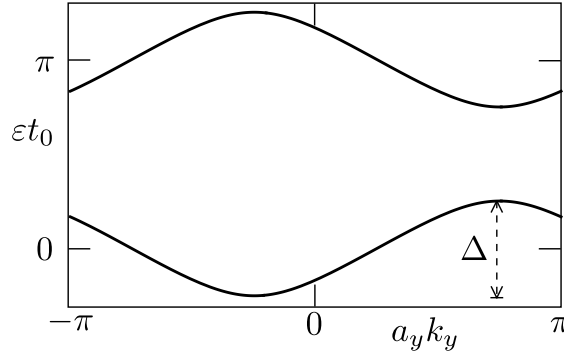


Figure 5.3. Two Bloch bands $\varepsilon_{\pm}(k_y)$ of the quantum walk, computed from Eq. (5.5) for $P_f = 1/2$. The band width Δ is indicated.

rotated at each node by the 2×2 matrix [168]²

$$R = \begin{pmatrix} e^{i\pi/4} \sqrt{P_f} & \sqrt{1-P_f} \\ \sqrt{1-P_f} & -e^{-i\pi/4} \sqrt{P_f} \end{pmatrix}. \quad (5.3)$$

The corresponding time evolution of a state (at stroboscopic intervals $t = 0, 1, 2, \dots \times t_0$) is given by

$$\psi_{t+t_0} = \mathcal{T}R\psi_t, \quad (5.4)$$

$$\mathcal{T}\psi(y) = (\psi_+(y - a_y), \psi_-(y + a_y)) = e^{-ia_y \hat{k}_y \sigma_z} \psi(y).$$

The operator \mathcal{T} displaces the particle up or down depending on its pseudospin σ_z . Eq. (5.4) represents a 1D quantum walk along y in the fictitious time $t = 2x/v$, with momentum operator $\hat{k}_y = -i\partial/\partial y$.

The eigenvalues $e^{-i\varepsilon t_0}$ of the evolution operator $\mathcal{T}R$ in momentum representation are given by

$$\varepsilon_{\pm} t_0 = \pm \arccos[\sqrt{P_f} \sin(a_y k_y - \pi/4)] + \pi/2, \quad (5.5)$$

plotted in Fig. 5.3. The single-valley bandstructure of the quasi-1D regime [41] is given by three copies rotated by 120° of the dispersion relation

$$E_{\pm}^{(n)}(k_x, k_y) = \hbar \varepsilon_{\pm}(k_y) + 2\pi n \hbar / t_0 + \hbar v k_x / 2, \quad n \in \mathbb{Z}. \quad (5.6)$$

²The unitary transformation $S \mapsto USU^\dagger$ that decouples the 6×6 scattering matrix (5.1) into 2×2 submatrices is $U = e^{-i(\pi/4)\sigma_y} e^{i(\alpha/2)\sigma_z}$. The Pauli matrices act on the two modes in each domain wall. The decoupling needs $\alpha = 0$ and $P_{d1} = P_{d2}$; if $P_{f1} \neq P_{f2}$ the phase $\pi/4$ in Eq. (5.3) is replaced by $\arctan \sqrt{P_{f1}/P_{f2}}$.

5.4 Bloch oscillations

A perpendicular magnetic field $\mathbf{B} = \nabla \times \mathbf{A}$ (in the z -direction) introduces a phase shift $-e \int \mathbf{A} \cdot d\mathbf{l}$ at each time step (taking the electron charge as $+e$). For $\mathbf{A} = (-By, Ba/4, 0)$ the time evolution (5.4) is modified into ³

$$\psi_{t+t_0} = e^{i\phi\hat{y}/a_y} \mathcal{T} R \psi_t, \quad \phi = \pi\Phi/\Phi_0. \quad (5.7)$$

The operator \hat{y} is defined by $\hat{y}\psi_t(y) = y\psi_t(y)$. The flux $\Phi = Ba a_y$ is the flux through a unit cell (two domain wall triangles) and $\Phi_0 = h/e$ is the flux quantum. The same phase shift ϕ would be produced by a fictitious electric field $\mathcal{E} \equiv Bv/2$. The corresponding Bloch frequency is

$$\omega_B = a_y e \mathcal{E} / \hbar = \phi / t_0. \quad (5.8)$$

Since the width of the Bloch band (5.5) is $\Delta = (2\hbar/t_0) \arcsin \sqrt{P_f}$, the amplitude of the Bloch oscillations is

$$\mathcal{A} \approx \Delta / e \mathcal{E} = (2a_y / \phi) \arcsin \sqrt{P_f}. \quad (5.9)$$

The 1D quantum walk in an electric field has been analyzed theoretically [59, 173–175] and realized experimentally in the context of optics [176, 177] and atomic physics [178]. A spatially localized wave packet evolves in a characteristic “breathing mode” with envelope [59] $\pm \mathcal{A} \sin(\omega_B t / 2)$. In our case, where time $t \mapsto 2x/v$ maps onto space, this implies the envelope

$$y_{\text{envelope}}(x) = \pm (2a_y / \phi) \arcsin \sqrt{P_f} \times \sin(\phi x / a). \quad (5.10)$$

A numerical simulation of the network model shown in Fig. 5.4 agrees nicely with this breathing mode envelope. For nonzero α side branches appear at a 120° orientation with the breathing mode, which we explain in terms of magnetic breakdown.

5.5 Magnetic breakdown

In semiclassical approximation the motion of an electron in a magnetic field \mathbf{B} can be obtained from the equi-energy contours in zero field: Because $\hbar \dot{\mathbf{k}} = e \dot{\mathbf{r}} \times \mathbf{B}$, the real-space orbit of a wave packet at energy E

³The constant y -component of the vector potential $\mathbf{A} = (-By, Ba/4, 0)$ is chosen such the resulting phase shift does not depend on the parity of the chiral mode. We need this for the mapping to an electric field induced phase shift. All results are obviously gauge independent, but this gauge simplifies the analysis.

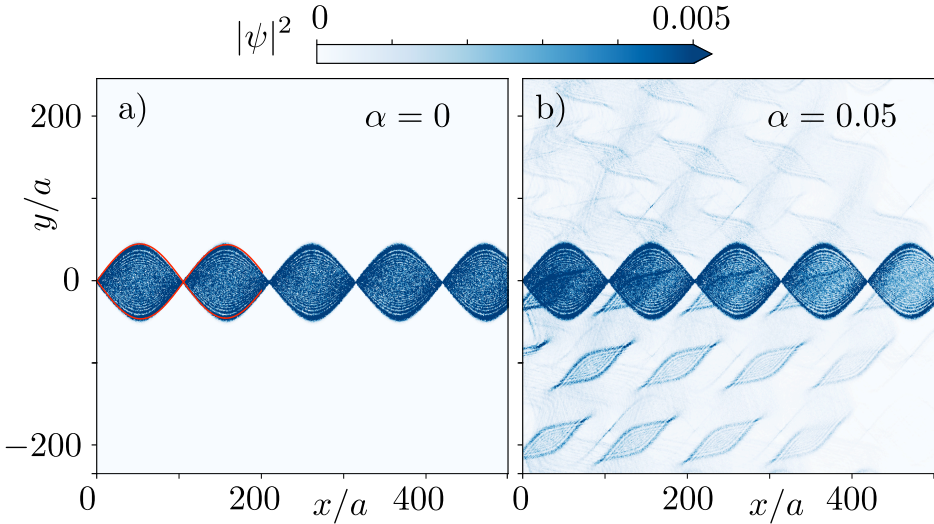


Figure 5.4. Numerical simulations of electron scattering in a twisted graphene bilayer, in a magnetic field ($\phi = \pi\Phi/\Phi_0 = 0.03$). Electrons at energy $E = 0$ are injected in a single mode and in a single node at $(x, y) = (0, 0)$. They then propagate through the network following the scattering matrix (5.1). We take $P_{f_1} = P_{f_2} = 1/4$, $P_{d1} = P_{d2} = 1/8$ and compare two values of α . The blue color scale gives the intensity $|\psi|^2$ of the scattering state. The red curve in panel a) is the envelope of the breathing mode predicted by Eq. (5.10).

follows the contour $E(\mathbf{k}) = E$ upon rotation by 90° and rescaling by a factor $l_m^2 = \hbar/eB$ (magnetic length squared).

We calculate the equi-energy contours⁴ from the scattering matrix (5.1), see Fig. 5.5. At $\alpha = 0$ three oscillating contours rotated by 120° cross near $\mathbf{k} = 0$. A wave packet moves along these open orbits with velocity $dk/dt = v/l_m^2$. A nonzero α opens up a gap $\Delta k \simeq \alpha/a$ at each crossing, thereby allowing the wave packet to be deflected by $\pm 120^\circ$. Magnetic breakdown refers to the tunneling of the wave packet through the gap [179, 180]. This happens with the Landau-Zener probability $T = \exp[-c(l_m\Delta k)^2]$, where c is a coefficient of order unity⁵. We conclude

⁴The bandstructure $E(\mathbf{k})$ of the infinite network, as a function of the Bloch momentum $\mathbf{k} = (k_x, k_y)$, is given by the eigenvalues $e^{iEa/\hbar v}$ of the matrix product $\Omega = S \cdot \text{diag}(e^{i\mathbf{k}\cdot\mathbf{l}_+}, e^{i\mathbf{k}\cdot\mathbf{l}_-}, e^{i\mathbf{k}\cdot\mathbf{l}_0}, e^{i\mathbf{k}\cdot\mathbf{l}_+}, e^{i\mathbf{k}\cdot\mathbf{l}_-}, e^{i\mathbf{k}\cdot\mathbf{l}_0})$, with lattice vectors $\mathbf{l}_\pm = \frac{1}{2}a(1, \pm\sqrt{3})$, $\mathbf{l}_0 = (-a, 0)$.

⁵The coefficient $c = \frac{1}{4}\pi \tan(\vartheta/2)$ in the magnetic breakdown probability $T = e^{-c(l_m\Delta k)^2}$ is determined by the angle $\vartheta \in (0, \pi)$ at which the equi-energy con-

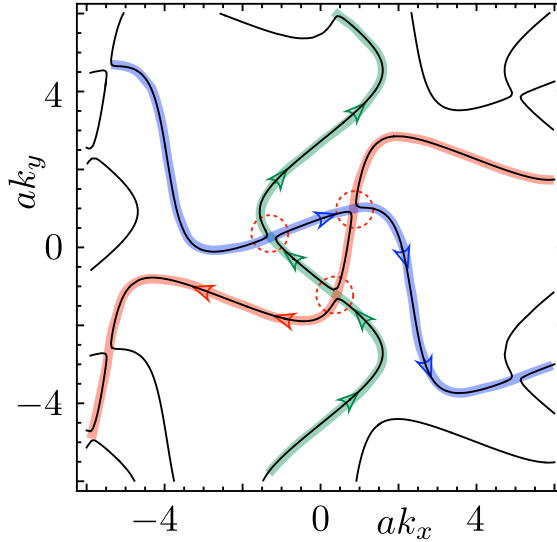


Figure 5.5. Equi-energy contours $E(k_x, k_y) = 0$ at zero magnetic field, computed for $P_{f_1} = P_{f_2} = 1/4$, $P_{d1} = P_{d2} = 1/8$, $\alpha = 0.1$. A magnetic field drives a wave packet in the direction of the arrows. Points of magnetic breakdown (tunneling between two contours) are encircled. The resulting open orbits are distinguished by different colors.

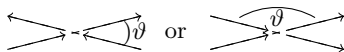
that the breathing mode remains predominantly uncoupled from the side branches provided that $(\alpha l_m/a)^2 \ll 1 \Rightarrow \alpha^2 \ll \Phi/\Phi_0$.

All of this is for the case of equal intra-channel and inter-channel probabilities. We have investigated numerically what happens if we relax this assumption. A difference between P_{d1} and P_{d2} increases the gap, $(a\Delta k)^2 \approx \alpha^2 + (P_{d1} - P_{d2})^2$. A difference between P_{f1} and P_{f2} has no effect on the gap, it weakly affects the coefficient c .

5.6 Conductance

The breathing mode visualized in Fig. 5.4 can be detected via the conductance, in the geometry of Fig. 5.1, with source and drain contacts aligned along a domain wall. We have tested this by computer simulation.

tours approach the avoided crossing, dependent on the relative direction of motion:



For typical parameters we have $\vartheta \approx 60^\circ \Rightarrow c \approx 0.45$.

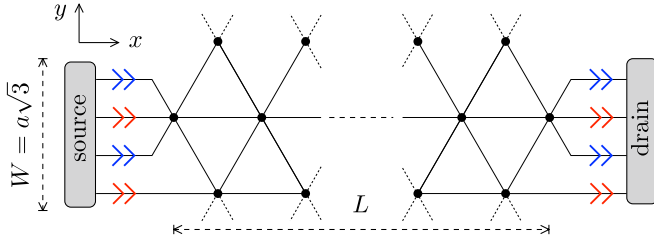


Figure 5.6. Outgoing modes at the left (source contact) and incoming modes at the right (drain contact). Red and blue arrows distinguish pairs of modes in the two valleys. For contacts of width $W = N \times a\sqrt{3}$ the transmission matrix t from source to drain has dimension $8N \times 8N$. The diagram shows the case $N = 1$. The full network in the simulation has length L along the x -axis and width much larger than the contact width W along the y -axis.

The transmission matrix t_{nm} from mode m in the source contact to mode n in the drain contact is calculated in the network model [41]. There are $8N$ outgoing (incoming) modes in the source (drain) contact, distributed over $N = W/a\sqrt{3}$ unit cells (see Fig. 5.6). Four of the eight modes per unit cell are in one valley and four are in the other valley.

The two-terminal conductance follows from

$$G = G_0 \sum_{n,m=1}^{8N} |t_{nm}|^2, \quad (5.11)$$

with $G_0 = 2e^2/h$ the conductance quantum (the factor of two accounts for the spin). In the quasi-1D regime only two of the eight modes per unit cell contribute to the conductance, corresponding to the breathing mode. Note that the current is highly valley polarized: the red modes in Fig. 5.6 give a negligible contribution to G , because they are backscattered into the source at the nodes. A rotation of the contact alignment by 60° switches the transmission from one valley to the other.

The conductance is a maximum whenever a node of the breathing mode coincides with the drain contact, so if the separation L of source and drain is an integer multiple of $\pi a/\phi = a\Phi_0/\Phi$. As a function of magnetic field the conductance then oscillates with period ⁶

$$\Delta\Phi = \Phi_0 \times a/L \Rightarrow \Delta B = (h/e)(a_y L)^{-1}. \quad (5.12)$$

⁶The periodicity (5.12) refers to the magnetoconductance oscillations from the breathing mode near $\Phi = 0$. Because of gauge invariance, copies exist near higher fields $\Phi_p = \Phi_0/p$ ($p = 1, 2, \dots$), with smaller periodicity $\Delta\Phi_p = (\Phi_0/p) \times a/L$.

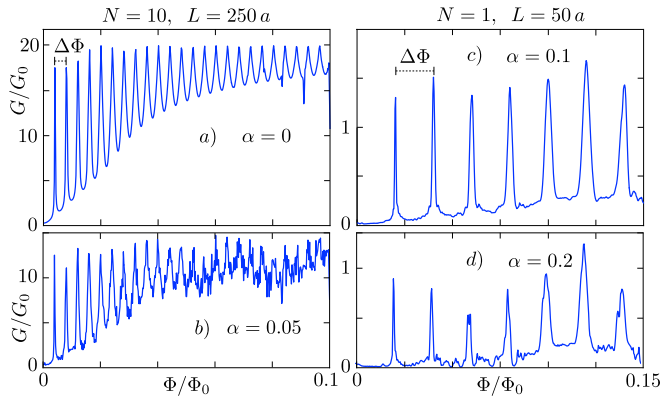


Figure 5.7. Calculation of the magnetic field dependence of the conductance in the geometry of Fig. 5.1. Source and drain contacts are separated by L and have a width of N unit cells ($W = N \times a\sqrt{3}$). The parameters of the network model are the same as in Fig. 5.4. Different values of α are compared, for wide contacts (panels a,b) and narrow contacts (panels c,d). The Bloch oscillation period $\Delta\Phi$ from Eq. (5.12) is indicated. Full transmission of the breathing mode corresponds to $G/G_0 = 2N$.

This is what we observe in the computer simulation [181], see Fig. 5.7. To resolve the Bloch oscillations the width W of source and drain contacts should be smaller than the amplitude $\mathcal{A} \propto 1/B$ of the breathing mode, which explains why the oscillations die out with increasing magnetic field. The oscillations become more robust to nonzero α if both the width and the separation of the contacts are reduced, because then the larger magnetic field scale promotes the magnetic breakdown that enables the breathing mode.

5.7 Conclusion

In closing, we have shown that the breathing mode that is the hallmark of Bloch oscillations in a periodic potential can be observed in the magneto-conductance of minimally twisted bilayer graphene. The spatial resolution that is needed to resolve the oscillatory electron motion requires narrow source and drain contacts, which is presumably why these low-field oscillations have not yet been observed. Panels c,d in Fig. 5.7 correspond to a contact width $W = a\sqrt{3} \approx 0.25 \mu\text{m}$ at a twist angle $\theta \approx 0.1^\circ$.

For a contact separation of $L = 50a \approx 7 \mu\text{m}$ the periodicity of the mag-

netoconductance oscillations is $\Delta B \approx 2.4$ mT. This is two orders of magnitude below the fields at which quantum Hall interferometry (Aharonov-Bohm and Shubnikov-De Haas oscillations) becomes operative [50, 51, 168, 169]. There is room to reduce the contact separation, which will help to mitigate disorder effects — L should be shorter than the mean free path.

The key requirement for the appearance of the breathing mode is the quasi-1D regime, in which open orbits govern the magnetoconductance, enabled by magnetic breakdown. Support for this regime can be found in microscopic calculations of the band structure [81], that show equi-energy contours qualitatively similar to those in Fig. 5.5. The observation of the low-field magnetoconductance oscillations predicted here would then be a striking demonstration of Bloch oscillations in the solid state.

Chapter 6

Breathing mode in open-orbit magnetotransport: a magnetic lens with a quantum mechanical focal length

6.1 Introduction

The Lorentz force from a magnetic field may act as a lens for electrons, by focusing their trajectories down to a point of size limited only by their wave length. In the solid state such electron optics was pioneered half a century ago by Sharvin and Tsoi [182–184], enabled by the availability of single crystals with mean free paths of several millimeters — well above the typical focal lengths of the magnetic lens. Geometric optics is sufficient in metals [185, 186], in semiconductors and in graphene the larger wave length introduces diffraction and interference effects [187–190]. Irrespective of these quantum effects, the magnetic focusing itself is still an essentially classical effect — the focal length is given by the classical cyclotron radius p_F/eB (ratio of Fermi momentum and magnetic field). In what follows we will describe a magnetic focusing effect that is intrinsically

quantum mechanical. The focusing mechanism is Bragg reflection at Brillouin zone boundaries, resulting in a parametrically larger focal length, with Fermi momentum p_F replaced by the Bragg momentum transfer \hbar/a (inverse lattice constant).

We build on our recent study of magnetotransport in twisted bilayer graphene [191], where a precise mathematical mapping was found onto Bloch oscillations in an electric quantum walk [173–175]. The mapping of space onto time and magnetic field onto electric field was shown to result in a “breathing mode” [59, 165], a wave function that periodically expands and contracts. The mapping relied on the special nature of the scattering problem in the graphene bilayer [168], where electrons propagate in topologically protected chiral modes on a triangular network of domain walls [42, 43].

Here we take a broader perspective and develop a general theory for breathing modes that applies to any band structure which supports open orbits in a magnetic field. It applies in particular to layered materials with a strongly anisotropic dispersion, of recent interest in this context [166, 192]. We present both a fully quantum mechanical calculation and a semiclassical description of the breathing mode, and test this by comparing with computer simulations of a tight-binding model.

6.2 Calculation of the breathing mode

An open orbit in the Brillouin zone is an equi-energy contour that crosses the Brillouin zone boundaries. In the repeated zone scheme it therefore runs through the whole reciprocal space, without closing on itself. The open orbits in a plane perpendicular to an applied magnetic field govern the electrical transport properties. We orient the field in the z -direction and focus on an open orbit in the x - y plane. An example on the 2D square lattice is shown in Fig. 6.1.

As an effective low-energy description of an open orbit we consider a two-dimensional (2D) Bloch band near the Fermi energy $E_F = 0$ in the first Brillouin zone, described by the Hamiltonian

$$H = \hbar v_x k_x + \varepsilon(k_y). \quad (6.1)$$

The momentum operator is $\mathbf{k} = -i\partial/\partial\mathbf{r}$. The open orbit has the equi-energy contour $\varepsilon(k_y) + \hbar v_x k_x = 0$, with $\varepsilon(k_y) = \varepsilon(k_y + 2\pi/a_y)$ for lattice constant a_y .

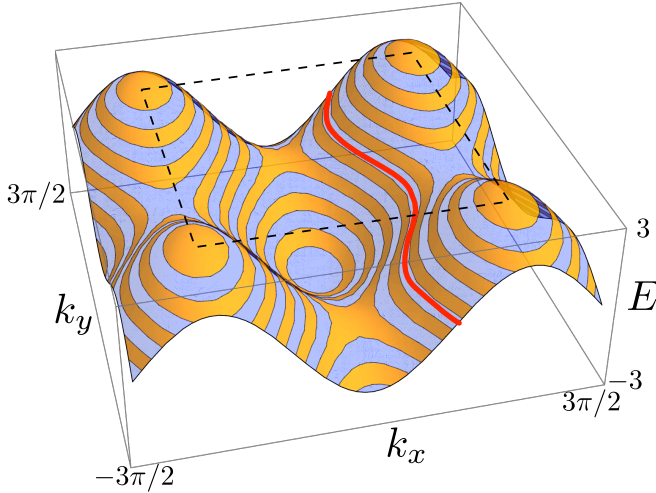


Figure 6.1. Equi-energy contours of the 2D dispersion $E(k_x, k_y) = -2 \cos k_x - \cos k_y$ (dimensionless units). The black dotted square indicates the Brillouin zone, the red curve is an open orbit at the Fermi energy $E_F = 0$, given by $k_x + \varepsilon(k_y) = 0$, with $\varepsilon(k_y) = -\arccos(-\frac{1}{2} \cos k_y)$.

The vector potential is introduced via the substitution $\hbar\mathbf{k} \mapsto \hbar\mathbf{k} - e\mathbf{A}$ (taking the electron charge as $+e$). We choose the gauge $\mathbf{A} = (-yB(x), 0, 0)$, corresponding to the magnetic field $\mathbf{B} = (0, 0, B(x))$. We will later specialize to the case $B(x) = B_0$ of a constant field.

Eigenstates $\Psi(x, k_y)$ of H at energy $E = 0$, in a mixed coordinate-momentum representation, satisfy

$$iv_x(-\hbar\partial_x + eB(x)\partial_{k_y})\Psi(x, k_y) = -\varepsilon(k_y)\Psi(x, k_y). \quad (6.2)$$

A similar partial differential equation has been studied in the context of Wannier-Stark localization [193], and we can adapt that method of solution.

We define the field integral

$$C(x) = \int_0^x B(x') dx', \quad (6.3)$$

and note that

$$\hbar\partial_x f(\hbar k_y + eC(x)) = eB(x)\partial_{k_y} f(\hbar k_y + eC(x)), \quad (6.4)$$

for any function f . We thus find the solution

$$\Psi(x, k_y) = \Psi(0, k_y + (e/\hbar)C(x)) \exp(-i\omega(x, k_y)), \quad (6.5)$$

$$\omega(x, k_y) = \int_0^x \frac{dx'}{\hbar v_x} \varepsilon(k_y + (e/\hbar)C(x) - (e/\hbar)C(x')). \quad (6.6)$$

For an initial condition $\Psi(0, k_y) \equiv 1$ that is localized at $y = 0$ we obtain the real space profile

$$\psi(x, y) = a_y \int_0^{2\pi/a_y} \frac{dk_y}{2\pi} e^{iyk_y} \exp(-i\omega(x, k_y)). \quad (6.7)$$

The first moment of the transverse displacement vanishes,

$$\begin{aligned} \langle y \rangle_x &= a_y \sum_{m=-\infty}^{\infty} m |\psi(x, ma_y)|^2 \\ &= ia_y \int_0^{2\pi/a_y} \frac{dk_y}{2\pi} \Psi^*(x, k_y) \partial_{k_y} \Psi(x, k_y) \\ &= a_y \int_0^{2\pi/a_y} \frac{dk_y}{2\pi} \partial_{k_y} \omega(x, k_y) = 0. \end{aligned} \quad (6.8)$$

The second moment is given by

$$\begin{aligned} \langle y^2 \rangle_x &= a_y^2 \sum_{m=-\infty}^{\infty} m^2 |\psi(x, ma_y)|^2 \\ &= a_y \int_0^{2\pi/a_y} \frac{dk_y}{2\pi} |\partial_{k_y} \Psi(x, k_y)|^2 \\ &= a_y \int_0^{2\pi/a_y} \frac{dk_y}{2\pi} \left(\partial_{k_y} \omega(x, k_y) \right)^2. \end{aligned} \quad (6.9)$$

Specializing now to a constant magnetic field, we have $C(x) = B_0 x$ and

$$\omega(x, k_y) = (eB_0 v_x)^{-1} \int_{k_y}^{k_y + eB_0 x/\hbar} dq \varepsilon(q). \quad (6.10)$$

We conclude that

$$\psi(x + 2\pi\hbar/eB_0 a_y, y) = \psi(x, y) e^{-i\alpha}, \quad (6.11)$$

for some constant phase α , so the density $|\psi(x, y)|^2$ is periodic in x with period

$$\ell = \frac{h}{eB_0 a_y} = \frac{a_x \Phi_0}{\Phi}. \quad (6.12)$$

Here $\Phi = Ba_x a_y$ is the flux through a unit cell and $\Phi_0 = h/e$ is the flux quantum.

The transverse displacement has variance

$$\langle y^2 \rangle_x = \frac{a_y}{(eB_0 v_x)^2} \int_0^{2\pi/a_y} \frac{dk_y}{2\pi} (\varepsilon(k_y + eB_0 x) - \varepsilon(k_y))^2, \quad (6.13)$$

which vanishes when $x = n\ell$, $n = 1, 2, \dots$ — the breathing mode refocuses to a single lattice site.

6.3 Tight-binding model

We test this analytical theory numerically on the tight-binding model of a 2D square lattice (lattice constant $a_x = a_y = a$) with anisotropic nearest-neighbor hopping energies t_x and t_y in the x - and y -directions. In the plots we take $t_y/t_x \equiv \tau = 1/2$. The Hamiltonian is

$$\mathcal{H} = -t_x \cos a_x k_x - t_y \cos a_y k_y. \quad (6.14)$$

We set the Fermi level in the middle of the band, $E_F = 0$, where the open orbits are given by

$$a_x k_x = \pm \arccos(-\tau \cos a_y k_y) + 2\pi n, \quad n \in \mathbb{Z}, \quad (6.15)$$

see Fig. 6.1.

The geometry is shown in Fig. 6.2. The conductor has dimensions L in the x -direction and W in the y -direction. Point contacts (width δW) at $x = 0$ and $x = L$ are a source and drain for electrical current. We implement hard-wall boundary conditions at $|y| = W/2$ (by terminating the lattice) and absorbing boundary conditions at $x = 0, L$, $|y| > \delta W/2$ (by attaching ideal leads to ground). The grounded leads are not essential for the magnetoconductance oscillations, they help to improve the resolution by removing a background signal from electrons that are not focused by the lens.

The point contacts at $x = 0, L$, $|y| < \delta W/2$ connect to heavily doped metallic leads, at chemical potential μ_{lead} much larger than the band width t_y in the conductor. Only a small fraction t_y/μ_{lead} of the $N \approx \delta W/a$ propagating modes in the leads will couple effectively to the conductor, namely those modes that have transverse momentum small compared to longitudinal momentum. For $t_y/\mu_{\text{lead}} \ll 1$ we may thus remove the transverse

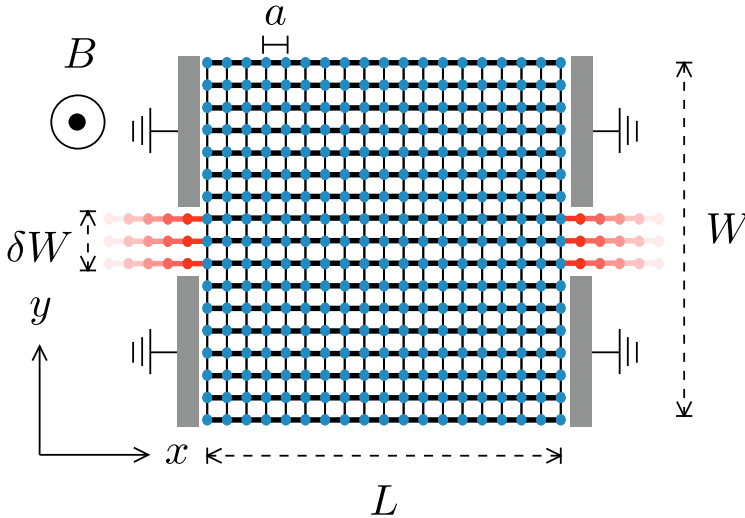


Figure 6.2. Layout of the tight-binding model, a 2D square lattice with anisotropic hopping energies. Strong and weak bonds are distinguished by thicker and thinner lines. The colors distinguish the conductor (blue), source and drain point contacts (red), and grounded terminals (grey).

hoppings in the leads, which are then described by the Hamiltonian (6.14) with $t_y = 0$. The perpendicular magnetic field is introduced in the hopping matrix elements via the Peierls substitution.

We use the tight-binding package Kwant [134, 163] to calculate the scattering matrix of the six-terminal-structure in Fig. 6.2. The $N \times N$ transmission matrix \mathbf{t} from source to drain then gives the conductance $G = (e^2/h) \text{Tr } \mathbf{t}\mathbf{t}^\dagger$.

The breathing mode injected into the conductor by a single mode in the lead is shown in Fig. 6.3. It has the expected periodicity of $\Delta x = \ell = a\Phi_0/\Phi$. In Fig. 6.4 we compare the variance of the spread in the y -direction as obtained from the tight-binding model with the result (6.13). For the open-orbit dispersion we take

$$\varepsilon(k_y) = (\hbar v_x/a) \arccos(-\tau \cos ak_y), \quad (6.16)$$

corresponding to one of the two branches in Eq. (6.15). The agreement is very good, without any adjustable parameter. The small oscillations with periodicity a present in the numerics are due to interference of the two branches of the dispersion relation, which we have neglected in Eq. (6.16). See App. 6.7 for a calculation that includes the interference effect.

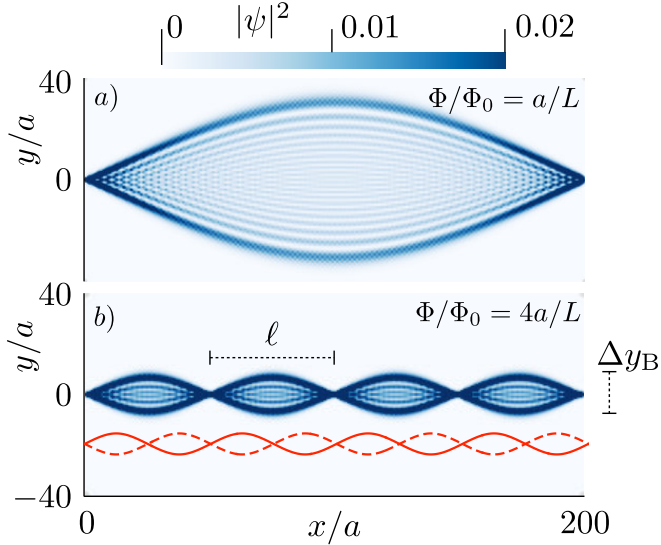


Figure 6.3. Blue data points: Wave function profile $|\psi(x, y)|^2$ injected into the conductor by a single mode in the lead, for two magnetic fields (corresponding to focal lengths $\ell \equiv a\Phi_0/\Phi = L$ and $\ell = L/4$). The wave function is normalized such that unit current is injected. The red curves in panel b) show two semiclassical orbits, calculated at the same magnetic field value as the breathing mode, to illustrate that the semiclassical orbits oscillate twice as rapidly as the breathing mode envelop.

Because $\hbar\dot{\mathbf{k}} = e\dot{\mathbf{r}} \times \mathbf{B}$, the trajectory $y_c(x)$ of a semiclassical wave packet is obtained from the equi-energy contour $\hbar v_x k_x + \varepsilon(k_y) = 0$ upon the transformation $\hbar k_x \mapsto eB_0 y$, $\hbar k_y \mapsto -eB_0 x$, thus

$$y_c(x) = (eB_0 v_x)^{-1} \varepsilon(-eB_0 x / \hbar). \quad (6.17)$$

A pair of semiclassical orbits is plotted in Fig. 6.3b (red curves), in order to emphasize the fact that the envelope of the breathing mode is not simply the superposition of two semiclassical orbits. Let us study the semiclassical correspondence in more detail.

6.4 Semiclassical approximation

For that purpose we consider (for a state $\psi(x, y)$ normalized to unity) the intensity profile $\rho_x(y) = |\psi(x, y)|^2$ in the weak-field semiclassical regime $\Phi \ll \Phi_0$. We Fourier transform $\rho_x(y)$ with respect to y , substitute Eq.

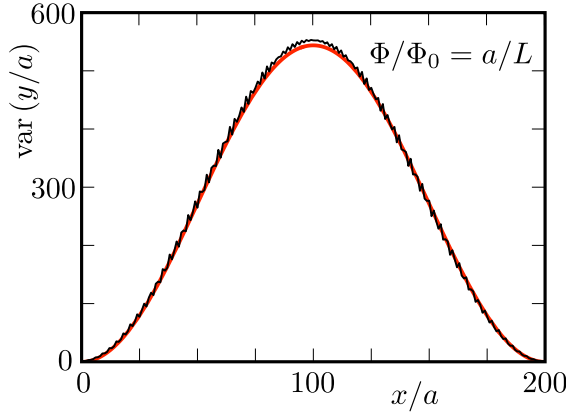


Figure 6.4. Variance of the spread in the y -direction as a function of the distance x from the point source. The smooth red curve is calculated from Eq. (6.13), the black curve with small oscillations is the numerical result from the tight-binding model. The numerical data is obtained by converting the wave function profile in Fig. 6.3a to a normalized intensity profile $\rho_x(y) = |\psi(x, y)|^2 / \sum_y |\psi(x, y)|^2$, and then computing $\sum_y y^2 \rho_x(y)$.

(6.7) for $\psi(x, y)$, retain only intensity variations with small wave number q , and finally Fourier transform back ¹:

$$\begin{aligned} \sum_y \rho_x(y) e^{iqy} &= a_y \int_0^{2\pi/a_y} \frac{dk_y}{2\pi} \\ &\quad \times \exp(i\omega(x, q + k_y) - i\omega(x, k_y)) \\ &= a_y \int_0^{2\pi/a_y} \frac{dk_y}{2\pi} \exp(iq\partial_{k_y}\omega(x, k_y) + \mathcal{O}(q^2)), \end{aligned} \quad (6.18)$$

$$\Rightarrow \rho_x(y) = a_y^2 \int_0^{2\pi/a_y} \frac{dk_y}{2\pi} \delta(\partial_{k_y}\omega(x, k_y) - y). \quad (6.19)$$

Now y is treated as a continuous variable (with $\sum_y \mapsto a_y^{-1} \int dy$).

¹We note that the expression for the variance $\langle y^2 \rangle_x = a_y^{-1} \int dy y^2 \rho_x(y)$ which follows from the semiclassical density profile (6.19) is *identical* to the result (6.9) which we obtained without making the semiclassical approximation. We have no more fundamental explanation for this correspondence. It does not carry over to higher moments.

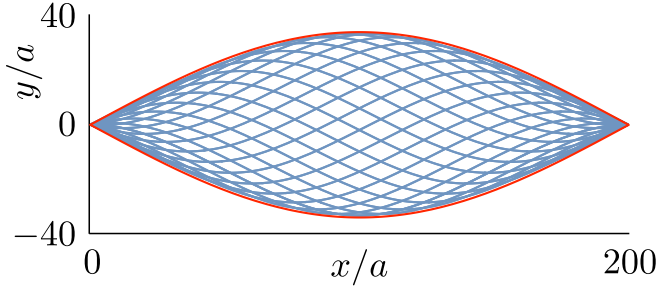


Figure 6.5. Superposition of semiclassical orbits that satisfy $y_c(x_0 - x) - y_c(x_0) - y = 0$, with x_0 varied between 0 and ℓ . The open orbit $y_c(x)$ is given by Eqs. (6.16) and (6.17), the parameters are those of Fig. 6.3a. The caustic is indicated in red.

For a constant magnetic field B_0 this can be worked out to

$$\rho_x(y) = a_y^2 e B_0 v_x \int_0^{2\pi/a_y} \frac{dk_y}{2\pi} \times \delta[\varepsilon(k_y + eB_0 x/\hbar) - \varepsilon(k_y) - eB_0 v_x y]. \quad (6.20)$$

In view of Eq. (6.17) the semiclassical density profile (6.20) can be rewritten as a superposition of displaced semiclassical orbits,

$$\rho_x(y) = (a_y/\ell) \int_0^\ell dx_0 \delta[y_c(x_0 - x) - y_c(x_0) - y]. \quad (6.21)$$

In Fig. 6.5 we have plotted this superposition for the same parameters as in the tight-binding simulation of Fig. 6.3a. The profiles match very well. The semiclassical calculation identifies the envelope as a caustic: an accumulation of classical trajectories with an infinite density, regularized by the finite wave length in the quantum calculation.

Eq. (6.20) allows for a semiclassical estimate for the amplitude of the breathing mode: Since $\rho_x(y) \equiv 0$ for all x when $|y| > (eB_0 v_x)^{-1} \max_{k_1, k_2} |\varepsilon(k_1) - \varepsilon(k_2)| \equiv (eB_0/\hbar)^{-1} \Delta k_x$ or, equivalently, when $|y| > \max_{x_1, x_2} |y_c(x_1) - y_c(x_2)| \equiv \Delta y_c$, we arrive at the relation

$$\Delta y_B = 2\Delta y_c = 2(\hbar/eB_0)\Delta k_x \quad (6.22)$$

between the amplitude Δk_x of the open orbit in momentum space, on the one hand, and the amplitudes Δy_B and Δy_c of breathing mode and semiclassical orbit in real space, on the other hand.

The ratio $R = \Delta y_B / \ell = (a_y / \pi) \Delta k_x$ is a magnetic field independent characteristic of the open orbit. For the anisotropic dispersion (6.14) one has

$$R \equiv \Delta y_B / \ell = (2a_y / \pi a_x) \arcsin(t_y / t_x). \quad (6.23)$$

The ratio equals 1/3 for the parameters in Fig. 6.3 ($a_y = a_x$, $t_x = 2t_y$).

6.5 Magnetoconductance oscillations

In the double point-contact geometry of Fig. 6.2 the breathing mode manifests itself as a conductance peak when the point contact separation L is an integer multiple of the period ℓ . This is the magnetoconductance oscillation studied in the context of twisted bilayer graphene in Ref. [191]. The magnetic field periodicity is

$$\Delta B = \frac{h}{eaL}. \quad (6.24)$$

A simulation of the tight-binding model in Fig. 6.6 shows the effect. The amplitude of the oscillations decays with increasing field because the point contact width δW is no longer able to resolve the decreasing amplitude Δy_B of the breathing mode. In terms of the dimensionless parameter $\xi(B) = (1/R)(\delta W / a_y)(\Phi / \Phi_0)$ we calculate that the ratio G_{\min} / G_{\max} of the minima and maxima of the conductance oscillations follows the curve ²:

$$\frac{G_{\min}}{G_{\max}} = \begin{cases} \xi(B) & \text{if } \xi(B) < 1/2, \\ 1 - \frac{1}{4}\xi(B)^{-1} & \text{if } \xi(B) > 1/2. \end{cases} \quad (6.25)$$

This agrees quite nicely with the numerics (blue curve in Fig. 6.6, without any fit parameter).

To make contact with Refs. [166, 192], we note that magnetoconductance oscillations with the same period (6.24) — upon exchange of L by W — can be observed without any point contacts, so without focusing of wave profiles. Instead of a current flowing along the open orbit the current should then flow perpendicularly to the open orbit, see Fig. 6.7. This

²Eq. (6.25) follows from a calculation of the fraction of the injected breathing mode that can enter the opposite point contact when $L = (n + 1/2)\ell$, so at the conductance minimum. This fraction equals G_{\min} / G_{\max} and is given by the integral $(\delta W \Delta y_B)^{-1} \int_{-\delta W/2}^{\delta W/2} dx (\min[\delta W/2, x + \Delta y_B/2] - \max[-\delta W/2, x - \Delta y_B/2])$.

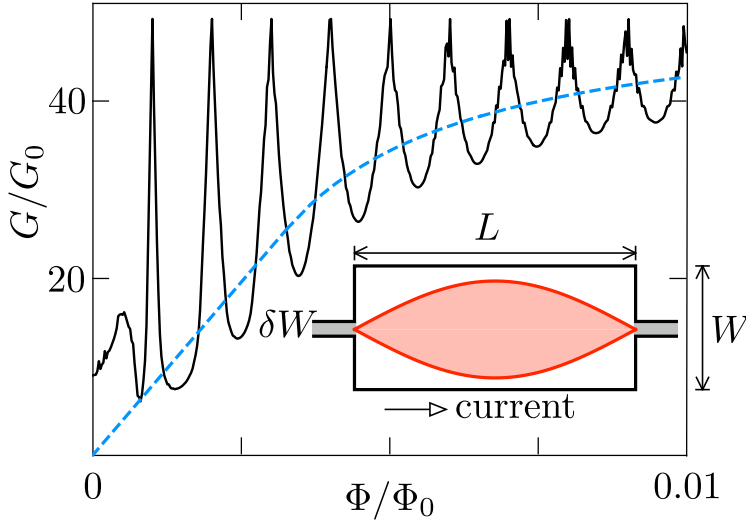


Figure 6.6. Conductance G (in units of the conductance quantum $G_0 = e^2/h$, per spin degree of freedom), as a function of magnetic field $B = \Phi/a^2$, computed from the tight-binding model in the point contact geometry shown in the inset (parameters $L/a = 1000$, $W/a = 440$, $\delta W/a = 51$). The breathing mode at the first conductance peak is shown in red. The periodicity of the oscillations is $\Delta\Phi/\Phi_0 = a/L = 10^{-3}$. Full refocusing of the breathing mode without any backscattering would give a conductance peak of NG_0 with $N = 51$ injected modes. The blue dashed curve is the calculated decay (6.25) of the amplitude of the conductance oscillations.

is the geometry first studied by Pippard [194]³, to explain conductance oscillations with period Φ_0/aW in cadmium [195, 196]. We refer to Refs. [166, 192] for a comprehensive theory and experiment on these magnetoconductance oscillations. Note that magnetic lensing plays no role in the Pippard geometry, one needs the spatial resolution of a point contact to excite a breathing mode.

³In connection with the simulations shown in Fig. 6.7, we note that these are for specular reflection at the boundary. That a disordered boundary is not needed for the magnetoconductance oscillations due to open orbits was pointed out by O. V. Kirichenko, V. G. Peschansky, and S. N. Savelieva, *Static skin effect in metals with open Fermi surfaces*, Sov. Phys. JETP **50**, 977 (1979).

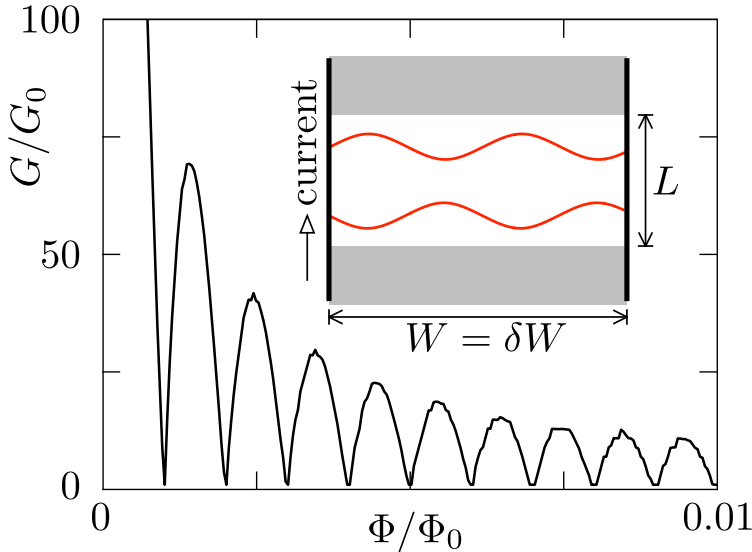


Figure 6.7. Same as Fig. 6.6, but now with the current flowing perpendicularly to the open orbits (a few are shown as red trajectories; parameters $W/a = 1000$, $L/a = 440$, no point contacts, $\delta W = W$). The conductance has a minimum when an open orbit fits in the width of the conductor, so when $B = n\Phi_0/aW$, $n = 1, 2, \dots$

6.6 Conclusion

In summary, we have presented a magnetic lensing effect with an unusually long focal length, set by the Bragg momentum \hbar/a rather than the Fermi momentum p_F . At a field of 1 T and for a lattice constant $a = 0.5$ nm the focal length $\ell = \hbar/eBa \approx 8 \mu\text{m}$ — an order of magnitude larger than in semiconductor electron focusing experiments [167]. Magnetic focusing is an effective way to study scattering processes [197] and in clean systems a large focal length would be an advantage.

The quantum mechanical origin of the focusing effect, Bragg reflection at Brillouin zone boundaries, does not imply that the magnetic lens needs long-range phase coherence — the breathing mode only requires phase coherence on the scale of the lattice constant. We note the contrast with the Aharonov-Bohm effect, where a magnetoconductance oscillation with period h/eS would require phase coherence over distances of order \sqrt{S} . The oscillation period (6.24) has $S = aL$ but only requires phase coherence over a length a , irrespectively of how large L might be.

We have applied the general theory to a simple model of an anisotropic dispersion, appropriate for the layered material (delafossites) studied in Refs. [166, 192] (with a ratio $\tau \simeq 10^{-2}$ between in-plane and out-of-plane hopping energies, and mean free paths of $20 \mu\text{m}$ [198]). For such a strong anisotropy the open orbits in the Brillouin zone are essentially decoupled from each other, allowing for closed-form expressions for the breathing mode in the fully quantum regime, Eq. (6.7), and in the semiclassical approximation, Eq. (6.21).

More complicated band structures would allow for multiple open orbits coupled by magnetic breakdown. The magnetic lens may then exhibit a complex pattern of caustics, one example (relevant for twisted bilayer graphene [191]) is analysed in App. 6.8.

6.7 Appendix: Calculation of the interference oscillations in the root-mean-square displacement

The tight-binding model calculation in Fig. 6.4 shows small oscillations on the scale of the lattice constant, which are absent in the analytical curve. To include these, we consider both branches of the equi-energy contour (6.15). These produce two open-orbit dispersions $\pm\varepsilon(k_y)$, with two corresponding wave function profiles ψ_{\pm} . With reference to Eq. (6.7) we have $\psi_+(x, y) = \psi(x, y)$ and $\psi_-(x, y) = \psi^*(x, -y)$.

We take an equal weight superposition $2^{-1/2}(\psi_+ + \psi_-)$. The average displacement remains equal to zero, the mean square displacement becomes

$$\langle y^2 \rangle_x = a_y \int_0^{2\pi/a_y} \frac{dk_y}{2\pi} \left(\partial_{k_y} \omega(x, k_y) \right)^2 [1 - \cos 2\omega(x, k_y)]. \quad (6.26)$$

The result, see Fig. 6.8, has oscillations with a somewhat smaller amplitude than in the numerics of Fig. 6.4, but the periodicity agrees nicely.

6.8 Appendix: Magnetic lens for multiple coupled open orbits

In the main text we considered the magnetic lens that results from a single open orbit in the Brillouin zone. As a more complicated example,

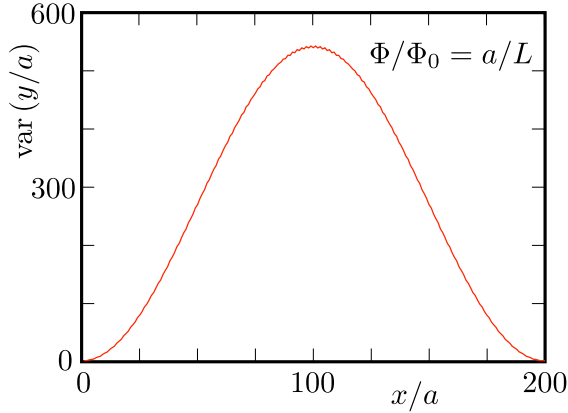


Figure 6.8. Variance of the spread in the y -direction as a function of the distance x from the point source, calculated from Eq. (6.26). This figure can be compared with Fig. 6.4, where the interference oscillations are neglected.

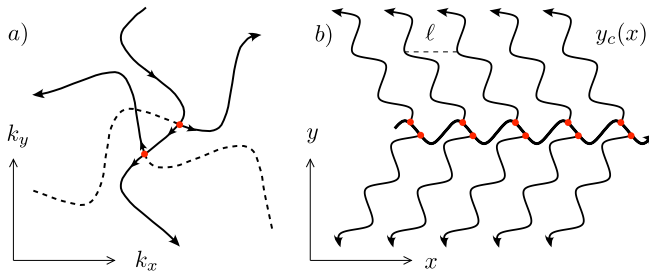


Figure 6.9. Panel *a*: Equi-energy contours in momentum space consisting of three sets of open orbits, at relative orientation of 120° . The arrows indicate the direction of motion in a magnetic field. The solid contours produce, upon rotation by 90° , the multi-branched real-space trajectory $y_c(x)$ shown in panel *b*. A trajectory initially moving in the $+x$ direction branches out into the $-x$ direction at the intersection points indicated by red dots. Higher order branch-outs are not considered, these would contribute with reduced amplitude.

we show in Fig. 6.9a the equi-energy contours of minimally twisted bilayer graphene [168], with three open orbits at a relative orientation of 120° . At an intersection an electron can switch from one orbit to the other, a process known as magnetic breakdown. The corresponding multi-branched classical trajectory $y_c(x)$ is shown in Fig. 6.9b. If we now apply the semi-classical formula (6.21) we obtain the complex pattern of caustics shown in Fig. 6.10.

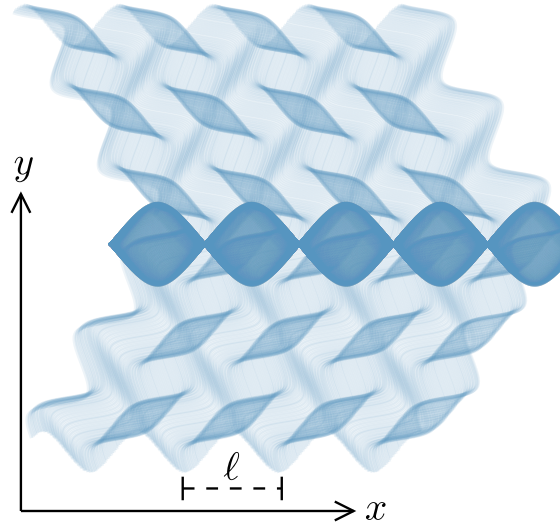


Figure 6.10. Superposition of the semiclassical orbits $y_c(x)$ from Fig. 6.9b that satisfy $y_c(x_0 - x) - y_c(x_0) - y = 0$, with x_0 varied between 0 and ℓ .

In Ref. [191] a fully quantum mechanical calculation was presented for the wave function profile. The semiclassical calculation well reproduces the qualitative features. Notice in particular that the side branches at an orientation of 120° are not simply copies of the main breathing mode. There is an extinction of the amplitude between two oscillations, which one might have suspected to be an interference effect. Instead it can be fully reproduced from a trajectory description.

Bibliography

- [1] B. D. Josephson. *Possible new effects in superconductive tunnelling*. Physics letters **1**, 251–253 (1962).
- [2] B. D. Josephson. *The discovery of tunnelling supercurrents*. Reviews of Modern Physics **46**, 251 (1974).
- [3] S. Strogatz. *Sync: The emerging science of spontaneous order*. (2004).
- [4] A. Braginski. *Consequences of Brian Josephson’s theoretical discovery*. Journal of Superconductivity and Novel Magnetism **34**, 1597–1600 (2021).
- [5] C. Beenakker, *Three “universal” mesoscopic Josephson effects*, in Transport phenomena in mesoscopic systems: proceedings of the 14th taniguchi symposium, shima, japan, november 10–14, 1991 (Springer, 1992), pp. 235–253.
- [6] P. Brooks, A. Kitaev, and J. Preskill. *Protected gates for superconducting qubits*. Physical Review A **87**, 052306 (2013).
- [7] K. Kalashnikov, W. T. Hsieh, W. Zhang, W.-S. Lu, P. Kamenov, A. Di Paolo, A. Blais, M. E. Gershenson, and M. Bell. *Bifluxon: Fluxon-parity-protected superconducting qubit*. PRX Quantum **1**, 010307 (2020).
- [8] S.-B. Zhang, L.-H. Hu, and T. Neupert. *Finite-momentum cooper pairing in proximitized altermagnets*. Nature Communications **15**, 1801 (2024).
- [9] J. A. Ouassou, A. Brataas, and J. Linder. *Dc Josephson effect in altermagnets*. Physical Review Letters **131**, 076003 (2023).
- [10] M. Tinkham. *Introduction to superconductivity*. (Courier Corporation, 2004).

- [11] V. Ambegaokar and A. Baratoff. *Tunneling between superconductors*. Phys. Rev. Lett. **10**, 486–489 (1963).
- [12] L. Glazman and G. Catelani. *Bogoliubov quasiparticles in superconducting qubits*. SciPost Physics Lecture Notes, 031 (2021).
- [13] Y. V. Nazarov and Y. M. Blanter. *Quantum transport: introduction to nanoscience*. (Cambridge University press, 2009).
- [14] A. F. Andreev. *Thermal conductivity of the intermediate state of superconductors*. Sov. Phys. JETP **19**, 1228 (1964).
- [15] C. W. J. Beenakker. *Universal limit of critical-current fluctuations in mesoscopic Josephson junctions*. Phys. Rev. Lett. **67**, 3836–3839 (1991).
- [16] A. Bargerbos, W. Uilhoorn, C.-K. Yang, P. Krogstrup, L. P. Kouwenhoven, G. de Lange, B. van Heck, and A. Kou. *Observation of vanishing charge dispersion of a nearly open superconducting island*. Phys. Rev. Lett. **124**, 246802 (2020).
- [17] A. Kringhøj, B. van Heck, T. W. Larsen, O. Erlandsson, D. Sabonis, P. Krogstrup, L. Casparis, K. D. Petersson, and C. M. Marcus. *Suppressed charge dispersion via resonant tunneling in a single-channel transmon*. Phys. Rev. Lett. **124**, 246803 (2020).
- [18] P. D. Kurilovich, V. D. Kurilovich, V. Fatemi, M. H. Devoret, and L. I. Glazman. *Microwave response of an Andreev bound state*. Phys. Rev. B **104**, 174517 (2021).
- [19] T. Meng, S. Florens, and P. Simon. *Self-consistent description of Andreev bound states in Josephson quantum dot devices*. Phys. Rev. B **79**, 224521 (2009).
- [20] D. O. Oriekhov, Y. Cheipesh, and C. W. J. Beenakker. *Voltage staircase in a current-biased quantum-dot Josephson junction*. Phys. Rev. B **103**, 094518 (2021).
- [21] P. Recher, Y. V. Nazarov, and L. P. Kouwenhoven. *Josephson light-emitting diode*. Phys. Rev. Lett. **104**, 156802 (2010).
- [22] T. Vakhtel and B. van Heck. *Quantum phase slips in a resonant Josephson junction*. Phys. Rev. B **107**, 195405 (2023).
- [23] L. Glazman and K. Matveev. *Resonant Josephson current through Kondo impurities in a tunnel barrier*. JETP Lett **49**, 659–662 (1989).

- [24] V. Bouchiat, D Vion, P. Joyez, D Esteve, and M. Devoret. *Quantum coherence with a single Cooper pair*. Physica Scripta **1998**, 165 (1998).
- [25] A. Shnirman, G. Schön, and Z. Hermon. *Quantum manipulations of small Josephson junctions*. Physical Review Letters **79**, 2371 (1997).
- [26] J. Koch, T. M. Yu, J. Gambetta, A. A. Houck, D. I. Schuster, J. Majer, A. Blais, M. H. Devoret, S. M. Girvin, and R. J. Schoelkopf. *Charge-insensitive qubit design derived from the Cooper pair box*. Phys. Rev. A **76**, 042319 (2007).
- [27] J. Koch, V. Manucharyan, M. H. Devoret, and L. I. Glazman. *Charging effects in the inductively shunted Josephson junction*. Phys. Rev. Lett. **103**, 217004 (2009).
- [28] V. E. Manucharyan, J. Koch, L. I. Glazman, and M. H. Devoret. *Fluxonium: Single Cooper-pair circuit free of charge offsets*. Science **326**, 113–116 (2009).
- [29] G. Zhu and J. Koch. *Asymptotic expressions for charge-matrix elements of the fluxonium circuit*. Physical Review B **87**, 144518 (2013).
- [30] L. B. Nguyen, Y.-H. Lin, A. Somoroff, R. Mencia, N. Grabon, and V. E. Manucharyan. *High-Coherence Fluxonium Qubit*. Phys. Rev. X **9**, 041041 (2019).
- [31] F. Bao, H. Deng, D. Ding, R. Gao, X. Gao, C. Huang, X. Jiang, H.-S. Ku, Z. Li, X. Ma, X. Ni, J. Qin, Z. Song, H. Sun, C. Tang, T. Wang, F. Wu, T. Xia, W. Yu, F. Zhang, G. Zhang, X. Zhang, J. Zhou, X. Zhu, Y. Shi, J. Chen, H.-H. Zhao, and C. Deng. *Fluxonium: An Alternative Qubit Platform for High-Fidelity Operations*. Phys. Rev. Lett. **129**, 010502 (2022).
- [32] L. B. Nguyen, G. Koolstra, Y. Kim, A. Morvan, T. Chistolini, S. Singh, K. N. Nesterov, C. Jünger, L. Chen, Z. Pedramrazi, B. K. Mitchell, J. M. Kreikebaum, S. Puri, D. I. Santiago, and I. Siddiqi. *Blueprint for a high-performance fluxonium quantum processor*. PRX Quantum **3**, 037001 (2022).
- [33] A. Somoroff, Q. Ficheux, R. A. Mencia, H. Xiong, R. Kuzmin, and V. E. Manucharyan. *Millisecond coherence in a superconducting qubit*. Phys. Rev. Lett. **130**, 267001 (2023).

- [34] I. V. Pechenezhskiy, R. A. Mencia, L. B. Nguyen, Y.-H. Lin, and V. E. Manucharyan. *The superconducting quasicharge qubit*. *Nature* **585**, 368–371 (2020).
- [35] E. S. Morell, J. Correa, P Vargas, M Pacheco, and Z Barticevic. *Flat bands in slightly twisted bilayer graphene: tight-binding calculations*. *Physical Review B* **82**, 121407 (2010).
- [36] R. Bistritzer and A. H. MacDonald. *Moiré bands in twisted double-layer graphene*. *Proceedings of the National Academy of Sciences* **108**, 12233–12237 (2011).
- [37] P. J. Ledwith, E. Khalaf, and A. Vishwanath. *Strong coupling theory of magic-angle graphene: a pedagogical introduction*. *Annals of Physics* **435**, 168646 (2021).
- [38] K. Kim, A. DaSilva, S. Huang, B. Fallahazad, S. Larentis, T. Taniguchi, K. Watanabe, B. J. LeRoy, A. H. MacDonald, and E. Tutuc. *Tunable moiré bands and strong correlations in small-twist-angle bilayer graphene*. *Proceedings of the National Academy of Sciences* **114**, 3364–3369 (2017).
- [39] D. Wong, K. P. Nuckolls, M. Oh, B. Lian, Y. Xie, S. Jeon, K. Watanabe, T. Taniguchi, B. A. Bernevig, and A. Yazdani. *Cascade of electronic transitions in magic-angle twisted bilayer graphene*. *Nature* **582**, 198–202 (2020).
- [40] S. Carr, D. Massatt, S. Fang, P. Cazeaux, M. Luskin, and E. Kaxiras. *Twistronics: manipulating the electronic properties of two-dimensional layered structures through their twist angle*. *Physical Review B* **95**, 075420 (2017).
- [41] C. D. Beule, F. Dominguez, and P. Recher. *Network model and four-terminal transport in minimally twisted bilayer graphene*. *Phys. Rev. B* **104**, 195410 (2021).
- [42] P. San-Jose and E. Prada. *Helical networks in twisted bilayer graphene under interlayer bias*. *Phys. Rev. B* **88**, 121408(R) (2013).
- [43] D. K. Efimkin and A. H. MacDonald. *Helical network model for twisted bilayer graphene*. *Phys. Rev. B* **98**, 035404 (2018).
- [44] A. C. Neto, F. Guinea, N. M. Peres, K. S. Novoselov, and A. K. Geim. *The electronic properties of graphene*. *Reviews of modern physics* **81**, 109 (2009).

- [45] F. Guinea and N. R. Walet. *Electrostatic effects, band distortions, and superconductivity in twisted graphene bilayers*. Proceedings of the National Academy of Sciences **115**, 13174–13179 (2018).
- [46] H. Yoo, R. Engelke, S. Carr, S. Fang, K. Zhang, P. Cazeaux, S. H. Sung, R. Hovden, A. W. Tsen, T. Taniguchi, et al. *Atomic and electronic reconstruction at the van der waals interface in twisted bilayer graphene*. Nature materials **18**, 448–453 (2019).
- [47] N. N. Nam and M. Koshino. *Lattice relaxation and energy band modulation in twisted bilayer graphene*. Physical Review B **96**, 075311 (2017).
- [48] J. D. Verbakel, Q. Yao, K. Sotthewes, and H. J. W. Zandvliet. *Valley-protected one-dimensional states in small-angle twisted bilayer graphene*. Phys. Rev. B **103**, 165134 (2021).
- [49] S. Huang, K. Kim, D. K. Efimkin, T. Lovorn, T. Taniguchi, K. Watanabe, A. H. MacDonald, E. Tutuc, and B. J. LeRoy. *Topologically protected helical states in minimally twisted bilayer graphene*. Phys. Rev. Lett. **121**, 037702 (2018).
- [50] S. G. Xu, A. I. Berdyugin, P. Kumaravadivel, F. Guinea, R. K. Kumar, D. A. Bandurin, S. V. Morozov, W. Kuang, B. Tsim, S. Liu, J. H. Edgar, I. V. Grigorieva, V. I. Fal’ko, M. Kim, and A. K. Geim. *Giant oscillations in a triangular network of one-dimensional states in marginally twisted graphene*. Nature Commun. **10**, 4008 (2019).
- [51] P. Rickhaus, J. Wallbank, S. Slizovskiy, R. Pisoni, H. Overweg, Y. Lee, M. Eich, M. H. Liu, K. Watanabe, T. Taniguchi, T. Ihn, and K. Ensslin. *Transport through a network of topological channels in twisted bilayer graphene*. Nano Lett. **18**, 6725 (2018).
- [52] F. Bloch. *Über die Quantenmechanik der Elektronen in Kristallgittern*. Z. Physik **52**, 555 (1929).
- [53] C. Zener. *A theory of the electrical breakdown of solid dielectrics*. Proc. R. Soc. London A **145**, 523 (1934).
- [54] K. Leo, P. H. Bolivar, F. Brüggemann, R. Schwedler, and K. Köhler. *Observation of Bloch oscillations in a semiconductor superlattice*. Solid State Comm. **84**, 943 (1992).

- [55] C. Waschke, H. G. Roskos, R. Schwedler, K. Leo, H. Kurz, and K. Köhler. *Coherent submillimeter-wave emission from Bloch oscillations in a semiconductor superlattice*. Phys. Rev. Lett. **70**, 3319 (1993).
- [56] H. G. Roskos. *Coherent emission of electromagnetic pulses from Bloch oscillations in semiconductor superlattices*. Adv. Solid State Phys. **34**, 297 (1995).
- [57] P. G. Savvidis, B. Kolasa, G. Lee, and S. J. Allen. *Resonant crossover of terahertz loss to the gain of a Bloch oscillating InAs/AlSb superlattice*. Phys. Rev. Lett. **92**, 196802 (2004).
- [58] A. Fahimniya, Z. Dong, E. I. Kiselev, and L. Levitov. *Synchronizing Bloch-oscillating free carriers in moiré flat bands*. Phys. Rev. Lett. **126**, 256803 (2021).
- [59] T. Hartmann, F. Keck, H. J. Korsch, and S. Mossmann. *Dynamics of Bloch oscillations*. New J. Phys. **6**, 2 (2004).
- [60] I. I. Mazin, K. Koepernik, M. D. Johannes, R. González-Hernández, and L. Šmejkal. *Prediction of unconventional magnetism in doped FeSb₂*. Proceedings of the National Academy of Sciences **118**, e2108924118 (2021).
- [61] L.-D. Yuan, Z. Wang, J.-W. Luo, E. I. Rashba, and A. Zunger. *Giant momentum-dependent spin splitting in centrosymmetric low-Z antiferromagnets*. Physical Review B **102**, 014422 (2020).
- [62] S. Hayami, Y. Yanagi, and H. Kusunose. *Momentum-dependent spin splitting by collinear antiferromagnetic ordering*. Journal of the Physical Society of Japan **88**, 123702 (2019).
- [63] L. Šmejkal, R. González-Hernández, T. Jungwirth, and J. Sinova. *Crystal time-reversal symmetry breaking and spontaneous Hall effect in collinear antiferromagnets*. Science Advances **6**, eaaz8809 (2020).
- [64] L. Šmejkal, J. Sinova, and T. Jungwirth. *Beyond conventional ferromagnetism and antiferromagnetism: a phase with nonrelativistic spin and crystal rotation symmetry*. Phys. Rev. X **12**, 031042 (2022).
- [65] L. Šmejkal, J. Sinova, and T. Jungwirth. *Emerging research landscape of altermagnetism*. Phys. Rev. X **12**, 040501 (2022).

- [66] L. Šmejkal, A. H. MacDonald, J. Sinova, S. Nakatsuji, and T. Jungwirth. *Anomalous hall antiferromagnets*. *Nature Reviews Materials* **7**, 482–496 (2022).
- [67] R. D. G. Betancourt, J. Zubáč, R. González-Hernández, K. Geishendorf, Z. Šobáň, G. Springholz, K. Olejník, L. Šmejkal, J. Sinova, T. Jungwirth, S. T. B. Goennenwein, A. Thomas, H. Reichlová, J. Železný, and D. Krieger. *Spontaneous anomalous Hall effect arising from an unconventional compensated magnetic phase in a semiconductor*. *Phys. Rev. Lett.* **130**, 036702 (2023).
- [68] Z. Feng, X. Zhou, L. Šmejkal, L. Wu, Z. Zhu, H. Guo, R. González-Hernández, X. Wang, H. Yan, P. Qin, et al. *An anomalous Hall effect in altermagnetic ruthenium dioxide*. *Nature Electronics* **5**, 735–743 (2022).
- [69] I. I. Mazin. *Altermagnetism — a new punch line of fundamental magnetism*. *Phys. Rev. X* **12**, 040002 (2022).
- [70] I. I. Mazin. *Altermagnetism in MnTe: origin, predicted manifestations, and routes to detwinning*. *Phys. Rev. B* **107**, L100418 (2023).
- [71] .*Observation of time-reversal symmetry breaking in the band structure of altermagnetic RuO₂*, author=Fedchenko, Olena and Minár, Jan and Akashdeep, Akashdeep and D’Souza, Sunil Wilfred and Vasilyev, Dmitry and Tkach, Olena and Odenbreit, Lukas and Nguyen, Quynh and Kutnyakhov, Dmytro and Wind, Nils and others, journal=Science Advances, volume=10, number=5, pages=eadj4883, year=2024, publisher=American Association for the Advancement of Science.
- [72] L. Šmejkal, A. B. Hellenes, R. González-Hernández, J. Sinova, and T. Jungwirth. *Giant and tunneling magnetoresistance in unconventional collinear antiferromagnets with nonrelativistic spin-momentum coupling*. *Phys. Rev. X* **12**, 011028 (2022).
- [73] J Krempaský, L Šmejkal, S. D’Souza, M Hajlaoui, G Springholz, K Uhlířová, F Alarab, P. Constantinou, V Strocov, D Usanov, et al. *Altermagnetic lifting of Kramers spin degeneracy*. *Nature* **626**, 517–522 (2024).
- [74] K.-H. Ahn, A. Hariki, K.-W. Lee, and J. Kuneš. *Antiferromagnetism in RuO₂ as d-wave Pomeranchuk instability*. *Physical Review B* **99**, 184432 (2019).

- [75] M Podgorny and J Oleszkiewicz. *Electronic structure of antiferromagnetic MnTe*. Journal of Physics C: Solid State Physics **16**, 2547 (1983).
- [76] I. Mazin. *Altermagnetism then and now*. Physics **17**, 4 (2024).
- [77] C. Sun, A. Brataas, and J. Linder. *Andreev reflection in altermagnets*. Physical Review B **108**, 054511 (2023).
- [78] M. Papaj. *Andreev reflection at the altermagnet-superconductor interface*. Physical Review B **108**, L060508 (2023).
- [79] D. Zhu, Z.-Y. Zhuang, Z. Wu, and Z. Yan. *Topological superconductivity in two-dimensional altermagnetic metals*. Physical Review B **108**, 184505 (2023).
- [80] S. A. A. Ghorashi, T. L. Hughes, and J. Cano. *Altermagnetic routes to Majorana modes in zero net magnetization*. eprint: [arXiv:2306.09413](https://arxiv.org/abs/2306.09413).
- [81] M. Fleischmann, R. Gupta, F. Wulfschläger, S. Theil, D. Weckbecker, V. Meded, S. Sharma, B. Meyer, and S. Shallcross. *Perfect and controllable nesting in minimally twisted bilayer graphene*. Nano Lett. **20**, 971 (2020).
- [82] B. Tsim, N. N. T. Nam, and M. Koshino. *Perfect one-dimensional chiral states in biased twisted bilayer graphene*. Phys. Rev. B **101**, 125409 (2020).
- [83] D. Haviland. *Quantum phase slips*. Nature Physics **6**, 565–566 (2010).
- [84] E. Chow, P. Delsing, and D. B. Haviland. *Length-Scale Dependence of the Superconductor-to-Insulator Quantum Phase Transition in One Dimension*. Phys. Rev. Lett. **81**, 204–207 (1998).
- [85] C. N. Lau, N. Markovic, M. Bockrath, A. Bezryadin, and M. Tinkham. *Quantum phase slips in superconducting nanowires*. Phys. Rev. Lett. **87**, 217003 (2001).
- [86] J. Mooij and Y. V. Nazarov. *Superconducting nanowires as quantum phase-slip junctions*. Nature Physics **2** (2006).
- [87] I. M. Pop, I Protopopov, F. Lecocq, Z. Peng, B. Pannetier, O. Buisson, and W. Guichard. *Measurement of the effect of quantum phase slips in a Josephson junction chain*. Nature Physics **6**, 589–592 (2010).

- [88] O. Astafiev, L. Ioffe, S Kafanov, Y. A. Pashkin, K. Y. Arutyunov, D Shahar, O Cohen, and J. S. Tsai. *Coherent quantum phase slip*. Nature **484**, 355–358 (2012).
- [89] V. E. Manucharyan, N. A. Masluk, A. Kamal, J. Koch, L. I. Glazman, and M. H. Devoret. *Evidence for coherent quantum phase slips across a Josephson junction array*. Phys. Rev. B **85**, 024521 (2012).
- [90] A. D. Zaikin, D. S. Golubev, A. van Otterlo, and G. T. Zimányi. *Quantum phase slips and transport in ultrathin superconducting wires*. Phys. Rev. Lett. **78**, 1552–1555 (1997).
- [91] F. W. J. Hekking and L. I. Glazman. *Quantum fluctuations in the equilibrium state of a thin superconducting loop*. Phys. Rev. B **55**, 6551–6558 (1997).
- [92] R. Fazio and H. van der Zant. *Quantum phase transitions and vortex dynamics in superconducting networks*. Physics Reports **355**, 235–334 (2001).
- [93] D. S. Golubev and A. D. Zaikin. *Quantum tunneling of the order parameter in superconducting nanowires*. Phys. Rev. B **64**, 014504 (2001).
- [94] K. A. Matveev, A. I. Larkin, and L. I. Glazman. *Persistent current in superconducting nanorings*. Phys. Rev. Lett. **89**, 096802 (2002).
- [95] H. P. Büchler, V. B. Geshkenbein, and G. Blatter. *Quantum fluctuations in thin superconducting wires of finite length*. Phys. Rev. Lett. **92**, 067007 (2004).
- [96] G. Refael, E. Demler, Y. Oreg, and D. S. Fisher. *Superconductor-to-normal transitions in dissipative chains of mesoscopic grains and nanowires*. Phys. Rev. B **75**, 014522 (2007).
- [97] B. I. Halperin, G. Refael, and E. Demler. *Resistance in superconductors*. International Journal of Modern Physics B **24**, 4039–4080 (2010).
- [98] D. V. Averin, A. B. Zorin, and K. K. Likharev. *Bloch oscillations in small Josephson junctions*. Sov. Phys. JETP **61**, 407–413 (1985).
- [99] Y. Nakamura, Y. A. Pashkin, and J. Tsai. *Coherent control of macroscopic quantum states in a single-Cooper-pair box*. nature **398**, 786–788 (1999).

- [100] D. Vion, A. Aassime, A. Cottet, P. Joyez, H. Pothier, C. Urbina, D. Esteve, and M. H. Devoret. *Manipulating the quantum state of an electrical circuit*. Science **296**, 886–889 (2002).
- [101] J. A. Schreier, A. A. Houck, J. Koch, D. I. Schuster, B. R. Johnson, J. M. Chow, J. M. Gambetta, J. Majer, L. Frunzio, M. H. Devoret, S. M. Girvin, and R. J. Schoelkopf. *Suppressing charge noise decoherence in superconducting charge qubits*. Phys. Rev. B **77**, 180502 (2008).
- [102] D. Ristè, C. Bultink, M. J. Tiggelman, R. N. Schouten, K. W. Lehnert, and L. DiCarlo. *Millisecond charge-parity fluctuations and induced decoherence in a superconducting transmon qubit*. Nature communications **4**, 1913 (2013).
- [103] K. Serniak, M. Hays, G. de Lange, S. Diamond, S. Shankar, L. D. Burkhardt, L. Frunzio, M. Houzet, and M. H. Devoret. *Hot nonequilibrium quasiparticles in transmon qubits*. Phys. Rev. Lett. **121**, 157701 (2018).
- [104] K. Serniak, S. Diamond, M. Hays, V. Fatemi, S. Shankar, L. Frunzio, R. Schoelkopf, and M. Devoret. *Direct dispersive monitoring of charge parity in offset-charge-sensitive transmons*. Phys. Rev. Appl. **12**, 014052 (2019).
- [105] W. Uilhoorn, J. G. Kroll, A. Bargerbos, S. D. Nabi, C.-K. Yang, P. Krogstrup, L. P. Kouwenhoven, A. Kou, and G. de Lange. *Quasiparticle trapping by orbital effect in a hybrid superconducting-semiconducting circuit*. arXiv preprint arXiv:2105.11038 (2021).
- [106] C. Kurter, C. Murray, R. Gordon, B. Wymore, M. Sandberg, R. Shelby, A. Eddins, V. Adiga, A. Finck, E. Rivera, et al. *Quasiparticle tunneling as a probe of Josephson junction barrier and capacitor material in superconducting qubits*. npj Quantum Information **8**, 31 (2022).
- [107] O. Erlandsson, D. Sabonis, A. Kringhøj, T. W. Larsen, P. Krogstrup, K. D. Petersson, and C. M. Marcus. *Parity switching in a full-shell superconductor-semiconductor nanowire qubit*. Physical Review B **108**, L121406 (2023).
- [108] F Hassler, A. Akhmerov, and C. Beenakker. *The top-transmon: a hybrid superconducting qubit for parity-protected quantum computation*. New Journal of Physics **13**, 095004 (2011).

- [109] D. Aasen, M. Hell, R. V. Mishmash, A. Higginbotham, J. Danon, M. Leijnse, T. S. Jespersen, J. A. Folk, C. M. Marcus, K. Flensberg, and J. Alicea. *Milestones toward Majorana-based quantum computing*. Phys. Rev. X **6**, 031016 (2016).
- [110] R. Aguado. *A perspective on semiconductor-based superconducting qubits*. Applied Physics Letters **117**, 240501 (2020).
- [111] A. Gyenis, A. Di Paolo, J. Koch, A. Blais, A. A. Houck, and D. I. Schuster. *Moving beyond the transmon: Noise-protected superconducting quantum circuits*. PRX Quantum **2**, 030101 (2021).
- [112] B. R. Holstein. *Semiclassical treatment of the periodic potential*. American Journal of Physics **56**, 894–898 (1988).
- [113] A. Altland and B. D. Simons. *Condensed matter field theory*. 2nd ed. (Cambridge University Press, 2010), pp. 154–155.
- [114] D. V. Averin. *Coulomb blockade in superconducting quantum point contacts*. Phys. Rev. Lett. **82**, 3685–3688 (1999).
- [115] D. Ivanov and M. Feigel'man. *Coulomb effects in a ballistic one-channel S-S-S device*. Journal of Experimental and Theoretical Physics **87**, 349–356 (1998).
- [116] D. Averin. *Quantum dynamics of superconducting point contacts: chiral anomaly, Landau–Zener transitions, and all that*. Superlattices and microstructures **25**, 891–904 (1999).
- [117] C. W. J. Beenakker and H. van Houten, *Resonant Josephson current through a quantum dot*, in Single-electron tunneling and mesoscopic devices, edited by H. Koch and H. Lübbig (1992), pp. 175–179.
- [118] I. A. Devyatov and M. Y. Kupriyanov. *Resonant Josephson tunneling through S-I-S junctions of arbitrary size*. Journal of Experimental and Theoretical Physics **85**, 189–194 (1997).
- [119] A. Y. Kitaev. *Unpaired Majorana fermions in quantum wires*. Physics-Uspekhi **44**, 131–136 (2001).
- [120] L. Fu and C. L. Kane. *Josephson current and noise at a superconductor/quantum - spin - Hall-insulator/superconductor junction*. Phys. Rev. B **79**, 161408 (2009).

- [121] C. Beenakker, *Three “universal” mesoscopic Josephson effects*, in *Transport phenomena in mesoscopic systems* (Springer, 1992), pp. 235–253.
- [122] A Martín-Rodero and A Levy Yeyati. *Josephson and Andreev transport through quantum dots*. *Advances in Physics* **60**, 899–958 (2011).
- [123] C Janvier, L. Tosi, L Bretheau, Ç. Girit, M Stern, P Bertet, P Joyez, D Vion, D Esteve, M. Goffman, et al. *Coherent manipulation of Andreev states in superconducting atomic contacts*. *Science* **349**, 1199–1202 (2015).
- [124] M. Hays, G. de Lange, K. Serniak, D. J. van Woerkom, D. Bouman, P. Krogstrup, J. Nygård, A. Geresdi, and M. H. Devoret. *Direct microwave measurement of Andreev-bound-state dynamics in a semiconductor-nanowire Josephson junction*. *Phys. Rev. Lett.* **121**, 047001 (2018).
- [125] M. Hays, V. Fatemi, D. Bouman, J. Cerrillo, S. Diamond, K. Serniak, T. Connolly, P. Krogstrup, J. Nygård, A. L. Yeyati, A. Geresdi, and M. H. Devoret. *Coherent manipulation of an Andreev spin qubit*. *Science* **373**, 430–433 (2021).
- [126] A. Bargerbos, M. Pita-Vidal, J. Ávila, L. J. Splitthoff, L. Grünhaupt, J. J. Westorp, C. K. Andersen, Y. Liu, L. P. Kouwenhoven, R. Aguado, A. Kou, and B. van Heck. *Singlet-doublet transitions of a quantum dot Josephson junction detected in a transmon circuit*. *PRX Quantum* **3**, 030311 (2022).
- [127] D. A. Ivanov and M. V. Feigel’man. *Two-level Hamiltonian of a superconducting quantum point contact*. *Phys. Rev. B* **59**, 8444–8446 (1999).
- [128] A. Zazunov, V. S. Shumeiko, E. N. Bratus’, J. Lantz, and G. Wendin. *Andreev level qubit*. *Phys. Rev. Lett.* **90**, 087003 (2003).
- [129] L. D. Landau and E. M. Lifshitz. *Quantum mechanics: non-relativistic theory*. Vol. 3 (Elsevier, 2013), pp. 167–170.
- [130] I. S. Gradshteyn and I. M. Ryzhik. *Table of integrals, series, and products*. Vol. 3 (Academic press, 2014), pp. 1064–1067.
- [131] K. Likharev and A. Zorin. *Theory of the Bloch-wave oscillations in small Josephson junctions*. *Journal of low temperature physics* **59**, 347–382 (1985).

- [132] S. Corlevi, W. Guichard, F. W. J. Hekking, and D. B. Haviland. *Phase-charge duality of a Josephson junction in a fluctuating electromagnetic environment*. Phys. Rev. Lett. **97**, 096802 (2006).
- [133] And L. B. Ioffe. *Voltage-current curves for small Josephson junction arrays: Semiclassical treatment*. Phys. Rev. B **76**, 214507 (2007).
- [134] T. Vakhtel, D. O. Oriekhov, and C. W. J. Beenakker, *Computer code and data for Bloch oscillations in the magnetoconductance of twisted bilayer graphene*, <https://doi.org/10.5281/zenodo.7121013>, 2007.
- [135] L. Fu. *Electron Teleportation via Majorana Bound States in a Mesoscopic Superconductor*. Phys. Rev. Lett. **104**, 056402 (2010).
- [136] D. Pikulin, K. Flensberg, L. I. Glazman, M. Houzet, and R. M. Lutchyn. *Coulomb Blockade of a Nearly Open Majorana Island*. Phys. Rev. Lett. **122**, 016801 (2019).
- [137] D. Pekker, C.-Y. Hou, D. L. Bergman, S. Goldberger, I. Adagideli, and F. Hassler. *Suppression of 2π phase slip due to hidden zero modes in one-dimensional topological superconductors*. Phys. Rev. B **87**, 064506 (2013).
- [138] R. Rodríguez-Mota, S. Vishveshwara, and T. Pereg-Barnea. *Revisiting 2π phase slip suppression in topological Josephson junctions*. Phys. Rev. B **99**, 024517 (2019).
- [139] A. E. Svetogorov, D. Loss, and J. Klinovaja. *Critical current for an insulating regime of an underdamped current-biased topological Josephson junction*. Phys. Rev. Research **2**, 033448 (2020).
- [140] B. van Heck, F. Hassler, A. R. Akhmerov, and C. W. J. Beenakker. *Coulomb stability of the 4π -periodic Josephson effect of Majorana fermions*. Phys. Rev. B **84**, 180502 (2011).
- [141] D. I. Pikulin and Y. V. Nazarov. *Phenomenology and dynamics of a Majorana Josephson junction*. Phys. Rev. B **86**, 140504 (2012).
- [142] A. Keselman, C. Murthy, B. van Heck, and B. Bauer. *Spectral response of Josephson junctions with low-energy quasiparticles*. SciPost Phys. **7**, 050 (2019).
- [143] J. Clarke and F. K. Wilhelm. *Superconducting quantum bits*. Nature **453**, 1031–1042 (2008).

- [144] A. Blais, A. L. Grimsmo, S. M. Girvin, and A. Wallraff. *Circuit quantum electrodynamics*. Rev. Mod. Phys. **93**, 025005 (2021).
- [145] B Douçot and L. Ioffe. *Physical implementation of protected qubits*. Reports on Progress in Physics **75**, 072001 (2012).
- [146] L Bretheau, Ç. Girit, H. Pothier, D. Esteve, and C Urbina. *Exciting Andreev pairs in a superconducting atomic contact*. Nature **499**, 312–315 (2013).
- [147] S. N. Shevchenko, S. Ashhab, and F. Nori. *Landau–Zener–Stückelberg interferometry*. Physics Reports **492**, 1–30 (2010).
- [148] N. Earnest, S. Chakram, Y. Lu, N. Irons, R. K. Naik, N. Leung, L. Ocola, D. A. Czaplewski, B. Baker, J. Lawrence, J. Koch, and D. I. Schuster. *Realization of a Λ system with metastable states of a capacitively shunted fluxonium*. Phys. Rev. Lett. **120**, 150504 (2018).
- [149] H. Zhang, S. Chakram, T. Roy, N. Earnest, Y. Lu, Z. Huang, D. K. Weiss, J. Koch, and D. I. Schuster. *Universal fast-flux control of a coherent, low-frequency qubit*. Phys. Rev. X **11**, 011010 (2021).
- [150] E. Ginossar and E. Grosfeld. *Microwave transitions as a signature of coherent parity mixing effects in the Majorana-transmon qubit*. Nature communications **5**, 4772 (2014).
- [151] D. Karki, K. Matveev, and I. Martin. *Physics of the Majorana superconducting qubit hybrids*. Physical Review B **109**, 085410 (2024).
- [152] D. M. Pino, R. S. Souto, and R. Aguado. *Minimal Kitaev-transmon qubit based on double quantum dots*. Physical Review B **109**, 075101 (2024).
- [153] B.-L. Najera-Santos, R. Rousseau, K. Gerashchenko, H. Patange, A. Riva, M. Villiers, T. Briant, P.-F. Cohadon, A. Heidmann, J. Palomo, et al. *High-sensitivity AC-charge detection with a Mhz-frequency fluxonium qubit*. Physical Review X **14**, 011007 (2024).
- [154] J. B. Hertzberg, E. J. Zhang, S. Rosenblatt, E. Magesan, J. A. Smolin, J.-B. Yau, V. P. Adiga, M. Sandberg, M. Brink, J. M. Chow, et al. *Laser-annealing Josephson junctions for yielding scaled-up superconducting quantum processors*. npj Quantum Information **7**, 129 (2021).

- [155] T. Takahashi, N. Kouma, Y. Doi, S. Sato, S. Tamate, and Y. Nakamura. *Uniformity improvement of Josephson-junction resistance by considering sidewall deposition during shadow evaporation for large-scale integration of qubits*. Japanese Journal of Applied Physics **62**, SC1002 (2022).
- [156] A. M. Bozkurt and V. Fatemi, *Josephson tunnel junction arrays and Andreev weak links: what's the difference?*, in Spintronics XVI, Vol. 12656 (Sept. 2023), pp. 35–43.
- [157] J. Ulrich and F. Hassler. *Dual approach to circuit quantization using loop charges*. Phys. Rev. B **94**, 094505 (2016).
- [158] Z. Feng, X. Zhou, L. Šmejkal, L. Wu, Z. Zhu, H. Guo, R. González-Hernández, X. Wang, H. Yan, P. Qin, X. Zhang, H. Wu, H. Chen, Z. Xia, C. Jiang, M. Coey, J. Sinova, T. Jungwirth, and Z. Liu. *An anomalous Hall effect in altermagnetic ruthenium dioxide*. Nature Electronics **5**, 735 (2022).
- [159] C. A. Occhialini, L. G. P. Martins, S. Fan, V. Bisogni, T. Yasunami, M. Musashi, M. Kawasaki, M. Uchida, R. Comin, and J. Pellicari. *Strain-modulated anisotropic electronic structure in superconducting RuO_2 films*. Phys. Rev. Mater. **6**, 084802 (2022).
- [160] I. I. Mazin. *Notes on altermagnetism and superconductivity*. Phys. Rev. B **76**, 214507 (2007) eprint: arXiv:2203.05000.
- [161] C. W. J. Beenakker. *Universal limit of critical-current fluctuations in mesoscopic Josephson junctions*. Phys. Rev. Lett. **67**, 3836 (1991).
- [162] I. O. Kulik and A. N. Omel'yanchuk. *Properties of superconducting microbridges in the pure limit*. Sov. J. Low Temp. Phys. **3**, 459 (1977).
- [163] C. W. Groth, M. Wimmer, A. R. Akhmerov, and X. Waintal. *Kwant: a software package for quantum transport*. New J. Phys. **16**, 063065 (2014).
- [164] J. Feldmann, K. Leo, J. Shah, D. A. B. Miller, J. E. Cunningham, T. Meier, G. von Plessen, A. Schulze, P. Thomas, and S. Schmitt-Rink. *Optical investigation of Bloch oscillations in a semiconductor superlattice*. Phys. Rev. B **46**, 7252 (1992).
- [165] H. Kurz, H. G. Roskos, T. Dekorsy, and K. Köhler. *Bloch oscillations*. Phil. Trans. Roy. Soc. A **354**, 2295 (1996).

- [166] K. Vilkelis, L. Wang, and A. R. Akhmerov. *Bloch-Lorentz magnetoresistance oscillations in delafossites*. SciPost Physics **15**, 019 (2023).
- [167] C. W. J. Beenakker and H. van Houten. *Quantum transport in semiconductor nanostructures*. Solid State Phys. **44**, 1 (1991).
- [168] C. D. Beule, F. Dominguez, and P. Recher. *Aharonov-bohm oscillations in minimally twisted bilayer graphene*. Phys. Rev. Lett. **125**, 096402 (2020).
- [169] P. S. Mahapatra, M. Garg, B. Ghawri, A. Jayaraman, K. Watanabe, T. Taniguchi, A. Ghosh, and U Chandni. *Quantum Hall interferometry in triangular domains of marginally twisted bilayer graphene*. Nano Letters **22**, 5708–5714 (2022).
- [170] Y.-Z. Chou, F. Wu, and S. D. Sarma. *Hofstadter butterfly and Floquet topological insulators in minimally twisted bilayer graphene*. Phys. Rev. Research **2**, 033271 (2020).
- [171] C. D. Beule, F. Dominguez, and P. Recher. *Effective Floquet model for minimally twisted bilayer graphene*. Phys. Rev. B **103**, 195432 (2021).
- [172] J. Kempe. *Quantum random walks — an introductory overview*. Contemp. Phys. **44**, 307 (2003).
- [173] C. Cedzich, T. Rybár, A. H. Werner, A. Alberti, M. Genske, and R. F. Werner. *Propagation of quantum walks in electric fields*. Phys. Rev. Lett. **111**, 160601 (2013).
- [174] P. Arnault, B. Pepper, and A. Pérez. *Quantum walks in weak electric fields and Bloch oscillations*. Phys. Rev. A **101**, 062324 (2020).
- [175] C. Cedzich and A. H. Werner. *Anderson localization for electric quantum walks and skew-shift cmv matrices*. Comm. Math. Phys. **387**, 1257 (2021).
- [176] A. Regensburger, C. Bersch, B. Hinrichs, G. Onishchukov, A. Schreiber, C. Silberhorn, and U. Peschel. *Zitterbewegung, Bloch oscillations and Landau-Zener tunneling in a quantum walk*. Phys. Rev. B **76**, 214507 (2007) eprint: [arXiv:1104.0105](https://arxiv.org/abs/1104.0105).
- [177] A. D’Errico, R. Barboza, R. Tudor, A. Dauphin, P. Massignan, L. Marrucci, and F. Cardano. *Bloch-Landau-Zener dynamics induced by a synthetic field in a photonic quantum walk*. APL Photonics **6**, 020802 (2021).

- [178] M. Genske, W. Alt, A. Steffen, A. H. Werner, R. F. Werner, D. Meschede, and A. Alberti. *Electric quantum walks with individual atoms*. Phys. Rev. Lett. **110**, 190601 (2013).
- [179] D. Shoenberg. *Magnetic oscillations in metals*. Vol. 76 (Cambridge university press, 2009), p. 214507.
- [180] A Alexandradinata and L. Glazman. *Semiclassical theory of Landau levels and magnetic breakdown in topological metals*. Physical Review B **97**, 144422 (2018).
- [181] T. Vakhtel, D. O. Oriekhov, and C. W. J. Beenakker, *Bloch oscillations in the magnetoconductance of twisted bilayer graphene: code for numerical calculations*, version v2, 2022.
- [182] Y. V. Sharvin. *A possible method for studying Fermi surfaces*. Sov. Phys. JETP **21**, 655 (1965).
- [183] Y. V. Sharvin and M. L. Fisher. *Observation of focused electron beams in a metal*. JETP Lett. **1**, 152 (1965).
- [184] V. S. Tsoi. *Focusing of electrons in a metal by a transverse magnetic field*. JETP Lett. **19**, 70 (1974).
- [185] V. S. Tsoi, J. Bass, and P. Wyder. *Studying conduction-electron/interface interactions using transverse electron focusing*. Rev. Mod. Phys. **71**, 1641 (1999).
- [186] S. I. Bozhko. *Focusing of electrons by a transverse magnetic field*. JETP Lett. **99**, 487 (2014).
- [187] H. van Houten, C. W. J. Beenakker, J. G. Williamson, M. E. I. Broekaart, P. H. M. van Loosdrecht, B. J. van Wees, J. E. Mooij, C. T. Foxon, and J. J. Harris. *Coherent electron focusing with quantum point contacts in a two-dimensional electron gas*. Phys. Rev. B **39**, 8556 (1989).
- [188] P. Rakyta, A. Kormanyos, J. Cserti, and P. Koskinen. *Exploring the graphene edges with coherent electron focusing*. Phys. Rev. B **81**, 115411 (2010).
- [189] T. Stegmann, D. E. Wolf, and A. Lorke. *Magnetotransport along a boundary: from coherent electron focusing to edge channel transport*. New J. Phys. **15**, 113047 (2013).

-
- [190] T. Taychatanapat, K. Watanabe, T. Taniguchi, and P. Jarillo-Herrero. *Electrically tunable transverse magnetic focusing in graphene*. *Nature Phys.* **9**, 225 (2013).
- [191] T. Vakhrel, D. O. Oriekhov, and C. W. J. Beenakker. *Bloch oscillations in the magnetoconductance of twisted bilayer graphene*. *Phys. Rev. B* **105**, L241408 (2022).
- [192] C. Putzke, M. D. Bachmann, P. McGuinness, E. Zhakina, V. Sunko, M. Konczykowski, T. Oka, R. Moessner, A. Stern, M. König, S. Khim, A. P. Mackenzie, and P. J. W. Moll. *H/e oscillations in interlayer transport of delafossites*. *Science* **368**, 1234 (2020).
- [193] X.-G. Zhao, R. Jahnke, and Q. Niu. *Dynamic fractional stark ladders in dc-ac fields*. *Phys. Lett.* **202**, 297 (1995).
- [194] A. B. Pippard. *Magnetomorphic oscillations due to open orbits*. *Phil. Mag.* **13**, 1143 (1965).
- [195] J. A. Munarin and J. A. Marcus. *New oscillatory magnetoresistance effect in gallium*. *Phys. Rev. B* **743**, 214507 (1965).
- [196] J. A. Munarin, J. A. Marcus, and P. E. Bloomfield. *Size-dependent oscillatory magnetoresistance effect in gallium*. *Phys. Rev.* **172**, 718 (1968).
- [197] A. Gupta, J. J. Heremans, G. Kataria, M. Chandra, S. Fallahi, G. C. Gardner, and M. J. Manfra. *Precision measurement of electron-electron scattering in GaAs/AlGaAs using transverse magnetic focusing*. *Nature Commun.* **12**, 5048 (2021).
- [198] H. Takatsu, J. J. Ishikawa, S. Yonezawa, H. Yoshino, T. Shishidou, T. Oguchi, K. Murata, and Y. Maeno. *Extremely large magnetoresistance in the nonmagnetic metal PdCoO₂*. *Phys. Rev. Lett.* **111**, 056601 (2013).

Summary

A Josephson junction is a device where a thin insulating barrier or a nanostructure is placed between two superconducting leads. A superconductor is characterized by an order parameter that is a complex number. The phase difference $\Delta\phi$ between the order parameters of the two superconducting leads is a coordinate typically used to describe the state of the junction. Such a junction is essential to superconducting qubits that store quantum information due to its anharmonic spectrum. Therefore, understanding the physics of these junctions is crucial for predictions of the qubit's main qualities, such as the dephasing and relaxation time. Most modern superconducting qubits use Josephson junctions with an insulating barrier (tunneling junction). One of this thesis aims is to explore other possibilities that may allow for better properties of the qubit.

Chapter 2 considers a qubit with a Josephson junction containing a single resonant level connected in parallel with a capacitor (capacitive shunt). For the control of the qubit, it is necessary to have a gate controlling the charge on the capacitor. However, fluctuations of the energy of the qubit with the gate voltage (charge dispersion) decrease the dephasing time. The charge dispersion is typically reduced by making the capacitor very large. However, this also increases the size of the qubit and the dielectric losses. In this Chapter, we study how the charge dispersion changes if a resonant level junction is used instead of the tunneling one. We show that, for the same transition frequency and capacitance of the qubit, the charge dispersion can be significantly reduced in some fine-tuned regimes.

In Chapter 3 we add an additional inductive shunt to the circuit considered in Chapter 2. The spectrum of the qubit doesn't depend on the gate voltage, but such a circuit can be used to implement a so-called bifluxon qubit, where a conservation law forbids its decay. We also show that for a sufficiently large inductance, the Hamiltonian of the circuit is dual to a topological superconducting island.

Chapter 4 concerns a planar Josephson junction with an altermagnetic material in between two superconductors. Altermagnetism is a new kind of magnetic order with a spin-polarized Fermi surface and broken time-reversal symmetry, but with zero net magnetization. We take a microscopic approach to the problem and look at how the states localized at the junction – Andreev bound states – are affected by altermagnetism. We derive that these states are spin-split and observe that for certain ranges of the junction’s length, the minimum of the energy of the junction is achieved at $\Delta\phi = \pi$ rather than at $\Delta\phi = 0$ (as in most Josephson junctions, such as the tunneling one). This type of junction can be a useful element for the creation of qubits protected against relaxation. It can provide a stable π phase bias in circuits implementing elements with conserved parity of Cooper pairs. The parity can act as a conserved quantity limiting the relaxation of the qubit. This type of qubit is dual to the bifluxon qubit mentioned in the previous paragraph.

In Chapter 5, we investigate magnetotransport in minimally twisted bilayer graphene. Minimally twisted bilayer graphene is a 2D material made of two graphene layers twisted at a very small angle $\sim 0.1^\circ$ with respect to each other. The material typically relaxes to a superlattice of domains with two relative upper and bottom layer alignments. If a perpendicular electric field is applied, the transport in such a material is dominated by a network of ballistic channels propagating along the domains. We study the dependence of the conductance of such a sample as a function of the perpendicularly applied weak magnetic field. The conductance shows oscillations that can be mapped to the Bloch oscillations of electrons in a 1D crystal.

In Chapter 6, we study magnetotransport in 2D materials, where the Fermi surface is open in one direction. This is a generalization of the situation studied in Chapter 5. We show that such materials feature a magnetic focusing effect with the focusing length $\Delta x = (eaB/h)^{-1}$ (where B is the applied magnetic field and a is the lattice constant). This effect is distinct from the usual magnetic focusing effect due to the Lorentz force and has no classical analogue. We also generalize our results to the case of multiple open orbits weakly coupled with each other.

Samenvatting

Een Josephson-junctie bestaat uit een dunne isolerende barrière of een nanostructuur die tussen twee supergeleidende draden wordt geplaatst. Een supergeleider wordt gekarakteriseerd door een ordeparameter die een complex getal is. Het faseverschil $\Delta\phi$ tussen de ordeparameters in de beide draden beschrijft de toestand van de junctie. Zo'n junctie is essentieel voor supergeleidende qubits die quantuminformatie opslaan. Daarom is het begrijpen van de fysica van deze juncties cruciaal voor voorspellingen van de belangrijkste eigenschappen van de qubit, zoals de coherentie en relaxatietijd. De meeste moderne supergeleidende qubits gebruiken Josephson juncties met een isolerende barrière (tunnel-juncties). Een van de doelen van dit proefschrift is om andere mogelijkheden te onderzoeken die betere eigenschappen van de qubit mogelijk maken.

Hoofdstuk 2 beschouwt een qubit met een Josephson junctie die een enkel resonant energiniveau bevat dat parallel is geschakeld met een condensator. Voor de besturing van de qubit is een elektrode nodig die de lading op de condensator regelt. Schommelingen van de energie van de qubit met de spanning verminderen echter de coherentietijd. De schommelingen worden meestal verminderd door de condensator erg groot te maken. Dit vergroot echter ook de grootte van de qubit en de dielektrische verliezen. In dit hoofdstuk bestuderen we hoe de ladingsdispersie verandert als er een resonante koppeling wordt gebruikt in plaats van de tunnel-koppeling. We laten zien dat, voor dezelfde overgangsfrequentie en capaciteit van de qubit, de ladingsdispersie aanzienlijk kan worden verminderd in sommige regimes.

In hoofdstuk 3 voegen we een extra inductief element toe aan de schakeling die in hoofdstuk 2 is beschreven. Het spectrum van de qubit hangt niet af van de poortspanning, maar een dergelijke schakeling kan worden gebruikt om een zogenaamde bifluxon qubit te implementeren, waarbij een behoudswet het verval verbiedt. We laten ook zien dat voor een vol-

doende grote inductantie de Hamiltoniaan van de schakeling dual is aan een topologisch supergeleidend eiland.

Hoofdstuk 4 gaat over een Josephson junctie met een altermagnetisch materiaal tussen twee supergeleiders. Altermagnetisme is een nieuw soort magnetische orde met een spin-gepolariseerd Fermi-oppervlak en gebroken tijd-omkeringssymmetrie, maar met nul netto magnetisatie. We benaderen het probleem microscopisch en bekijken hoe de gelocaliseerde toestanden gelokaliseerd in de junctie - Andreev-gebonden toestanden - worden beïnvloed door altermagnetisme. We leiden af dat deze toestanden spin-gepolariseerd zijn en observeren dat voor bepaalde lengtes van de junctie, het minimum van de energie van de junctie wordt bereikt bij $\Delta\phi = \pi$ in plaats van bij $\Delta\phi = 0$ (zoals in de meeste Josephson juncties, zoals de tunnel-junctie). Deze eigenschap kan nuttig zijn voor het maken van qubits die beschermd zijn tegen relaxatie.

In hoofdstuk 5 onderzoeken we magnetotransport in minimaal getwist tweelaagig grafeen. Minimaal getwist tweelaagig grafeen is een tweedimensionaal materiaal dat bestaat uit twee lagen grafeen die onder een zeer kleine hoek (1/10de graad) ten opzichte van elkaar gedraaid zijn. In het materiaal ontstaat een superrooster van domeinen met twee relatieve uitlijningen van de bovenste en onderste laag. Als er een loodrecht elektrisch veld wordt aangelegd, wordt het transport in zo'n materiaal gedomineerd door een netwerk van geleidende toestanden die zich voortplanten langs de domeinranden. We bestuderen de afhankelijkheid van de geleiding van een dergelijk systeem als functie van een loodrecht aangelegd zwak magnetisch veld. De geleiding vertoont oscillaties die een manifestatie zijn van Bloch oscillaties van elektronen.

In hoofdstuk 6, tenslotte, bestuderen we magnetotransport in tweedimensionale materialen, waarbij het Fermi-oppervlak in één richting open is. Dit is een veralgemening van de situatie die in hoofdstuk 5 is bestudeerd. We laten zien dat dergelijke materialen een magnetisch lens-effect hebben. Dit effect verschilt van het gebruikelijke magnetische lens-effect als gevolg van de Lorentzkracht en heeft geen klassieke analogie. We veralgemenen onze resultaten ook naar het geval van meerdere open banen die zwak aan elkaar gekoppeld zijn.

Підсумки

Джозефсонівський контакт — це пристрій, у якому тонкий ізолюючий бар'єр або наноструктура розміщена між двома надпровідними електродами. Надпровідник характеризується параметром порядку, який є комплексним числом. Різниця фаз між параметрами порядку двох електродів $\Delta\phi$ зазвичай використовується як координата для опису стану контакту. Такий контакт є важливою компонентою надпровідних кубітів, завдяки ангармонічності спектру. Тому розуміння фізики цих контактів є ключовим для опису основних характеристик кубіта, таких як час дефазування та релаксації. Більшість сучасних надпровідних кубітів використовують Джозефсонівські контакти з ізолюючим бар'єром (тунельні контакти). Однією з цілей цієї дисертації є дослідження інших різновидностей контактів, які можуть забезпечити кращі властивості кубіта.

У розділі 2 розглядається кубіт з Джозефсонівським контактом, що містить один резонансний рівень, підключений паралельно до конденсатора (ємнісна шунтовка). Для керування кубітом необхідно мати затвор, що контролює заряд на конденсаторі. Однак, коливання енергії кубіта при зміні напруги на затворі (зарядова дисперсія) зменшують час дефазування. Зарядова дисперсія зазвичай зменшується шляхом збільшення ємності конденсатора. Проте це також збільшує фізичний розмір кубіта та діелектричні втрати. У цьому розділі ми досліджуємо, як змінюється зарядова дисперсія, якщо замість тунельного контакту використовується контакт з резонансним рівнем. Ми показуємо, що при тій самій частоті переходу та ємності кубіта, зарядова дисперсія може бути значно зменшена в деяких точно налаштованих режимах.

У розділі 3 ми додаємо додаткову індуктивну шунтовку до схеми, розглянутої в розділі 2. Спектр кубіта не залежить від напруги на затворі, але така схема може бути використана для реалізації так званого біфлюксонного кубіта, де закон збереження забороняє переходи

між рівнями, що використовуються для обчислень. Ми також показуємо, що при достатньо великій індуктивності гамільтоніан системи є дуальним до зарядового кубіта з топологічним Джозефсонівським контактом.

Розділ 4 стосується планарного Джозефсонівського контакту з альтермагнітним матеріалом між двома надпровідниками. Альтермагнетизм — це новий вид магнітного порядку зі спин-поляризованою Фермі-поверхнею і порушеною Т-симетрією, але з нульовою сумарною намагніченістю. Ми підходимо до проблеми з мікроскопічної точки зору і досліджуємо, як альтермагнетизм впливає на стани, локалізовані в контакті — Андреевські зв'язані стани. Ми отримуємо, що ці стани розщеплені по спіну, і спостерігаємо, що для певних діапазонів довжини контакту, мінімум енергії досягається при $\Delta\phi = \pi$, а не при $\Delta\phi = 0$ (як у більшості Джозефсонівських контактів, таких як тунельний). Такий тип контакту може бути корисним елементом для створення кубітів захищених від релаксації.

У розділі 5 ми досліджуємо магнітотранспорт у мінімально скрученому двошаровому графені. Мінімально скручений двошаровий графен — це 2D матеріал, утворений двома шарами графену, скрученими під дуже малим кутом $\sim 0.1^\circ$ один до одного. Матеріал зазвичай релаксує до надгратки доменів із двома можливими відносними вирівнюваннями верхнього та нижнього шарів. Якщо прикласти перпендикулярне електричне поле, транспорт у такому матеріалі визначається мережею балістичних каналів, що проходять уздовж доменів. Ми досліджуємо залежність провідності такого зразка як функцію прикладеного перпендикулярного слабкого магнітного поля. Провідність демонструє осциляції, математично еквівалентні осциляціям Блоха електронів в 1D кристалі.

У розділі 6 ми досліджуємо магнітотранспорт у 2D матеріалах, де Фермі-поверхня відкрита в одному напрямку. Це узагальнення ситуації, дослідженої в розділі 5. Ми показуємо, що такі матеріали характеризуються ефектом магнітного фокусування з довжиною фокусування $\Delta x = (eaB/h)^{-1}$ (де a — це постійна ґратки, а B — напруженість магнітного поля). Цей ефект відрізняється від звичайного ефекту магнітного фокусування через силу Лоренца і не має класичного аналога. Ми також узагальнюємо наші результати на випадок декількох відкритих орбіт, слабо зв'язаних між собою.

Curriculum Vitæ

I was born on November 24, 1997, in Kyiv, and spent a significant part of my childhood there and in Berdiansk (Ukraine). My grandmother and grandfather were both theoretical physicists, so I learned about this profession very early and have been interested in natural sciences all my life. I studied at Kyiv Natural Science Lyceum no. 145, which produced many talented Ukrainian scientists. During high school, I attended lectures at the Bogoliubov Institute for Theoretical Physics on various math and physics subjects. These lectures and exceptionally positive experiences at the lyceum convinced me to pursue physics as a career.

In 2014, I enrolled in the Quantum Field Theory Bachelor programme at the National University of Kyiv. The programme was mainly focused on the quantum field theory applications to high-energy physics, but after the Higgs boson discovery in 2012 and the subsequent absence of further discoveries, I became interested in condensed matter physics. After defending the Bachelor's thesis under the supervision of Prof. Vadim Cheianov, I continued my studies as a Master's student at the Lorentz Institute for theoretical physics of Leiden University. During the programme, I also took math and physics courses at various institutions nationwide, such as the University of Amsterdam, Utrecht University, and the Technical University of Delft. I graduated in 2020 with a Master's thesis on thermalization in integrable field theories under the supervision of Prof. Koenraad Schalm.

In September 2020, I started my PhD in mesoscopic physics under the supervision of Prof. Carlo Beenakker. The lectures at TU Delft and the University of Amsterdam sparked my interest in experiments, so I also joined the laboratory of Prof. Leo Kouwenhoven in Delft as a guest theorist, where Dr. Bernard van Heck became my second supervisor. The main subjects of my research were circuit QED, quantum transport in 2D materials and hybrid Josephson junctions. I also performed a beamline experiment with Dr. Gesa Welker at a low-energy muon facility at the Paul

Scherrer Institute in Switzerland. In the last two years of my PhD, I spent 4 months in Grenoble (France), working with Prof. Nicolas Roch and Prof. Denis Basko on superconducting circuits and many-body localization. I also presented my research at various international conferences and during group visits in France, Spain and Switzerland.

After finishing my PhD, I'm excited to continue my path as a postdoc in Dr. Maximilian Rimbach-Russ' group in Delft, studying semiconductor spin qubits.

List of Publications

- [1] Philippe Sabella-Garnier, Koenraad Schalm, Tereza Vakhtel, Jan Zaanen, *Thermalization/Relaxation in integrable and free field theories: an Operator Thermalization Hypothesis*, arXiv:1906.02597 2019.
- [2] T. Vakhtel, D. O. Oriekhov, C. W. J. Beenakker, *Bloch oscillations in the magnetoconductance of twisted bilayer graphene*, Phys. Rev. B **105**, L241408 (2022) [Chapter 5].
- [3] D. O. Oriekhov, T. T. Osterholt, T. Vakhtel, A. R. Akhmerov, and C. W. J. Beenakker, *Breathing mode in open-orbit magnetotransport: a magnetic lens with a quantum mechanical focal length*, Phys. Rev. B **106**, 235413 (2022) [Chapter 6].
- [4] Tereza Vakhtel and Bernard van Heck, *Quantum phase slips in a resonant Josephson junction*, Phys. Rev. B **107**, 195405 (2023) [Chapter 2].
- [5] C. W. J. Beenakker and T. Vakhtel, *Phase-shifted Andreev levels in an altermagnet Josephson junction*, Phys. Rev. B **107**, 075425 (2023) [Chapter 4].
- [6] T. Vakhtel, P. D. Kurilovich, M. Pita-Vidal, A. Bargerbos, V. Fatemi, B. van Heck, *Tunneling of fluxons via a Josephson resonant level*, Phys. Rev. B **110**, 045404 (2024) [Chapter 3].
- [7] W. Ardati, S. Léger, S. Kumar, V. N. Suresh, D. Nicolas, C. Mori, F. D'Esposito, T. Vakhtel, O. Buisson, Q. Ficheux, N. Roch, *Using bi-fluxon tunneling to protect the Fluxonium qubit*, arXiv:2402.04495 (2024).

Stellingen

behorende bij het proefschrift

Hybrid Josephson junctions and their qubit applications

1. Resonant Cooper pair tunneling allows for a qubit with a reduced charge dispersion at a fixed ratio of the qubit frequency to the charging energy.
Chapter 2
2. When the inductive energy of a superconducting loop becomes much smaller than the Josephson plasma frequency, the circuit is well described by a low-energy theory dual to that of a topological superconducting island.
Chapter 3
3. A Josephson junction with d -wave magnetization has spin-polarized Andreev levels.
Chapter 4
4. The oscillatory electron motion known as a Bloch oscillation can be observed in DC electrical transport.
Chapter 5
5. Observation of the 4π -periodic Josephson effect does not necessarily imply the tunneling of single electrons.
6. The coherence time T_2 of state-of-the-art Andreev spin qubits is most likely limited by the coupling to nuclear spins.
7. A material that is proven to be an altermagnet does not yet exist.
8. Circuit realizations of efficient Josephson diodes are the easiest to fabricate.
9. Quasiparticle poisoning is not a relevant limitation on the coherence time of currently existing qubits.
10. The current grant system slows down scientific progress because the best researchers spend a significant amount of time writing and evaluating grant proposals.

Tereza Vakhtel

Leiden, 3 September 2024